Study of Fueling on the Large Helical Device by Gas Puffing and Compact Toroid Injection

Junichi Miyazawa

Doctor of Philosophy

Department of Fusion Science

School of Mathematical and Physical Science

The Graduate University for Advanced Studies

2003

Study of Fueling on the Large Helical Device by Gas Puffing and Compact Toroid Injection

Junichi Miyazawa

A dissertation presented to the National Institute for Fusion Science

for the degree of

Doctor of Philosophy

Department of Fusion Science

School of Mathematical and Physical Science

The Graduate University for Advanced Studies

2003

Abstract

Establishment of a fueling method in hot and large plasmas is one of the important issues to realize the fusion rector. An ideal fueling system for the steady-state fusion reactor should be as simple as the gas puffing, simultaneously achieving high fueling efficiency as the ice-pellet injection. Furthermore, the fueling method that can improve the confinement property of the main plasma is favorable. In this thesis, two fueling methods in the Large Helical Device (LHD) are studied. One is the gas puffing, which is the most basic fueling method, and another is the Compact Toroid (CT) injection, which is the most advanced fueling method. For reliable density control by gas puffing, it is important to understand the response of the plasma density to the gas puff flux. The fueling efficiency of gas puffing in LHD has not been known, while it has been estimated as ~ 10 % in diverted tokamaks. Determination of the fueling efficiency is often complicated and one should carefully consider the particle balance. Investigation of the confinement improvement is one of the important themes of the fusion plasma experiment. Making use of the flexibility of gas puffing that the working gas can be changed from hydrogen to other high-Z gasses, it is possible to change the plasma property. The confinement improvement due to the high-Z gas puffing has been reported from tokamaks as known as the radiative improved mode. The high-Z gas puff experiment can be more easily carried out in currentless LHD plasmas, since there is no concern about the dangerous current disruption. In the meanwhile, gas puffing is not capable of the direct fueling into the hot plasma core, which is thought to be favorable for the fusion reactor. One of the possible methods is the CT injection, where a high-density magnetized plasmoid is accelerated and injected into the target plasma. CT injection has been carried out in small/medium tokamaks. However, it has not been obvious if this can be applied to the large helical plasmas. Technically, the critical pass of CT injection in LHD lies in the long-distance transfer of CT. The distance from LHD port to plasma center is about 4 m. Since such a long distance transfer has not been reported, it is necessary to carry out the experiment for proof.

In this thesis, the fueling efficiency of gas puffing in LHD has been estimated for the first time. The 'effective' fueling efficiency of hydrogen gas puffing ranges from 10 to 50 %, in LHD. Here, the effective fueling efficiency is defined as the time derivative of the total number of electrons divided by the electron flux supplied by gas puffing. The particle balance analysis reveals that the recycling flux increases during the gas puffing and causes the high effective fueling efficiency. At the limit of small recycling flux, the effective fueling

efficiency decreases to ~ 10 %, which can be taken as the 'real' fueling efficiency of gas puffing in LHD. In the helium gas puff discharge, where the recycling flux is large, the effective fueling efficiency is larger than the hydrogen gas puffing and approaches 100 %. This can be related to the large recycling coefficient of more than 0.95.

Two representative examples of the high-Z gas puff experiment in LHD are also presented. The particle confinement was improved in the high-density pellet shot after the methane mixed hydrogen gas puff discharges. Only four discharges introducing ~ 20 $Pa \cdot m^3$ of methane caused the reduction of the radiation loss and the level of metal impurities as expected as the real time carbonization effect. Decay rate of the electron density was mitigated in the pellet shot after methane discharges. Transport analysis shows 60 % reduction in the particle transport coefficient at the half of the averaged minor radius. In the neon gas puff experiment, reduced ion number density resulted in the higher ion temperature than that obtained in hydrogen plasmas. The electron energy confinement of neon plasmas is highlighted and revealed to be similar to that of hydrogen plasmas. In both cases, the global electron energy confinement strongly depends on the electron gyro-radius. A new scaling law that describes the global electron energy confinement of hydrogen and neon plasmas in LHD has been derived.

The possibility of CT injection experiment on LHD has been researched based on the CT orbit calculation and the development of a CT injector named SPICA (SPheromak Injector using Conical Accelerator). CT trajectories in the helical magnetic field were calculated and the possibility of central fueling was confirmed with a model CT of 0.2 m diameter, 10^{22} m^{-3} electron density, and 300 km/s initial velocity, in the case of CT injection into LHD magnetic field of 1.5 T. A CT of spheromak-type magnetic configuration can be formed using co-axial plasma gun. Optimization of the CT injector for LHD has been carried out and a conical electrode for CT compression is adopted in the design. Point-model of CT acceleration in a co-axial electrode was solved to optimize the electrode geometry and the power supplies. Based on the results, SPICA was developed and the CT acceleration experiments have been carried out. SPICA is the largest CT injector in the world, which aims at fueling. In the experiment, high speed CT of over 200 km/s was obtained. It was also demonstrated that the CT could be transferred more than 3.6 m after the acceleration. These results indicate that SPICA has enough performance to carry out the CT injection experiment on LHD.

The basic objective of this thesis is to extend our knowledge on the fueling and the related physics problems. Although the knowledge obtained here is limited, it will be available for understanding the fueling physics. In the investigation of other fueling methods,

such as the pellet injection, and the neutral beam injection, the information presented in this thesis will give the basis for comparison. Even for the complementary study of tokamak plasmas with helical plasmas, the results of this thesis can afford the basic database.

Acknowledgements

The present work has been performed at the National Institute for Fusion Science (NIFS). It is an honor to express herewith the most profound gratitude to Associate Professor H. Yamada for his continuous support, invaluable consultations and advices throughout the whole period of this study. The great pleasure for the author is to express the sincerest thanks and deepest appreciation to Professor K. Yamazaki. Moreover, the author is deeply thankful to Professor O. Motojima for his continuous encouragements.

The author would like to convey his great thankfulness to Dr. N. Fukumoto who has vigorously carried out the experiments on SPICA with me. The author would like to acknowledge the useful comments and warm encouragement by Associate Professor M. Nagata. The special words of gratitude should also be addressed to Professor T. Uyama whose constant extensive assistance and support cannot be overemphasized.

The expressions of gratefulness should be extended to Professor N. Inoue, Professor Z. Yoshida and Professor Y. Ogawa for providing me an opportunity to study the fusion plasma physics.

Additionally, the author would like to acknowledge K. Yasui for his help in all over my work. The author is also thankful to all of the members of the LHD team, including technical staffs of NIFS and graduate students of Nagoya University and the Graduate University of Advanced studies.

Finally, I wish to thank my wife, my daughter, and my son.

Contents

Chapter 1 Introduction

Establishment of the fueling method in hot and large plasmas is one of the important issues to realize the fusion rector. Listed below are the typical fueling methods utilized in the fusion plasma experiment:

(*Gas injection*)

- Gas puffing : Low fueling efficiency.
- Supersonic gas puffing : Medial fueling efficiency.

(*Solid injection*)

- Ice-pellet injection : High fueling efficiency.

(*Plasma application*)

- Neutral beam injection : High fueling efficiency.
- Compact toroid (CT) injection : High fueling efficiency.

In general, the gas injection system is simple and can be easily applied in the steady state operation [1 - 8]. The fueling efficiency of gas puffing, however, is thought to be not satisfying. Recently, the supersonic gas puffing (supersonic molecular beam injection, MBI, in [9 - 12], and supersonic pulsed gas injection, SPGI, in [13 - 15]) is attracting an attention of the fusion community. This method was proposed to realize the high fueling efficiency with a supersonic high-density cloud of neutrals. Due to the collective effect of the high-density cloud that cools the plasma surface of a small area, the penetration depth is expected to be deeper than that of the ordinary spread gas puffing. In the Tore Supra tokamak, for example, a fueling efficiency of 30 – 50 % was achieved [15]. It is necessary to perform the efficiency of supersonic gas puffing on large plasmas. Ice-pellet injection has achieved high fueling efficiency of up to 100 %, especially in the case of high-field side injection [16, 17]. On the other hand, the steady state density control by the repetitive ice-pellet injection has not been performed to date, although it is being developed intensively. Neutral beam injection has the capabilities of plasma center fueling and plasma flow induction [18 - 20]. In this case, the cost is considerably higher than the others. CT injection is the most advanced fueling method that has a possibility of achieving high fueling efficiency [21 - 30]. The confinement improvement of the plasmas triggered by CT injection is also expected. Application of this on large plasmas has been waited. The ideal fueling system for the steady-state fusion reactor should be as simple as the gas puffing, simultaneously achieving the high fueling efficiency as the pellet

injection. Furthermore, the fueling method that can improve the confinement property of the fusion plasma is favorable, if possible.

In this thesis, two of the above fueling methods are studied in the framework of Large Helical Device (LHD). One is the gas puffing, which is the most basic technique utilized from the beginning of nuclear fusion research, and another is the CT Injection, which is the most recent and advanced fueling method. LHD is the world-largest super-conducting machine with the heliotron configuration, where the large current-free toroidal plasmas are being studied [31 - 34]. LHD has a set of continuous helical coils and three sets of poloidal coils, which generate the nested magnetic surfaces, where the field period around the torus is 10 and the pole number is 2. The maximum magnetic field at the plasma center reaches ~ 3 T. The major radius of the vacuum vessel is 3.9 m. The plasma minor radius can be changed from 0.5 to 0.65 m. Major objectives of LHD are: (1) achievement of high $n\tau T$ plasmas for the transport study which can be extrapolated to the fusion reactor plasmas; (2) achievement of high-beta plasmas of $<\beta> > 5$ %, and investigation of the relevant physics; (3) development of divertor device which enables the long-pulse experiment of current-free plasmas, and obtain the basic data for steady-state operation; (4) study of the high-energy particle behavior in helical magnetic fields, and experimental simulation of the α particles in fusion plasmas; and (5) complementary study with tokamaks for general understandings of the toroidal plasma physics. The large and hot LHD plasma is an adequate object for fueling study. Since no current is necessary to form the magnetic surfaces for plasma confinement, there are fewer concerns about the instabilities than tokamak plasmas. On the other hand, LHD plasma is showing a plenty of common plasma physics with the tokamak plasmas, such as the gyro-Bohm like behavior of the energy confinement and the fueling efficiency of gas puffing, as will be shown in this thesis. Study on LHD will help the understandings of tokamak plasmas, which is thought to be the nearest to the nuclear fusion reactor, at this moment.

Although gas puffing is a conventional and convenient way to control the plasma density, there have been remained many unsolved problems. For instance, the fueling efficiency of gas puffing in LHD has not been known. The fueling efficiency of gas puffing is one of the important parameters to describe the particle balance of the fusion plasmas, and has been studied in numerous tokamaks. Typically, the fueling efficiency of gas puffing on the diverted tokamaks is 10 %. Conventional method to estimate the fueling efficiency of gas puffing is to compare the time derivative of the electron density before and after the gas puff termination. However, this method has a difficulty; i.e. it is necessary to assume the related

parameters, such as the fueling efficiency or the recycling rate, are constant around the termination, and this inevitably includes the inconsistency since gas puff termination itself is transient. Another simple method is to compare the total amount of the particles puffed during the discharge and the total particle number in the plasma. This method also has a difficulty since the plasma density of the previous discharges largely affects the total particle number via an enhanced recycling process. In this thesis, the fueling efficiency is investigated based on a particle balance model. According to the model, it is possible to estimate the fueling efficiency from the ratio of density increase rate to the gas puff flux, as long as the change in the plasma density is due to the gas puffing alone. This method is robust to the aftereffects of the previous discharges, since it uses the time derivative of the plasma density.

A piezo-valve has been inserted inside the vacuum vessel of LHD, since the 6th experimental campaign started on 1 October 2002. In the experiment using the inserted piezo-valve, local increase of neutral particle pressure at the gas puff port was observed. Supported by this, a particle balance model has been analyzed. The recycling parameters given by the model indicate that the recycling phenomenon is not to be neglected in the fueling scenario of gas puffing. Especially in LHD plasmas, the recycling flux is considerably larger than the gas puff flux and it is no exaggeration to say that the plasma density is increased by the recycling flux. The role of recycling flux on the particle balance will be highlighted in this thesis.

In tokamaks, a number of impurity induced confinement improvement has been reported, i.e. Z-mode in ISX-B [35], RI-mode in TEXTOR-94 [36], TFTR [37], and DIII-D [38], where a small amount of noble gas was injected to the hydrogen or deuterium plasmas. On the other hand, the confinement property of LHD plasmas shows the gyro-Bohm nature [39, 40], where the energy confinement time inversely depends on the ion gyro-radius (see Appendix), and a recent study has pointed out the importance of the effective charge Z_{eff} that affects the averaged ion gyro-radius [41]. In this thesis, two examples of the exploration for the plasma confinement improvement by impurity gas puffing are discussed. At first, methane was used to reduce the metal impurity contamination. Secondary, neon was used to study the influence of the ion gyro-radius on the energy confinement and to see the RI-mode would take place in LHD. These are the good examples that show the flexibility and the importance of gas puffing in the plasma experiments.

Since Oct. 1999, LHD has been equipped with the carbon divertor tiles that cover the full trace of the divertor legs. The influx of metal impurities has been significantly reduced, while the emission from carbon ions has been increased. However, these influences of carbon

divertor tiles were conspicuous only just after the installation [42]. The methane mixed hydrogen gas-puff experiment has been carried out in LHD. Although the methane mixed discharges itself did not show clear differences compared with the hydrogen gas-puff discharges, only four discharges introducing ~ 20 $Pa \cdot m^3$ of methane (consisting of about 5×10^{21} of carbon atoms) caused the reduction of metal impurity emission, together with the improved confinement in the shot fueled by hydrogen ice-pellets. During methane discharges, the carbon impurities are piled on the wall, and the aftereffect of this carbon accumulation can last. This is what is called as the real time carbonization and can work to reduce the metal impurities. This technique was applied as the real time boronization in CHS, where a small amount of decaborane puffed into NBI-heated plasmas reduced the metal and oxygen impurities [43]. In this thesis, the effect of methane discharges on the confinement property is investigated through the transport analysis of pellet shots before and after methane discharges.

To investigate the effect of electric charge and mass of plasma ions on the energy confinement property, neon gas puff experiment has been carried out. Reduced ion number density resulted in the higher ion temperature than that obtained in hydrogen plasmas. Here, the electron energy confinement is highlighted to see the difference between the hydrogen and the neon plasmas. Although the gyro-Bohm model predicts significant difference between them due to the different ion gyro-radius, and reduction in the electron thermal diffusivity has been reported from RI-mode experiment in tokamaks, the global energy confinement of neon plasmas is similar to that of hydrogen plasmas in LHD. Results of neon gas puff experiments are also given in this thesis.

On the other hand, gas puffing is not capable of the direct fueling into the hot plasma core, which is needed for the fusion reactor. One of the possible methods is the CT injection, where a high-density magnetized plasmoid is accelerated and injected into the plasma core. CT injection has been carried out in small / medium size tokamaks. However, it has not been obvious if this can be applied to the large helical plasmas. The magnetic pressure working on the CT surface determines the motion of CT in the magnetic field. Therefore, a CT traces three-dimensional orbit in LHD, reflecting the helical magnetic pressure profile as will be shown. This three-dimensional nature makes it possible to control the plasma density profile, and to deposit the momentum parallel to the magnetic field. The confinement improvement can be expected if the plasma rotation is to be induced by CT injection.

A CT of spheromak-type magnetic configuration is formed using co-axial plasma gun and accelerated by the acceleration electrode connected to the formation electrode of the same axis. This is called two-stage acceleration method. A two-stage co-axial magnetized

plasma gun named SPICA, which is an acronym of SPheromak Injector using Conical Accelerator, has been developed for LHD. Cone shape is adopted in the design of acceleration electrode to compress the CT and achieve the high magnetic field and/or the high density. Point-model is introduced to describe the motion of current-sheet inside the acceleration electrode. The conical acceleration electrode is designed after the point-model simulation. Technically, the critical pass of CT injection in LHD lies in the long-distance transfer of CT. The distance from the LHD port to the plasma center is about 4 m in LHD. Since such a long distance transfer has not been reported in the world, it is necessary to carry out the experiment for proof. Two-stage acceleration experiments have been carried out on SPICA. The most important objectives of SPICA is to generate and accelerate a high-density CT, and to demonstrate the long-distance transfer of ~ 4 m.

In chapter 2, we investigate the fueling efficiency of gas puffing on LHD. The role of recycling on the particle balance in LHD plasma is also discussed. Experimental results of hydrogen and helium gas puff discharges are used there. Other than these, methane and neon gas puff discharges have been performed on LHD, to study the effect of impurities on the confinement properties. Favorable effect of methane discharges observed in LHD pellet shots and the global electron energy confinement in neon gas puff discharges is analyzed and presented in chapter 3. Development of a CT injector for LHD is described in chapter 4, which consists of the CT orbit calculation in LHD magnetic fields, design study of the co-axial plasma gun named SPICA, and experimental results of SPICA. In chapter 5, conclusions of this thesis are summarized.

References

[1] J. Miyazawa et al., J. Nucl. Mater. **313-316**, 534 (2003).

[2] H.F. Dylla et al., J. Nucl. Mater. **111&112**, 211 (1982).

[3] K. Yamada et al., Nucl. Fusion **27**, 1203 (1987).

[4] R. Maingi et al., J. Nucl. Mater. **241-243**, 672 (1997).

[5] TFR group (presented by M.H. Achard), J. Nucl. Mater. **111&112**, 199 (1982).

[6] H.-M. Mayer et al., J. Nucl. Mater. **111&112**, 204 (1982).

[7] J. Ehrenberg et al., J. Nucl. Mater. **176&177**, 226 (1990).

[8] ITER Physics Expert Group on Divertor et al., Nucl. Fusion **39**, 2391 (1999).

[9] Lianghua Yao et al., Nucl. Fusion **38**, 631 (1998).

[10] Lianghua Yao et al., Nucl. Fusion **41**, 817 (2001).

[11] Xiang Gao et al., Nucl. Fusion **40**, 1875 (2000).

[12] Xiang Gao et al., Phys. Plasmas **7**, 2933 (2000).

[13] B. Pégourié et al., J. Nucl. Mater. **313-316**, 539 (2003).

[14] J. Bucalossi et al., Proc. 29th EPS on Plasma Phys. and Control. Fusion (Montreux, 2002) O-2.07.

[15] J. Bucalossi et al., IAEA-CN-94/P4-04.

[16] P. T. Lang et al., Phys. Rev. Lett. **79**, 1487 (1997).

[17] Sakamoto R. et al., Nucl. Fusion **41**, 381 (2001).

[18] P. Gohil, K. H. Burrell and T. H. Osborne, Nucl. Fusion **38** (1998) 425.

[19] Y. Koide, K. H. Burrell, B. W. Rice and T. Fujita, Plasma Phys. Control. Fusion **40**, 97 (1998).

[20] K. Ida, et al., Phys. Rev. Lett. **68**, 182 (1992).

[21] R. Raman et al., Phys. Rev. Lett. **73**, 3101 (1994).

[22] M. R. Brown and P. M. Bellan, Nucl. Fusion **32**, 1125 (1992).

[23] J. Yee and P. M. Bellan, Nucl. Fusion **38**, 711 (1998).

[24] J. H. Hammer, J. L. Eddleman, C. W. Hartman, H. S. McLean and A. W. Molvik, Phys. Fluids B **3**, 2236 (1991).

[25] J. Eddleman et al., "Final Report on the LLNL Compact Torus Acceleration Project", UCRL-ID-120238, Lawrence Livermore National Laboratory (Mar. 1995).

[26] J. H. Hammer, C. W. Hartman, J. L. Eddleman, H. S. McLean, Phys. Rev. Letters **61**, 2843 (1988).

[27] Charles W. Hartman and James H. Hammer, Phys. Rev. Lett. **48**, 929 (1982).

[28] P. B. Parks, Phys. Rev. Lett. **61**, 1364 (1988).

[29] W. A. Newcomb, Phys. Fluids B **3**, 1818 (1991).

[30] L. J. Perkins, S. K. Ho and J. H. Hammer, Nucl. Fusion **28**, 1365 (1988).

[31] A. Iiyoshi et al., Nucl. Fusion **3**, 1245 (1999).

[32] O. Motojima et al., Phys. Plasmas **6**, 1843 (1999).

[33] M. Fujiwara et al., Plasma Phys. Control. Fusion **41**, B157 (1999).

[34] A. Komori et al., Plasma Phys. Control. Fusion **42**, 1165 (2000).

[35] E. A. Lazarus et al., J. Nucl. Mater. **121**, 61 (1984).

[36] A. M. Messiaen et al, Phys. Rev. Lett. **77**, 2487 (1996).

[37] K. W. Hills et al., Phys. Plasmas **6**, 877 (1999).

[38] G. R. McKee et al., Phys. Plasmas **7**, 1870 (2000).

[39] H. Yamada et al., Phys. Rev. Lett. **84**, 1216 (2000)

[40] H. Yamada et al., Nucl. Fusion **41**, 901 (2001).

[41] J. Miyazawa et al., paper presented at the 28th EPS Conference on Controlled Fusion and Plasma Physics, Madeira, p4.043 (2001).

[42] S. Morita et al., Phys. Scr. **T91**, 48 (2001).

[43] A. Sagara et al., J. Nucl. Mater. **241-243**, 972 (1997).

Chapter 2 Gas Puff Experiments on LHD

This chapter discusses the fueling efficiency of gas puffing and the particle balance in LHD. At first, equations to describe the particle balance are introduced in section 2.1. Secondary, the fueling efficiency of gas puffing is estimated in section 2.2. The role of recycling flux in the particle balance is investigated in section 2.3. Summary of this chapter is given in the last section.

2.1. Equations

2.1.1. Effective fueling efficiency

For precise and reliable plasma density control by gas puffing, it is important to understand the response of dN_e/dt to Φ_{puff}, where N_e is the total number of the electrons confined in the plasma and Φ_{puff} is the electron flux supplied by gas puffing. Here we define the effective fueling efficiency, α_{eff}, as

$$\alpha_{eff} \equiv \frac{dN_e/dt}{\Phi_{puff}}. \tag{2.1.1}$$

The conventional method to obtain the fueling efficiency of gas puffing, α_{puff}, is to compare dN_e/dt before and after the termination of the gas puffing with Φ_{puff} [1, 2];

$$\alpha_{puff} \approx \frac{(dN_e/dt)_{before} - (dN_e/dt)_{after}}{\Phi_{puff} - 0}. \tag{2.1.2}$$

Neglecting $(dN_e/dt)_{after}$ in Eq. (2.1.2), one obtains Eq. (2.1.1). However, as will be discussed later, Eq. (2.1.2) assumes that the other particle sources such as the recycling flux are insensitive to the gas puffing and not changing before and after the gas puff termination. In this chapter, we are showing that the recycling flux does change due to the gas puffing. Therefore, α_{puff} determined by Eq. (2.1.2) is not reliable. This is why we call the parameter defined by Eq. (2.1.1) the 'effective' fueling efficiency.

2.1.2. Particle balance model

The particle balance model that describes the time derivative of the electron number density in gas-fueled plasmas heated by the neutral beam (NB) injection can be expressed as

$$\frac{\mathrm{d}N_\mathrm{e}}{\mathrm{d}t} = \alpha_\mathrm{puff}\Phi_\mathrm{puff} + \alpha_\mathrm{div}R_\mathrm{div}\Gamma_\mathrm{div} + \alpha_\mathrm{wall}R_\mathrm{wall}\Gamma_\mathrm{wall} + \Phi_\mathrm{NB} - \frac{N_\mathrm{e}}{\tau_\mathrm{p}}. \tag{2.1.3}$$

The particle sources are: Φ_puff times α_puff; the recycling flux from the divertor plate (or the vacuum vessel wall), which is a product of the recycling coefficient, R_div (R_wall), and the outflow of the electrons, Γ_div (Γ_wall), times the fueling efficiency of the recycling flux, α_div (α_wall); and the direct fueling component by the neutral beam (NB) injection, Φ_NB. The particle loss is simply expressed as $-N_\mathrm{e}/\tau_\mathrm{p}$, where τ_p is the particle confinement time.

Experimentally, Φ_puff is mainly used to control the plasma density, or $N_\mathrm{e}' = \mathrm{d}N_\mathrm{e}/\mathrm{d}t$. The response of N_e' to Φ_puff can be directly related to α_puff;

$$\alpha_\mathrm{puff} \approx \frac{\partial N_\mathrm{e}'}{\partial \Phi_\mathrm{puff}}, \tag{2.1.4}$$

as long as the other parameters are insensitive to the change of Φ_puff. In order to estimate α_puff by Eq. (2.1.4), the relations below should be satisfied;

$$\frac{\partial(\alpha_\mathrm{div}R_\mathrm{div}\Gamma_\mathrm{div})}{\partial \Phi_\mathrm{puff}} \ll 1, \tag{2.1.5}$$

$$\frac{\partial(\alpha_\mathrm{wall}R_\mathrm{wall}\Gamma_\mathrm{wall})}{\partial \Phi_\mathrm{puff}} \ll 1, \tag{2.1.6}$$

$$\frac{\partial \Phi_\mathrm{NB}}{\partial \Phi_\mathrm{puff}} \ll 1, \tag{2.1.7}$$

$$\frac{\partial(N_\mathrm{e}/\tau_\mathrm{p})}{\partial \Phi_\mathrm{puff}} \ll 1. \tag{2.1.8}$$

As will be shown later, typical orders of Φ_NB, Φ_puff, and Γ_div in LHD are 10^{20}, 10^{21}, and 10^{22}, respectively, while that of N_e' ranges from 10^{20} to 10^{22}, in the unit s^{-1}. Therefore, it is more difficult to satisfy Eq. (2.1.5), than Eq. (2.1.7). As for Eq. (2.1.6), we have no information about R_wall and/or Γ_wall itself to date. In this study, we refer to the H_α signal to assure that the

recycling term of $R_{wall}\Gamma_{wall}$ is constant. The H_α signal is proportional to the neutral particle density in our experimental regime [3]. To confirm the last criterion, Eq. (2.1.8), it is necessary to obtain τ_p, which also has not been estimated experimentally. Meanwhile, the energy confinement time, τ_E^{dia}, can be derived from the diamagnetic plasma stored energy, W_p^{dia}, as $\tau_E^{dia} = W_p^{dia} / (P_{NB} - dW_p^{dia} / dt)$, where P_{NB} is the NB heating power. Typical order of τ_E^{dia} is 0.1 s in LHD. In this study, we assume that the behavior of τ_p resembles to that of τ_E^{dia}, and use τ_E^{dia} to see whether Eq. (2.1.8) is satisfied or not.

2.1.3. Recycling coefficient

If one can neglect the term of $\alpha_{wall}R_{wall}\Gamma_{wall}$ in Eq. (2.1.3), it becomes possible to estimate the divertor-recycling coefficient R_{div}. In such a case, Γ_{div} can be expressed by the equation below;

$$\Gamma_{div} = (1-\alpha_{puff})\Phi_{puff} + (1-\alpha_{div})R_{div}\Gamma_{div} + \frac{N_e}{\tau_p}. \tag{2.1.9}$$

In other words, Γ_{div} is the sum of the residual part of Φ_{puff} that is not fueled to the plasma, the residual part of the recycling flux, $R_{div}\ \Gamma_{div}$, that is also not fueled, and the particle loss of N_e/τ_p.

The sum of Eqs. (2.1.3) and (2.1.9) gives the total particle balance equation as;

$$\frac{dN_e}{dt} = \Phi_{puff} + \Phi_{NB} - (1-R_{div})\Gamma_{div}. \tag{2.1.10}$$

This means that the electrons supplied by gas puffing or NB injection increase the electron density, and the residual part, which is not recycled, is absorbed by the divertor plates. Note that if $R_{div} = 1$ and $\Phi_{puff} \gg \Phi_{NB}$, Eq. (2.1.10) becomes

$$\frac{dN_e}{dt} \approx \Phi_{puff}. \tag{2.1.11}$$

Then α_{eff} is nearly equal to 1.

The divertor-recycling coefficient R_{div} can be derived from Eq. (2.1.10), as;

$$R_{div} = 1 - \frac{(\Phi_{puff} + \Phi_{NB} - dN_e/dt)}{\Gamma_{div}}. \tag{2.1.12}$$

It is straightforward to estimate R_{div}, since the right-hand-side of Eq. (2.1.12) is composed of the measurable parameters. In section 2.3, experimentally obtained R_{div} together with the recycling flux $R_{div}\,\Gamma_{div}$ will be shown.

In the particle balance model of Eq. (2.1.3), the fueling term by the recycling flux is given by $\alpha_{div} R_{div} \Gamma_{div}$. This means that all of the particles reflected by the divertor tiles are not necessarily returned to the plasma. Meanwhile, the conventional understanding of the recycling coefficient is that it expresses the ratio of the returned particles after the interaction with the wall material. In such a case, $\alpha_{div}\ R_{div}$ should be substituted by a recycling coefficient of R_{div}' as below,

$$\frac{dN_e}{dt} = \alpha_{puff}\Phi_{puff} + R_{div}'\Gamma_{div} + \Phi_{NB} - \frac{N_e}{\tau_p}. \qquad (2.1.3)'$$

The divertor flux in this case is given by

$$\Gamma_{div} = (1-\alpha_{puff})\Phi_{puff} + \frac{N_e}{\tau_p}. \qquad (2.1.9)'$$

The sum of Eqs. (2.1.3)' and (2.1.9)' gives the same expression of R_{div}' as R_{div} in Eq. (2.1.12). Therefore, the recycling coefficient discussed below does not contradict the conventional recycling coefficient.

References

[1] H.F. Dylla et al., J. Nucl. Mater. **111&112**, 211 (1982).

[2] K. Yamada et al., Nucl. Fusion **27**, 1203 (1987).

[3] L.C. Johnson, E. Hinnov, J. Quant. Spectrosc. Radiat. Transfer. **13**, 333 (1973).

2.2. Fueling efficiency of gas puffing

2.2.1. Experimental results

Gas puffing is routinely used on LHD to control the electron density. The gas puff system in LHD consists of eleven piezo valves distributed to three lower-ports as shown in Fig. 2.2.1. Three kinds of piezo valves, of which the hydrogen flow rate at the maximum are 5, 50, and 100 Pa·m^3/s, respectively, are utilized in the system. Density ramp up experiment has been carried out on LHD. The major radius, R_{ax}, and the strength of the magnetic field, B_0, at the magnetic axis were fixed to 3.6 m and 2.8 T, respectively. One piezo valve set at 3.5L port (see Fig. 2.2.1), of which the hydrogen flow rate at the maximum is 50 Pa·m^3/s, was used throughout the experiment. Discharges were initiated by the electron cyclotron heating (ECH) and then sustained by the neutral beam (NB) injection. Two or three beam lines of high-energy negative-ion based NB systems supplied ~ 3.5 or ~ 5 MW of the heating power. The P_{NB} is estimated from the direct heat-load measurement of NB shine-through power on the armor plate [1]. Electrostatic probes set on the divertor tiles were used to measure the electron temperature, T_e^{div}, and the electron density, n_e^{div} [2]. Using these parameters, Γ_{div} is estimated as the multiple of the ion saturation current density and the assumed wetted aria of 2 m^3. The H_α signals measured at two different toroidal positions showed similar behavior in this experiment. From this observation, we assume the toroidal uniformity of neutral particle behavior and use one H_α signal in the analysis below. LHD is equipped with ten sets of magnetic coils located at every upper and lower port [3]. The magnetic field generated by these coils interferes in the main helical magnetic field and is able to control the width of the magnetic island (m/n = 1/1 or 2/1, where m and n are the poloidal and toroidal mode number). Without using these coils, there naturally exists the m/n = 1/1 magnetic island in LHD. The m/n = 1/1 magnetic island is located around $\rho \sim 0.9$, where $\rho = r/a$ is the normalized minor radius [3, 4].

Here, five discharges from the series of the density ramp-up experiment are selected to examine Eq. (2.1.4) and estimate α_{puff}. These five discharges consist of the plasmas heated by different P_{NB}, with the natural/cancelled/extended magnetic island of m/n = 1/1. Typical parameters of the five discharges are summarized in Table 2.2.1. An example of the influence of the magnetic island on the plasma performance can be seen in the table; i.e. the maximum of W_p^{dia} is smaller in the shot with the extended magnetic island (#28189) than in the shot

with the cancelled magnetic island (#28179), although the other parameters such as P_{NB} and the line-averaged electron density, $\bar{n}_e$, are similar in both shots. Waveforms from one of the five discharges are shown in Fig. 2.2.2. The density feedback starts at 1 s, where $\bar{n}_e$ is $\sim 2 \times 10^{19}$ m^{-3}. ECH is stopped before 0.8 s and then NB injection alone heats the plasma. The density is increased to $\sim 5 \times 10^{19}$ m^{-3} during 1.5 – 3 s, by the feedback control of Φ_{puff}. This ramp up phase is indicated as " Phase I ", in Fig. 2.2.2. After the density reaches to $\sim 5 \times 10^{19}$ m^{-3}, Φ_{puff} is reduced at 3 – 4 s. This phase is indicated as " Phase II ". This ramp up scheme is also used in the other four discharges. Therefore the Phase I and the Phase II correspond to the same times in all of the five shots, in the discussion below.

2.2.2. Fueling efficiency

As can be seen in Fig. 2.2.2, $N_e' = dN_e/dt$ well correlates with Φ_{puff} during Phase II, while these are not correlated during Phase I. Instead, Φ_{puff} and Γ_{div} show similar increase during the Phase I. This suggests that the criterion of Eq. (2.1.5) is not satisfied here, and Eq. (2.1.4) is not adequate to estimate α_{puff}. The H_α signal also increases with Φ_{puff} during the Phase I, suggesting Eq. (2.1.6) is not satisfied in this phase. Although it is natural that $\bar{n}_e$ increases with Φ_{puff} during the Phase I, the constant nature of the τ_E^{dia} suggests the violation of Eq. (2.1.8) at this phase. The linear correlation between Φ_{puff} and the reference parameters (N_e', Γ_{div}, H_α, Φ_{NB}, and N_e/τ_E^{dia}) is calculated to estimate α_{puff} by Eq. (2.1.4), while confirming the four criteria of Eqs. (2.1.5) - (2.1.8). Here, we investigate two ensembles of the data from Phase I and Phase II of the five discharges. Note that this ensemble method is suitable to find out a robust correlation. For instance, a large correlation factor can be obtained between any two irreverent parameters in a discharge, only if these two are monotonically changing in time. In the data ensemble composed from several discharges with different experimental conditions, such a feigned correlation tends to disappear.

The linear correlation coefficient, R_c, is summarized in Table 2.2.2. At the Phase I, the linear correlation between Φ_{puff} and N_e' is weak and it is not possible to estimate α with Eq. (2.1.2). At the same phase, strong correlation between Φ_{puff} and H_α (or N_e/τ_E^{dia}) is observed, which indicates the violation of Eq. (2.1.4) (or Eq. (2.1.6)). Furthermore, there is a possibility that R_{div} is changing since the electron temperature at the divertor, T_e^{div}, is decreasing during Phase I (see Fig. 2.1.1). As for the Phase II, on the other hand, there

recognized is a strong correlation of $R_c = 0.95$ between Φ_{puff} and N_e'. Meanwhile, other reference parameters indicate small linear correlation factors of less than 0.3, which assure the criteria of Eqs. (2.1.5) - (2.1.8). These results support the validity of applying Eq. (2.1.4) for the data from the Phase II. The relation between Φ_{puff} and N_e' is shown in Fig. 2.2.3. The least square fit of N_e' with Φ_{puff} gives the linear equation below;

$$N_e' = 0.12 \times \Phi_{puff} - 12, \tag{2.2.1}$$

where the unit is 10^{19} s^{-1}. Comparing Eq. (2.2.1) with Eq. (2.1.3) (or, Eq. (2.1.4)), the fueling efficiency is obtained from the slope of Eq. (2.2.1); i.e. $\alpha_{puff} = 0.12$. The offset of Eq. (2.2.1) (= 12) corresponds to the sum of the other terms than $\alpha_{puff}\ \Phi_{puff}$, in the right-hand-side of Eq. (2.1.3).

As seen in Fig. 2.2.3, all of the five discharges have similar slopes as Eq. (2.2.1), although the offsets are different. The slopes (offsets) individually calculated for the five discharges at Phase II are; 0.12 (-8.3), 0.13 (-16), 0.11 (-12), 0.10 (-8.3) and 0.14 (-21), for #28163, #28166, #28178, #28179, and #28189, respectively. Note that the slopes calculated individually are identical to that of Eq. (2.2.1) within 20 %. This suggests that α_{puff} is insensitive to the heating power or the existence of the magnetic island, within the experimental conditions studied here. The fueling efficiency of about 10 % obtained here is similar to that observed in diverted tokamaks [5], although the estimation method is different. As for the offsets, it seems to change according to the experimental condition. Recycling might be the one of important keys to understand this.

2.2.3. Discussion

Where does the residual gas, which corresponds to nearly 90 % of the fueled gas, disappear? In LHD, typical order of the neutral pressure during the NB heated discharge is 10^{-3} Pa [6], and is much smaller than that expected from the integrated gas puff flux (10 – 100 Pa· m^3) and the volume of vacuum vessel (210 m^3). The maximum pumping speed of the LHD vacuum system is less than 200 m^3/s, and the resultant exhaust flux is also smaller than the gas puff flux. One of the possible scenarios to answer this is that the residual gas is absorbed by the plasma facing materials, such as the divertor tiles and the first wall of the vacuum vessel.

References

[1] M. Osakabe et al., Rev. Sci. Instrum. **72**, 590 (2001).

[2] S. Masuzaki et al., Nucl. Fusion **42**, 750 (2002).

[3] A. Komori et al., Plasma Phys. Control. Fusion **42**, 1165 (2000).

[4] N. Ohyabu et al., Phys. Rev. Lett. **84**, 103 (2000).

[5] ITER Physics Expert Group on Divertor et al., Nucl. Fusion **39**, 2391 (1999).

[6] H. Suzuki et al., J. Nucl. Mater. **313 - 316**, 297 (2003).

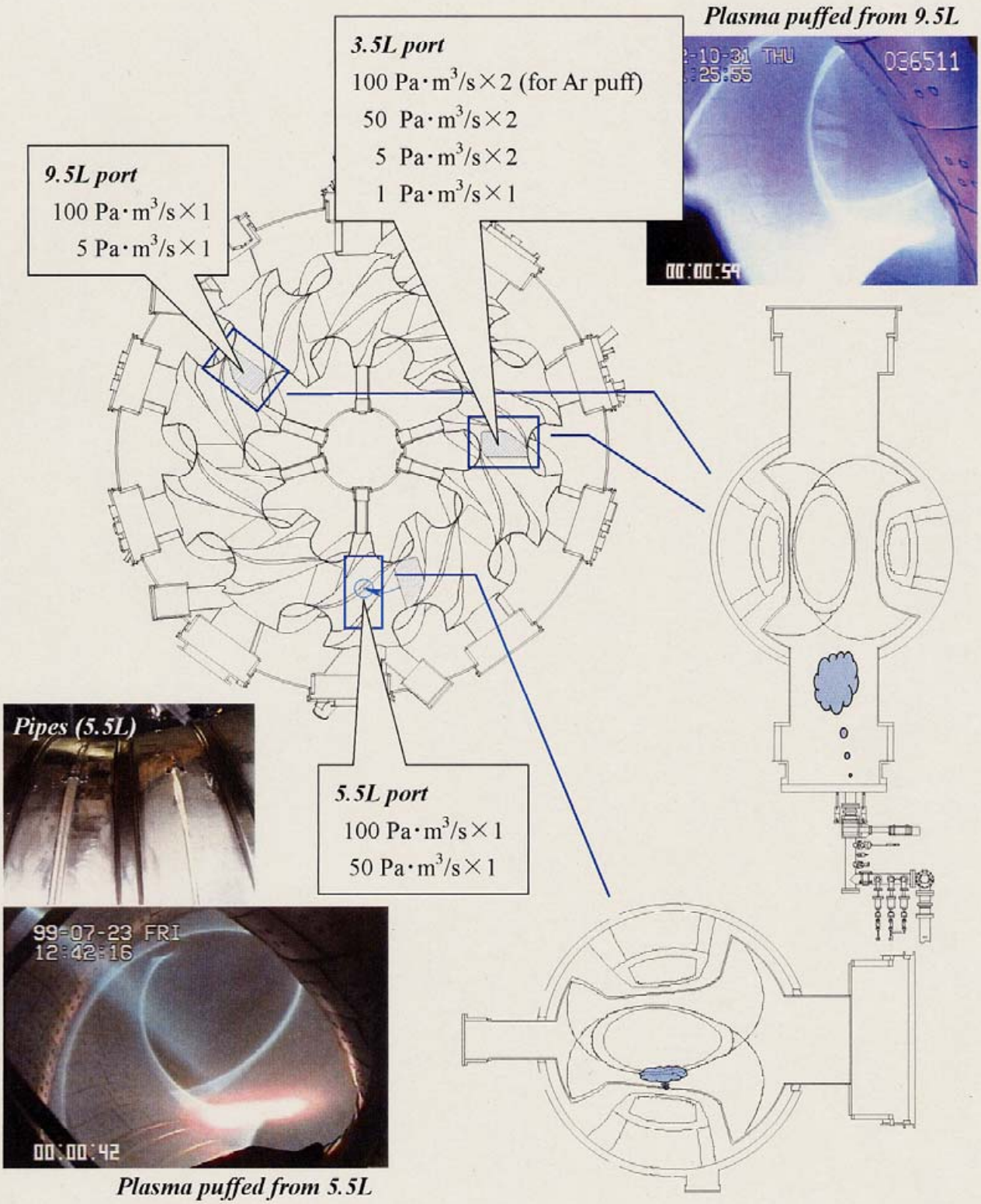

Fig. 2.2.1. Distributions of piezo-valves for gas puffing. At the 5.5L port, gas is fed through three narrow pipes of which the inner radius is 10 mm and the length is about 5 m.

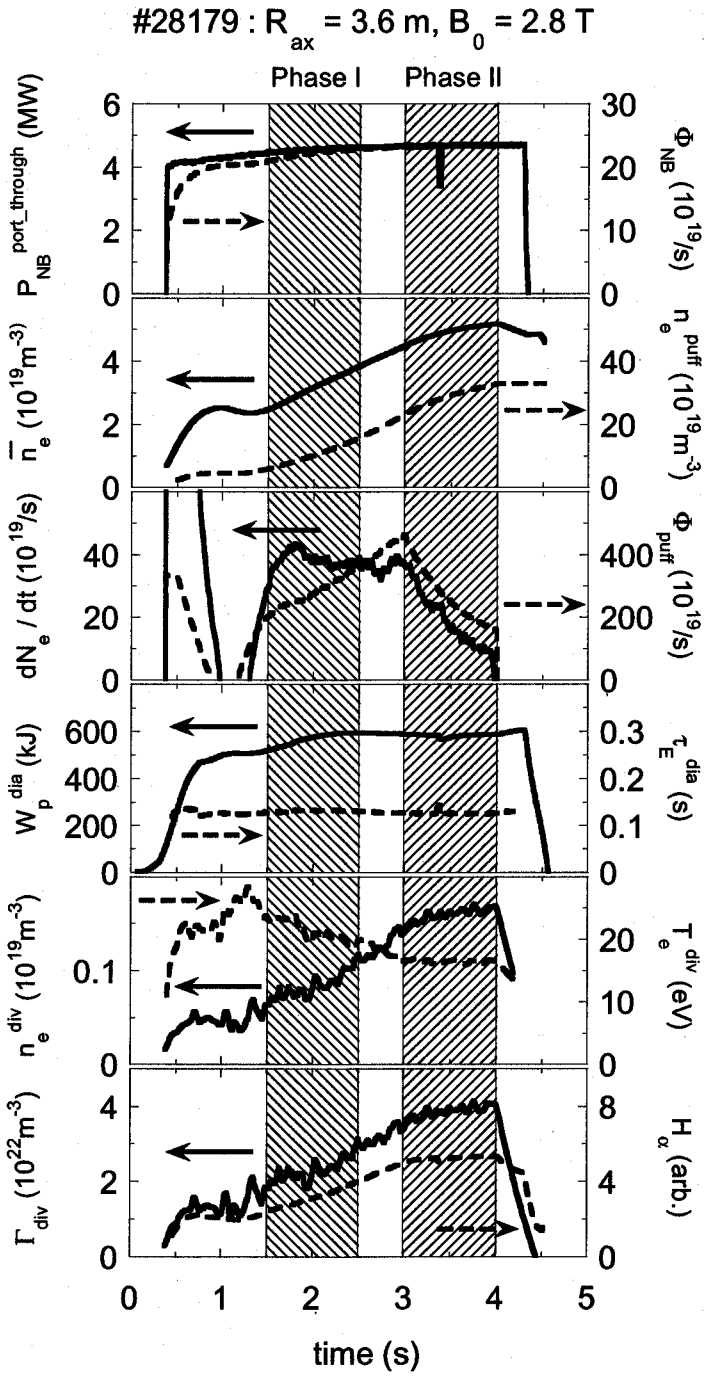

Fig. 2.2.2. Waveforms of typical parameters in the density ramp up discharge of #28179. Depicted from the top to the bottom are; the port through power of NB, $P_{NB}^{port\_through}$, and Φ_{NB}; $\bar{n}_e$ and the electron density calculated from the integrated particle number supplied by gas puffing with assumption of 100 % efficiency, n_e^{puff}; $N_e' = dN_e/dt$ and Φ_{puff}; W_p^{dia} and τ_E^{dia}; n_e^{div} and T_e^{div}, measured by the electrostatic probes on the divertor tile; Γ_{div} and H_α signal. The density ramp up phase and the latter phase are hatched and denoted as " Phase I " and " Phase II ", respectively.

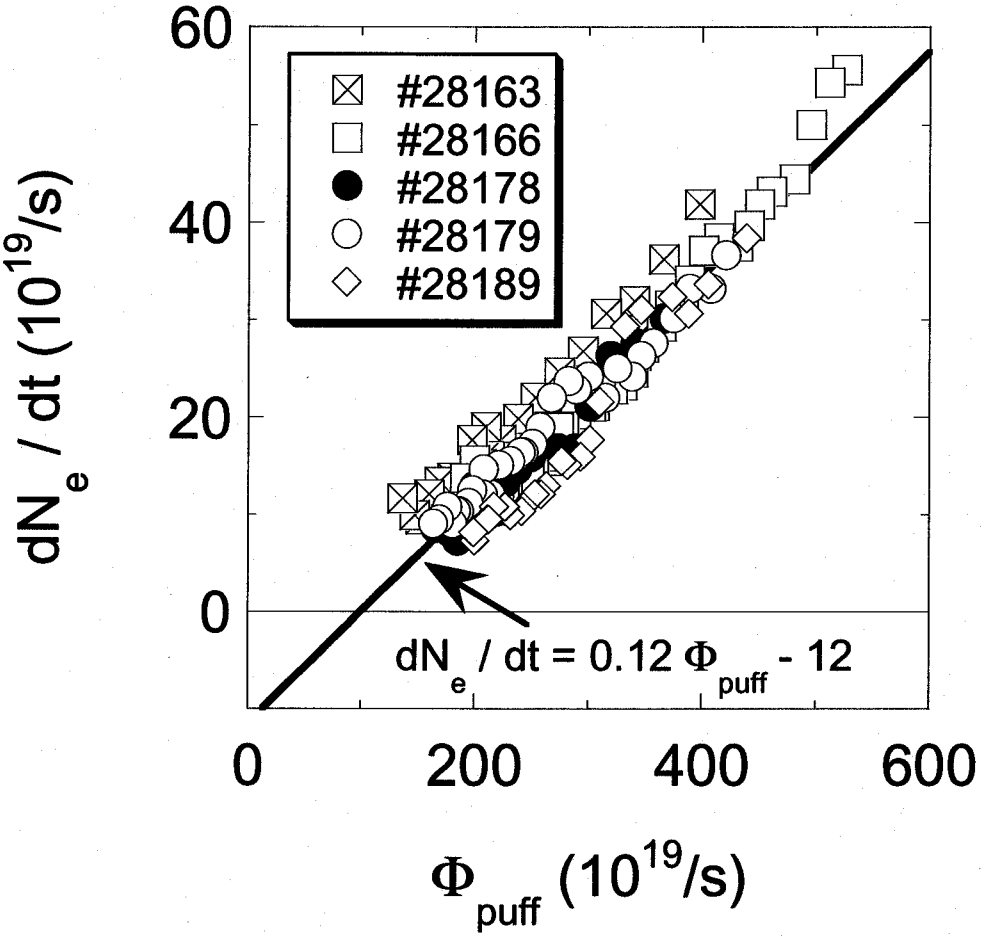

Fig. 2.2.3. Relation between Φ_{puff} and $N_e' = dN_e/dt$. Shown are the data from the Phase II of five discharges with different experimental conditions. Solid line is the least square fit of the data ensemble (Eq. (2.2.1)).

Table 2.2.1. Summary of the typical parameters of the five discharges selected to estimate the fueling efficiency. $(P_{NB})_{max}$, $(\bar{n}_e)_{max}$, and $(W_p^{dia})_{max}$ are the maximum of P_{NB}, $\bar{n}_e$, and W_p^{dia}, respectively. The arrow (←) denotes that the experimental condition is identical to the left column.

Experimental condition	Shot number				
	#28163	#28166	#28178	#28179	#28189
R_{ax} (m)	3.6	←	←	←	←
B_0 (T)	2.8	←	←	←	←
Magnetic island	Natural	←	Canceled	←	Extended
$(P_{NB})_{max}$ (MW)	3.5	5.0	4.7	4.7	4.7
$(\bar{n}_e)_{max}$ ($10^{19}m^{-3}$)	5.2	5.9	4.5	5.2	5.2
$(W_p^{dia})_{max}$ (kJ)	535	661	606	606	526

Table 2.2.2. Linear correlation coefficients R_c between Φ_{puff} and the reference parameters (N_e', Γ_{div}, H_α, Φ_{NB}, and N_e/τ_E^{dia}), at Phase I and Phase II.

Reference parameter	R_c	
	Phase I	Phase II
N_e'	0.49	0.95
Γ_{div}	0.53	0.17
H_α	0.80	0.24
Φ_{NB}	0.51	0.20
N_e/τ_E^{dia}	0.91	0.08

2.3. Role of recycling flux on gas fueling

In the former section, the fueling efficiency of gas puffing in LHD has been estimated as ~ 12 % [1]. Other than the fueling efficiency, the recycling phenomenon plays an important role in the particle balance of fusion plasma systems. Especially in LHD plasmas, the recycling flux is considerably larger than the gas puff flux. Therefore it is no exaggeration to say that the plasma density is increased by the recycling flux, as will be discussed later. This section discusses the particle balance in LHD plasmas, based on the results from the gas puff experiments using the inserted piezo-valve.

2.3.1. Experimental setup

Since the 6th experimental campaign started on 1 Oct. 2002, a piezo-valve has been inserted inside the LHD vacuum vessel. Figure 2.3.1 shows the schematic of this device and its location in LHD. The relation between the gas puff flux and the control voltage has been calibrated. In the experiment, the control voltage is always monitored to estimate the electron flux supplied by gas puffing, Φ_{puff}. The maximum hydrogen flow rate of the piezo-valve is 60 Pa·m^3/s ($\Phi_{puff} = 2.9 \times 10^{22}$ s^{-1}), when the absolute backpressure of the piezo-valve is 0.2 MPa. The time for full open to full close, or vice versa, of the piezo-valve is less than 1 ms, according to the result of test run, where the same kind of piezo-valve was used. Linear motion system of 0.5 m stroke is equipped and the vertical position of the piezo-valve is changeable. Throughout the experiments in this study, the piezo-valve was located at the upper position (or the 'private region' in relation to the divertor legs).

Also shown in Fig. 2.3.1 are the locations of the measurements discussed below. Two Fast Ion Gauges (FIG) [2] measure the neutral particle pressure at different location. One FIG is set inside the same upper-port as the gas puff device and the neutral particle pressure measured there is denoted as p_1. Another FIG is set inside the inner-port with a separation of 1.5/10 toroidal sections from the gas puff port, which measures p_0. The particle (electron) flux onto the divertor plates, Γ_{div}, is measured by the Langmuir probe array installed on the divertor plates [3]. The ion saturation current density times the assumed wetted area of 2 m^2 is defined as Γ_{div}, in this study. The electron density profile is measured by the multi channel far-infra-red (FIR) interferometer [4]. The line-averaged density, $\bar{n}_e$, is obtained from the FIR data of a central chord that passes near the magnetic axis. Since the electron density

profile is flat in the gas puff discharges, the total number of electrons, N_e, is estimated as $N_e = \bar{n}_e \times V_p$, where V_p is the plasma volume. The electron temperature at the plasma center, T_{e0}, and that at $\rho = 0.9$ ($\rho = r/a$ is the normalized minor radius), $T_{e(\rho=0.9)}$, is measured by the Thomson scattering [5]. The ion temperature at the plasma core, T_{i0}, is measured by the Doppler broadening of a line spectrum (Ar XVII) emitted from argon ions [6].

In this study, we focus on the plasmas heated by the negative-ion based neutral beam (NB) injection. The beam energy, E_{NB}, ranges from 140 to 170 keV. The NB heating power, P_{NB}, is estimated from the NB port-through power and the direct heat-load measurement of NB shine-through power on the armor plate [7]. The particle flux supplied by NB, Φ_{NB}, is derived from these P_{NB} and E_{NB}. Since E_{NB} is high, the order of Φ_{NB} is 10^{20} s^{-1} and much less than the typical Φ_{puff} in this study.

2.3.2. Hydrogen gas puff experiments

Waveforms from the typical hydrogen gas puff discharge are depicted in Fig. 2.3.2 (a). Rectangular pulses are used to open the piezo-valve. The time derivative of the total number of electrons, dN_e/dt, sharply increases with Φ_{puff} after a short delay of ~ 10 ms, which is larger than that obtained in the test run. Although the reason of the dead time is not understood at this moment, it is not the fatal problem in this study since the gas puff pulse length is much longer than the dead time. Two kinds of the neutral particle pressure, p_0 and p_1, are plotted in Fig. 2.3.2 (b), together with $\bar{n}_e$. Modulations corresponding to the gas puff pulses can be seen in $\bar{n}_e$ and p_1. Since p_1 is measured at the gas puff port, each of the peaks in p_1 can be taken as a part of Φ_{puff} that is not ionized. As for p_0, it gradually increases with $\bar{n}_e$, and no clear sharp increase due to the gas puff pulse is observed. The correlation between p_0 and $\bar{n}_e$ will be discussed again later. Well after the last gas puff pulse (> 3.2 s), p_0 and p_1 show similar behavior. After the plasma disappears (~ 3.5 s), the pressure abruptly increases (~ 4.0 s) and then decreases again (> 4.2 s) with a reasonable rate as estimated from the vacuum pumping speed. Although the physical scenario that can explain the abrupt pressure increase is not fully understood to date, the similar absolute values of p_0 and p_1 indicate that the discrepancy between p_0 and p_1 before 3.2 s is due to the gas puffing and not to the systematic errors of FIGs.

The insensitive behavior of p_0 suggests that the pressure rise due to gas puffing is

localized around the gas puff port. The neutrals that are not ionized cause the increase in p_1. Assuming that the pressure rise as p_1 is localized at the upper-half of the 1/10 toroidal section of LHD vacuum vessel, the neutral particle flux is calculated as $(dp_1/dt) \times V_1$, where $V_1 = (210 - V_p) / 20$, and 210 m^3 is the volume inside the LHD vacuum vessel. Comparison between Φ_{puff} and $(dp_1/dt) \times V_1$ in the unit of $Pa \cdot m^3/s$ is shown in Fig. 2.3.2 (c). The absolute value of $(dp_1/dt) \times V_1$ is less than 10 % of Φ_{puff}. Residual particles of more than 90 % of Φ_{puff} are ionized and fueled to the plasma.

Other important fluxes in the particle balance equations (see section 2.2.4) are Γ_{div} and Φ_{NB}, which are also depicted in Fig. 2.3.2 (c). As mentioned before, Φ_{NB} is small since the high-energy NB is adopted in LHD. The order of Φ_{NB}, dN_e/dt, and Φ_{puff} are 10^{20} s^{-1}, 10^{21} s^{-1}, and 10^{22} s^{-1}, respectively. The largest flux in this experiment is Γ_{div}, of which the typical order is 10^{23} s^{-1}.

2.3.3. Effective fueling efficiency

The relation between dN_e/dt and Φ_{puff} is depicted in Fig. 2.3.3, where the closed (open) circles are the data extracted from hydrogen (helium) gas puff discharges and the open squares are the data analyzed in section 2.2 (denoted as 'ref. 1'). In the hydrogen gas puff discharges, α_{eff} is distributed from 10 % to 20 % for the most part, and the maximum of α_{eff} reaches 50 %. In the helium gas puff discharges, larger α_{eff} of 20 – 100 % are obtained. As for the data from section 2.2, α_{eff} can be fitted by Eq. (2.2.1).

The density increase is not necessarily due to the gas puffing alone. Other particle sources such as Φ_{NB} or the recycling fluxes should be considered. In section 2.2, the influence of other particle sources is carefully eliminated and the relation between dN_e/dt and Φ_{puff} is obtained as Eq. (2.2.1). In this case, the coefficient of 0.12 can be treated as the 'real' fueling efficiency of gas puffing. Returning to Fig. 2.3.3, the large α_{eff} possibly suffers from the influence of other particle sources. In section 2.2, a large α_{eff} of > 17 % also appears (see Fig. 2.2.1) at the phase where the influence of other particle sources cannot be neglected (denoted as 'Phase I' in the figure).

Large α_{eff} at the large Φ_{puff} regime is favorable from the viewpoint of achieving a high density in a short time. However, the large dispersion of α_{eff} is not favorable to establish the reliable density control method. In the following subsections, we will investigate the cause

of the large dispersion in α_{eff}.

2.3.4. Particle balance

The particle balance model has been introduced as Eq. (2.1.3) in section 2.1, where the ionization efficiency of the gas puff flux is assumed as 100 %. In the discharges discussed here, $\alpha_{wall} R_{wall} \Gamma_{wall}$ in Eq. (2.1.3) can be neglected since the absolute value of p_0, which indicates the pressure of the remaining neutral particles, is much smaller than p_1, which corresponds to the small part of Φ_{puff} (see Figs 2.3.2 (b) and (c), and note that the ionization efficiency is estimated as > 90 %).

Here, we are adopting one more important assumption for Γ_{div}, i.e. all of the outward particle fluxes from the plasma go to the divertor plate. Since the outward magnetic lines of force that have long connection length are connected to the divertor plates [3], this assumption is valid if the direct particle loss to the vacuum vessel wall due to the charge recombination is small enough to be neglected. This is not the case if the divertor is 'detached' and the electron temperature at the plasma periphery or the divertor leg decreases to less than a few eV. In LHD, however, clear divertor detachment has not been observed to date [3]. Then equations introduced in section 2.1.3 are valid and Eq. (2.1.12) can be used to estimate the recycling coefficient R_{div}. In the next subsection, experimentally obtained R_{div} together with the recycling flux $R_{div} \Gamma_{div}$ will be shown.

2.3.5. Recycling flux

The data depicted in Fig. 2.3.3 consisted of the discharges with different experimental conditions. For example, the axis of the vacuum magnetic field, R_{ax}, is varied from 3.5 to 3.75 m, and the magnetic field strength at the magnetic axis, B_0, ranges from 0.5 to 2.8 T. To eliminate the dependence of the parameters on these experimental conditions, we select the data using several criteria, i.e. R_{ax} = 3.5 m, B_0 = 2.854 T, and the NB port-through power is 6 or 7 MW. Furthermore, data is selected from successive discharges in one day, to minimize the influences of the wall condition of the vacuum vessel. The characteristics of the data selected according to these criteria are shown in Fig. 2.3.4, where the density dependence of the key parameters (P_{NB}, p_0, Γ_{div}, R_{div}, and $R_{div} \Gamma_{div}$ normalized by N_e) is summarized. A

typical discharge involved in Fig. 2.3.4 is #39931 shown in Fig. 2.3.2. Other data points are also extracted from the pulsed gas puff discharges such as #39931. In Fig. 2.3.4, shown are data during gas puffing (open and closed circles for the NB port-through power of 7 MW and 6 MW, respectively) and that between gas puff pulses (open squares, denoted as 'w/o gas puff', where the NB port-through power is 7 MW).

At the low-density regimes in LHD, the NB shine-through is not negligible and P_{NB} is smaller than the NB port-through power (Fig. 2.3.4 (a)). As has already been shown in Fig. 2.3.2 (b), p_0 increases with $\bar{n}_e$. The linear correlation between these two is robust and scarcely depends on P_{NB}, or the existence of gas puffing (Fig. 2.3.4 (b)). The linear dependence on $\bar{n}_e$ also can be recognized in Γ_{div} (Fig. 2.3.4 (c)). The relation between $\bar{n}_e$ and Γ_{div} is, however, not robust as p_0 and changes with the NB heating power. Furthermore, Γ_{div} during gas puffing is larger than that w/o gas puffing, compared at the same $\bar{n}_e$ and the NB heating power. The recycling coefficient R_{div} defined by Eq. (2.1.12) is shown in Fig. 2.3.4 (d). At the phase w/o gas puffing, R_{div} is high and ~ 1. When the gas puffing is applied, R_{div} decreases and this characteristic is more evident at the low-density regime. The recycling flux defined by (R_{div} Γ_{div}) also increases with $\bar{n}_e$, as Γ_{div}. It is convenient to use the recycling flux normalized by N_e, i.e. (R_{div} Γ_{div}) / N_e, to discuss the level of recycling flux as shown in Fig. 2.3.4 (e). It should be noted that the normalized recycling flux is increased by gas puffing, although R_{div} itself decreases.

Returning to the effective fueling efficiency, α_{eff}, it also shows the $\bar{n}_e$ dependence as shown in Fig. 2.3.5 (a). However, the correlation between these two is not simple, i.e. it is positive for the 7 MW data, and negative for the 6 MW data. The simpler correlation is obtained in Fig. 2.3.5 (b), where the abscissa is given by the normalized recycling flux. In the discharges with 6 MW NB port-through powers, the normalized recycling flux is larger than the 7 MW case, as shown in Fig. 2.3.4 (e), and at the same time it achieves a higher α_{eff}. Even for the individual datasets of 7 MW and 6 MW, respectively, a positive correlation between α_{eff} and the normalized recycling flux is recognized.

From these observations, it can be understood that high α_{eff} is resulted from the large normalized recycling flux. Therefore, it is expected that α_{eff} saturates to α_{puff} of 12 % as obtained in section 2.2, at the limit of the small normalized recycling flux. This can be seen in Fig. 2.3.5 (b), where α_{eff} ranges from 9 – 14 % in the regime of (R_{div} Γ_{div}) / N_e < 120 s^{-1}.

2.3.6. Helium gas puff experiments

Helium gas puff experiment has been carried out to change the recycling parameters. As has been often observed, decay in the plasma density is more moderate in the helium discharges compared with the hydrogen discharges. This is thought to be a resultant from the difference in the recycling property. In the helium gas puff discharges, a high α_{eff} that approaches 100 % has been obtained (Fig. 2.3.3). According to the result of the former subsection, a large recycling flux that results in the high α_{eff} is expected in these cases. Waveforms in a typical helium gas puff discharge are shown in Fig. 2.3.6. One short helium gas puff pulse of 0.15 s rapidly increases $\bar{n}_e$ from 1×10^{19} m^{-3} to 6×10^{19} m^{-3} (Fig. 2.3.6 (a)). Such a rapid density increase by gas puffing often causes the radiation collapse [10], since the excess of the neutral gas cools the plasma edge temperature and enhance the radiation loss. In this case, plasma performance is not deteriorated by gas puffing, as shown in Fig. 2.3.6 (b). Although the electron temperature decreases as the density increases during the gas puffing, the plasma-stored energy estimated from diamagnetic signals (W_{p_dia}) continues to increase and no signs of radiation collapse can be recognized. The recycling coefficient defined by Eq. (2.3.8) decreases from 1 to 0.7 at the beginning of gas puff pulse (Fig. 2.3.6 (c)), as is the hydrogen case shown in Fig. 2.3.4 (d). During the gas puffing, R_{div} increases to more than 0.95. Immediately after the gas puffing is turned off, R_{div} recovers to 1 with a slight overshoot. In Fig. 2.3.6 (d), depicted are the α_{eff} and the normalized recycling flux, (R_{div} Γ_{div}) / N_e. Although the positive correlation between these two can be seen at the early phase of gas puffing, it becomes a negative correlation at the latter phase.

The relation between α_{eff} and (R_{div} Γ_{div}) / N_e is depicted in Fig. 2.3.7 (a), where the data of hydrogen gas puffing plotted in Fig. 2.3.5 (b) are also shown for comparison. The data from the early phase of the helium gas puff pulse shows a positive correlation similar to the hydrogen case. However, even after the normalized recycling flux reaches its maximum and begins to decrease, α_{eff} continues to increase. In that phase, the positive correlation between α_{eff} and (R_{div} Γ_{div}) / N_e is completely lost. This phenomenon can be explained by Fig. 2.3.7 (b), where α_{eff} as a function of R_{div} is plotted. According to Eq. (2.3.7), one can achieve $\alpha_{eff} \sim 1$ when $R_{div} \sim 1$ and Φ_{NB} is negligible. At the phase where the positive correlation between α_{eff} and (R_{div} Γ_{div}) / N_e is lost, R_{div} is fairly large (> 0.95) and continues to increase to 1. At the same time, α_{eff} also increases to 1. Therefore, the phase where the correlation between α_{eff} and (R_{div} Γ_{div}) / N_e is lost can be understood as the transient phase to the perfect-recycling

state of $R_{div} = 1$.

2.3.7. Discussion

It has been shown that the larger effective fueling efficiency than ~ 10 % is caused by the large recycling flux. From this, the difference between Phase I and II, which were defined in section 2.2, can be explained, i.e. the recycling flux is large in the Phase I and becomes small enough in the Phase II.

An inserted piezo-valve has been used in this study. Location of the valve is identical to that in the future supersonic gas puff experiment, where the piezo-valve will be replaced to the supersonic valve. The gas flux puffed from the inserted piezo-valve directly reaches the plasma surface. Therefore, this can be called as the 'direct' gas puff. Usually, other piezo-valves set on the manifolds under the lower ports have been used in LHD, as in section 2.2. In this case, the gas flux suffers from reflection and absorption by materials like the vacuum vessel wall. However, any clear difference has not been recognized between the direct gas puffing and the ordinary 'indirect' gas puffing, in the global point of view, such as the particle balance and the fueling efficiency. Namely, the fueling efficiency of the direct gas puffing is similar to that of the ordinary gas puffing in the low recycling flux condition. Note that this result does not mean that these two are fully identical. For instance, the decay time of dN_e/dt after the gas puff termination is shorter in the direct gas puffing as shown in Fig. 2.3.8. Anyhow, the experimental results obtained here are to be compared with the future supersonic gas puff experiment. If the fueling efficiency improves after the replacement of piezo-valve to the supersonic one, it will be possible to clearly assert the merit of supersonic gas puffing.

It is not straightforward to understand the decrease in the recycling coefficient during gas puff phase. The experimental data shown in this study indicate that even the plasma facing materials seem to be saturated to give the recycling coefficient of 1, a new particle sink appears due to the gas puffing. A similar phenomenon also has been reported from the ultra-long discharge experiments on the TRIAM-1M tokamak [11]. The new sink generated by gas puffing, of course, becomes saturated, as shown in the helium gas puff discharge in Figs. 2.3.6 and 2.3.7. From the standpoint of the density control in the steady-state fusion plasmas, it is important to establish the fueling and pumping methods that are effective under the high-recycling condition. The experimental condition, where the recycling coefficient is 1 even with gas puffing, is likely be achieved in the helium gas puff discharge in LHD. Using

this, one can simulate the perfect-recycling plasmas where the wall pumping is no longer effective.

References

[1] J. Miyazawa et al., J. Nucl. Mater. **313-316**, 534 (2003).

[2] H. Suzuki et al., J. Nucl. Mater. **313 - 316**, 297 (2003).

[3] S. Masuzaki et al., Nucl. Fusion **42**, 750 (2002).

[4] K. Tanaka et al., Rev. Sci. Instrum. **72**, 1089 (2001).

[5] K. Narihara et al., Phys. Rev. Lett. **87**, 135002 (2001).

[6] S. Morita et al., Nucl. Fusion **42**, 1179 (2002).

[7] M. Osakabe et al., Rev. Sci. Instrum. **72**, 590 (2001).

[8] H.F. Dylla et al., J. Nucl. Mater. **111&112**, 211 (1982).

[9] K. Yamada et al., Nucl. Fusion **27**, 1203 (1987).

[10] Y. Xu et al., Nucl. Fusion **42**, 601 (2002).

[11] M. Sakamoto et al., J. Nucl. Mater. **313 - 316**, 522 (2003).

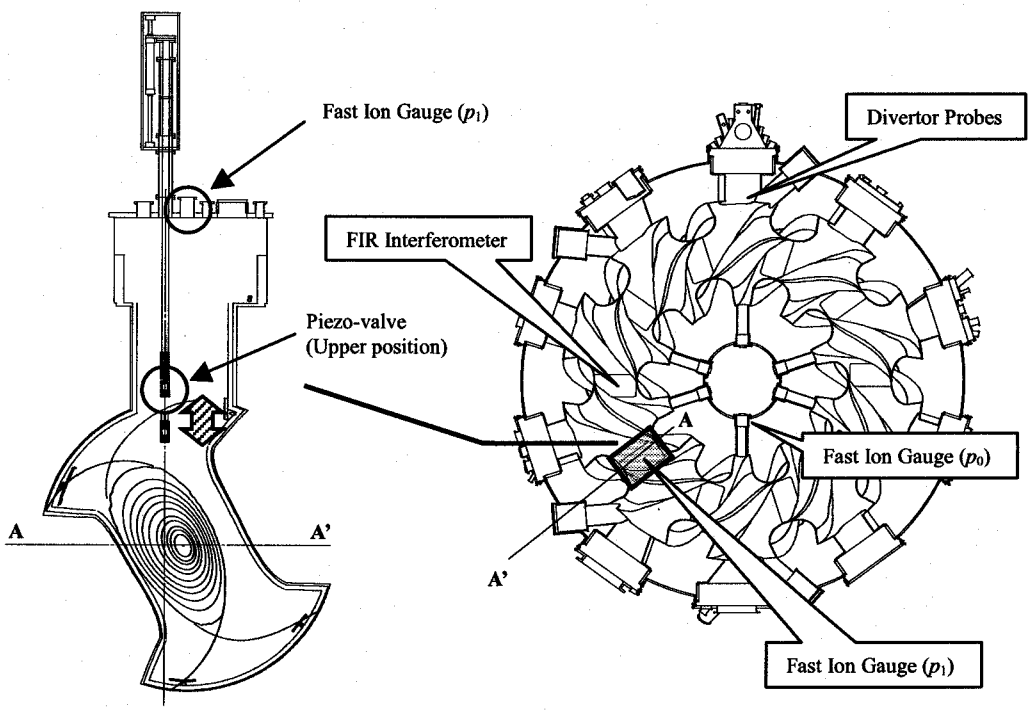

Fig. 2.3.1. Schematic view of the inserted piezo-valve and its location in LHD. Toroidal positions of typical measurements are also shown.

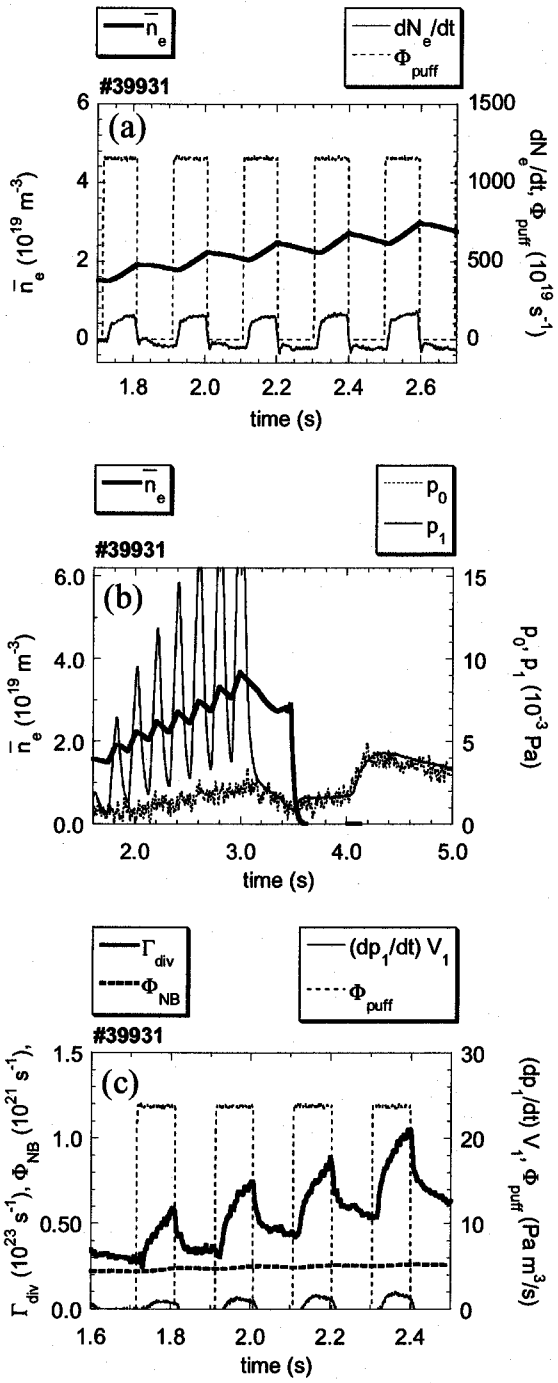

Fig. 2.3.2. Typical waveforms of the hydrogen gas puff discharge (#39931), where R_{ax} = 3.5 m, B_0 = 2.854 T, and NB port-through power is 7 MW. (a) Time evolutions of $\bar{n}_e$, dN_e/dt and Φ_{puff}. (b) Time evolutions of $\bar{n}_e$, and the neutral particle pressure measured at different toroidal position (p_0 and p_1). (c) Comparison between Γ_{div}, Φ_{NB}, the neutral particle flux estimated from the time derivative of p_1, and Φ_{puff}. Note that the unit of Γ_{div} (10^{23} s^{-1}) is a hundred times larger than that of Φ_{NB} (10^{21} s^{-1}).

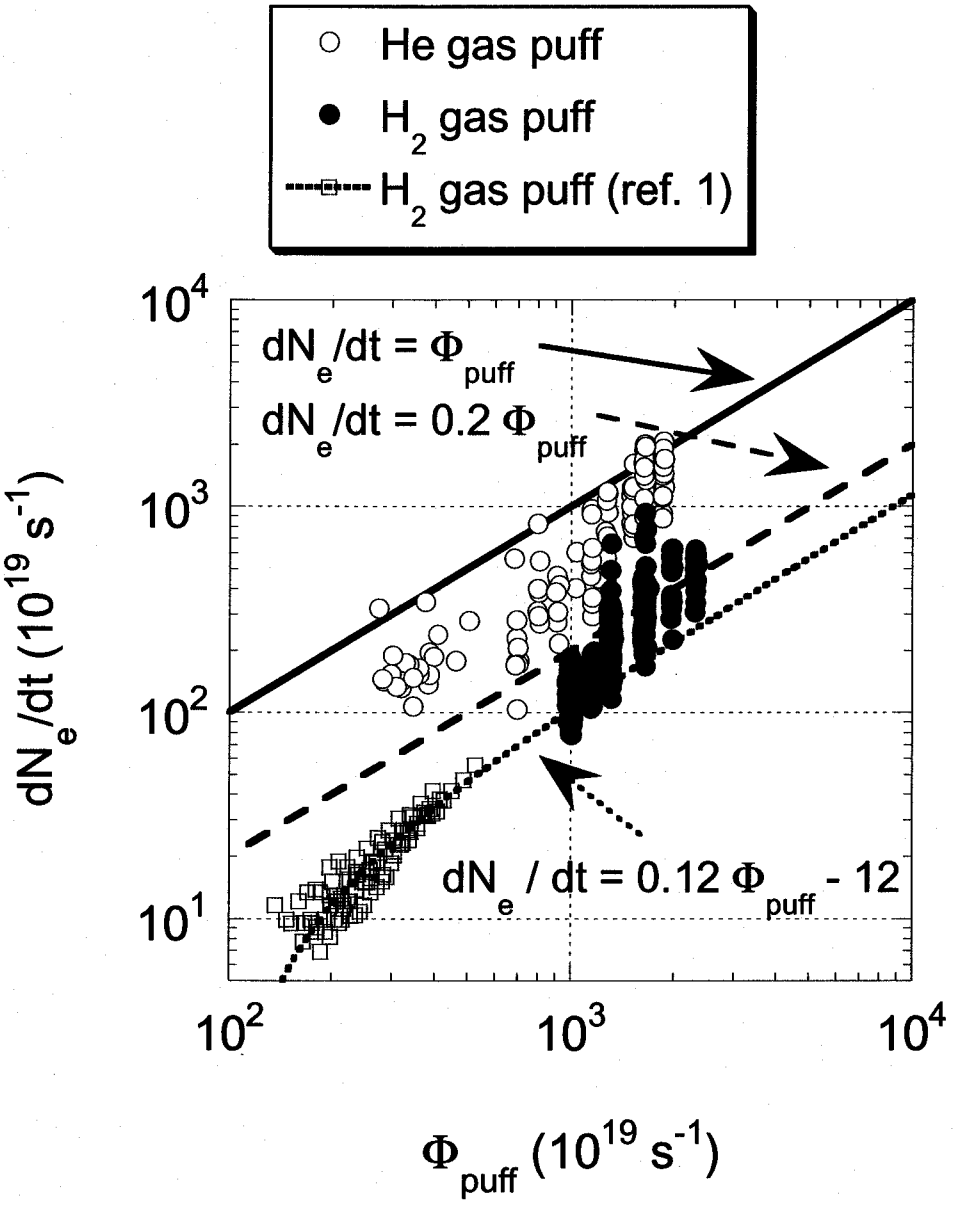

Fig. 2.3.3. Comparison between Φ_{puff} and dN_e/dt. The open circles and the closed circles are the data from the helium and the hydrogen gas puff discharges, respectively. The open squares are the data plotted in Fig. 2.2.3 in section 2.2 (denoted as 'ref. 1').

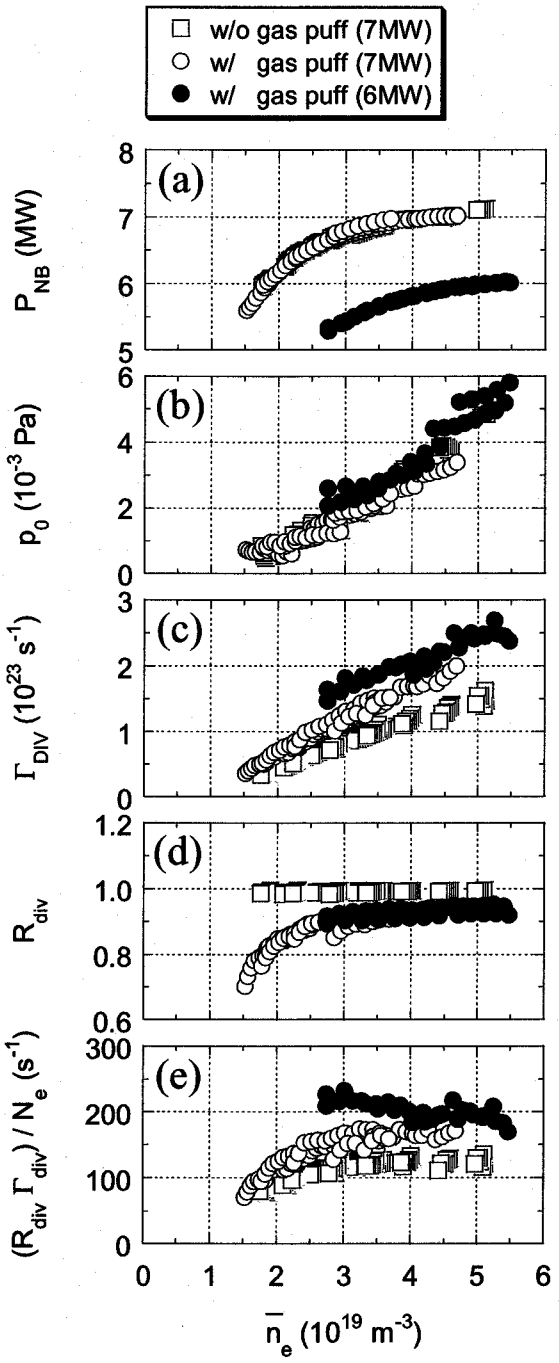

Fig. 2.3.4. Density dependence of (a) P_{NB}, (b) p_0, (c) Γ_{div}, (d) R_{div}, and (e) the normalized recycling flux, $(R_{div}\,\Gamma_{div})$ / N_e. Open squares are the data between the gas puff pulses (denoted as 'w/o gas puff'), where the NB port-through power is fixed to 7 MW. Open circles and closed circles are the data during gas puffing, where the NB port-through power is fixed to 7 MW and 6 MW, respectively.

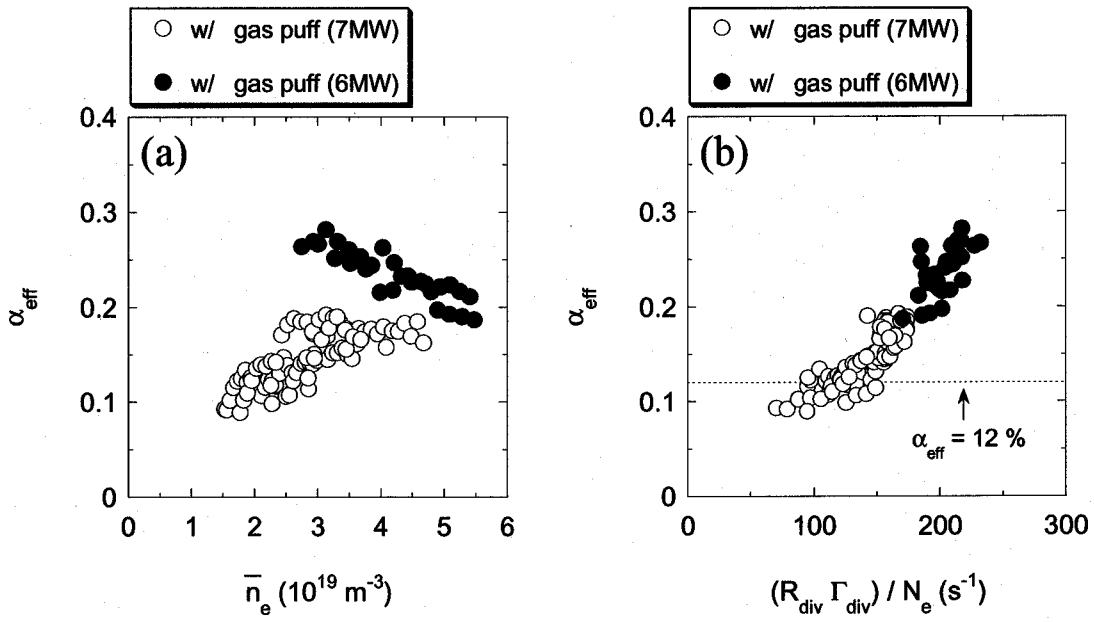

Fig. 2.3.5. The effective fueling efficiency, α_{eff}, as a function of (a) $\bar{n}_e$ or (b) the normalized recycling flux, $(R_{div}\,\Gamma_{div}) / N_e$.

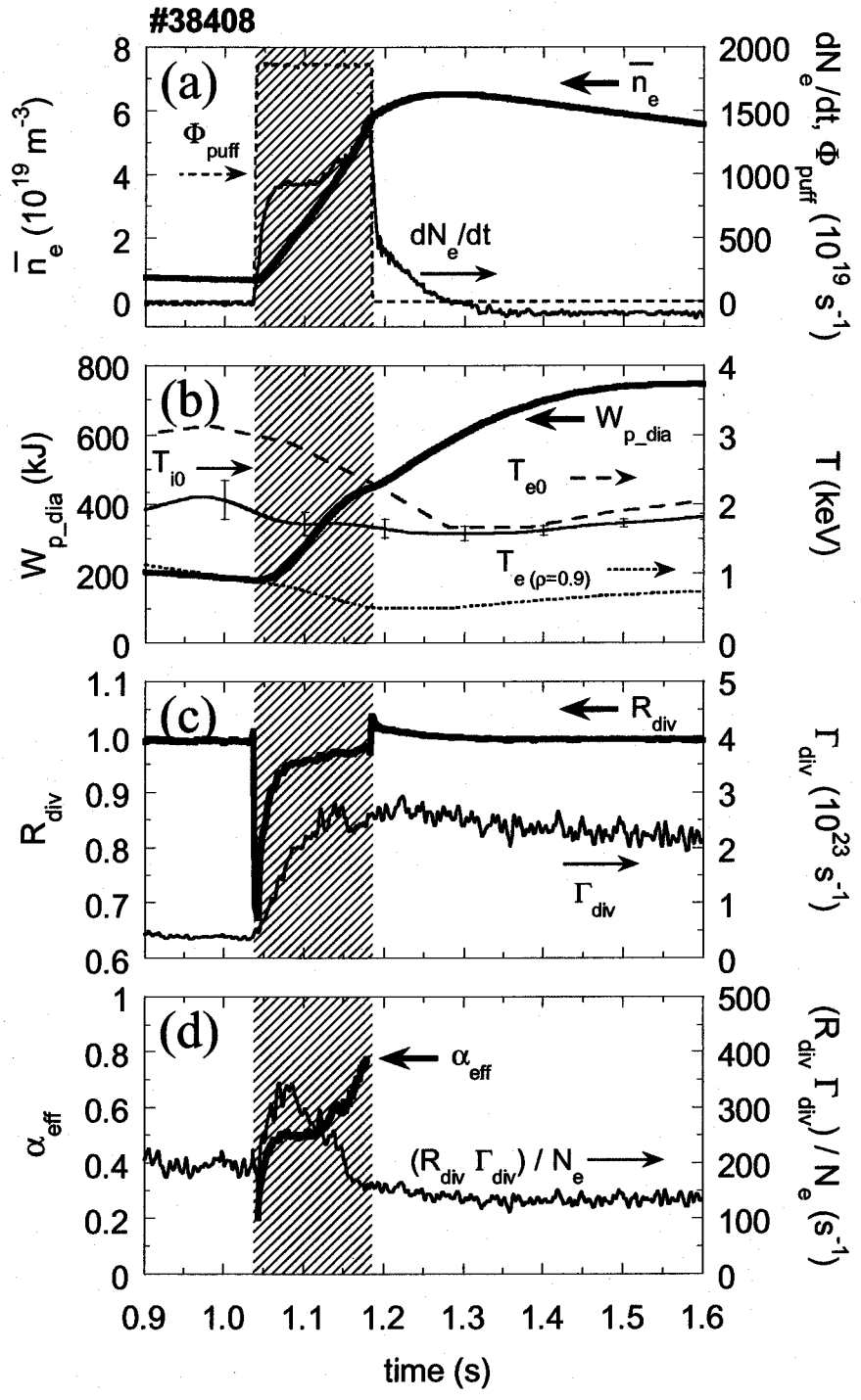

Fig. 2.3.6. Time evolutions of typical parameters in the helium gas puff discharge, where R_{ax} = 3.6 m, B_0 = 2.8 T, and the NB port-through power is 6.5 MW. Hatched region denotes the gas puff phase.

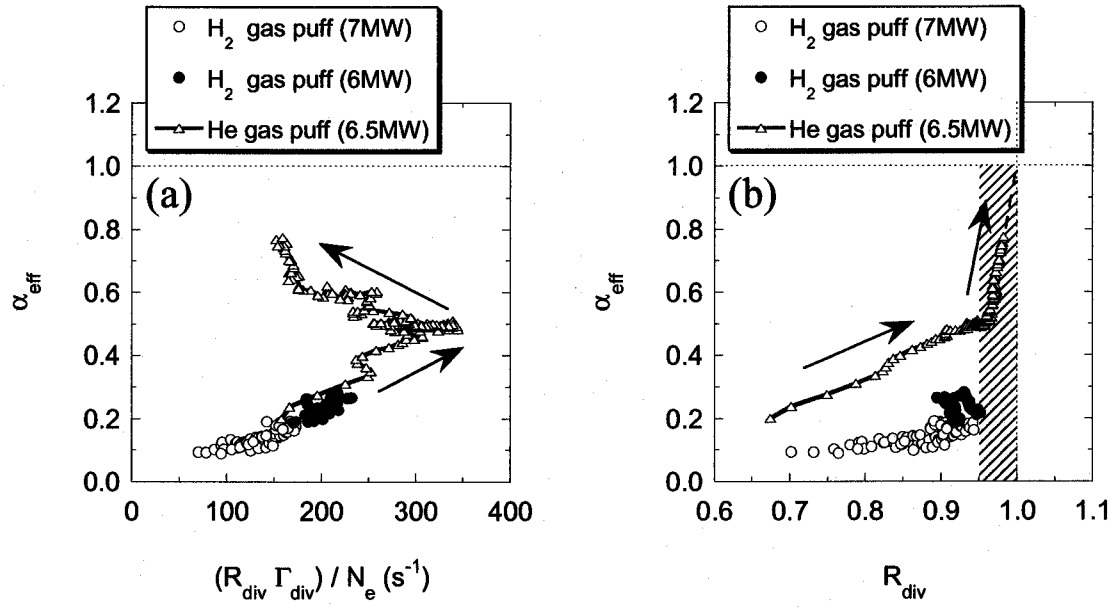

Fig. 2.3.7. The effective fueling efficiency α_{eff} as a function of (a) the normalized recycling flux, (R_{div} Γ_{div}) / N_{e} or (b) the recycling coefficient R_{div}. Open and closed circles are the same data as shown in Fig. 2.3.5. Open triangles denote the helium gas puff data from the hatched region in Fig. 2.3.6 (#38408). Arrows indicate the direction of the time evolution in #38408.

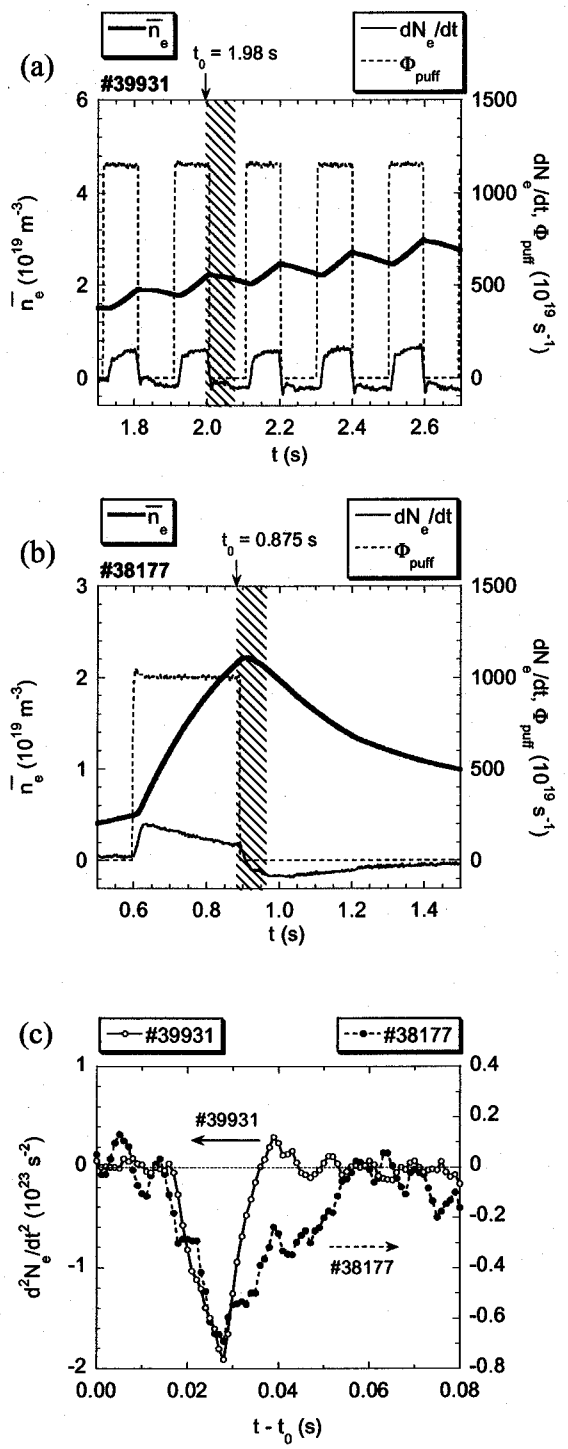

Fig. 2.3.8. Typical waveforms of (a) the direct gas puff discharge (#39931), where R_{ax} = 3.5 m, B_0 = 2.854 T, and NB port-through power is 7 MW, (b) the ordinary gas puff discharge (#38177), where R_{ax} = 3.6 m, B_0 = 2.893 T, and NB port-through power is 5 MW. (c) d^2N_e/dt^2 in #39931 and #38177 plotted with the offset time axis, $t - t_0$, where t_0 = 1.98 s for #39931 and t_0 = 0.875 s for #38177. Hatched regions in (a) and (b) correspond to the time window shown in (c).

2.4. Summary

The fueling efficiency of the hydrogen gas puffing has been estimated for the NB heated plasmas in LHD. A particle balance model was introduced together with the criteria to examine the applicability of the model. Five discharges were chosen from the series of density ramp up experiment, to apply the model. The latter phase of the discharges satisfied the criteria, whereas the ramp up phase was not adequate to estimate the fueling efficiency. The fueling efficiency of 0.12 has been obtained from the data ensemble at the latter phase of the five discharges. It was also suggested that this fueling efficiency of about 10 % is not sensitive to the NB heating power or the existence of the magnetic island.

The gas puff experiments using the piezo-valve inserted inside the LHD have been carried out. High effective fueling efficiency of up to 50 % was obtained in the hydrogen gas puff discharges. From the pressure rise localized around the gas puff port, the ionization efficiency was estimated as more than 90 %. The recycling coefficient and the recycling flux were also estimated. The recycling coefficient decreases during the gas puff phase, while it is about 1 in the phase w/o gas puffing. On the other hand, the recycling flux increases during the gas puff phase. It was shown that the high effective fueling efficiency obtained in the hydrogen gas puff discharges could be explained by the enhancement of the recycling flux normalized by the electron density. At the low recycling flux regime, the effective fueling efficiency decreases to ~ 10 %.

In the helium gas puff discharges, the effective fueling efficiency is higher than the hydrogen cases. The effective fueling efficiency increases with the normalized recycling flux in the early phase of gas puff pulse. At the regime where the recycling coefficient is larger than 0.95, the effective fueling efficiency begins to increase to 1, being irrelevant to the recycling flux. This is what expected from the total particle balance. Namely, if there is no particle sink and the perfect recycling condition is achieved, the plasma density increases exactly with the particle influx.

As has been shown, gas puffing has a strong influence on the plasma edge parameters and especially affects the recycling phenomena. On the other hand, however, the direct fueling into the plasma core is not achievable by the gas puffing. Therefore, other fueling method that can realize the center fueling is needed. In tokamaks, ice-pellet injection from the high-field side is a likely candidate. In helical plasmas, however, the magnetic field strength has a three-dimensional profile and the same scenario cannot be simply realized. One of the possible scenarios is the compact toroid (CT) injection, where a dense magnetized

plasmoid is electro-magnetically accelerated to several hundreds of km/s and injected to the target plasmas. Reserch and development of the CT injector for LHD is also a theme of this thesis and described in chapter 4.

Although gas puffing is not capable of the center fueling, it is still a powerful method for investigation of the plasma physics and even has a possibility to trigger the confinement improvement. Making use of the flexibility of gas puffing that the working gas can be changed from hydrogen to others, such as helium, methane, and neon, we have performed many experiments in LHD. Example of the helium gas puff discharge, where higher recycling coefficient compared with hydrogen cases is obtained, was already shown in this chapter. In the next chapter, other results from methane or neon gas puff experiments will be presented. These are the good examples that show the flexibility and the importance of gas puffing in the plasma experiments.

Chapter 3 Exploration for the Confinement Improvement by High-Z Gas Puffing

One of the merits of gas puffing is the flexibility in the selection of the working gas. High-Z (often called as "impurity") gas puffing has been utilized to change the plasma property. In tokamaks, a number of impurity induced confinement improvement has been reported, i.e. Z-mode in ISX-B, RI-mode in TEXTOR-94, TFTR, and DIII-D, where a small amount of noble gas was injected to the hydrogen or deuterium plasmas. On the other hand, the confinement property of LHD plasmas shows the gyro-Bohm nature, where the energy confinement time inversely depends on the ion gyro-radius (see Appendix). In this chapter, two examples of the exploration for the plasma confinement improvement by impurity gas puffing are discussed. Favorable aftereffects, such as the metal impurity reduction and the confinement improvement, caused by the methane gas puff discharges are presented in section 3.1. The global electron energy confinement in the neon gas puff discharges is analyzed in section 3.2.

3.1. Favorable aftereffects of the methane discharge observed in LHD pellet shot

The methane mixed hydrogen gas puff experiment has been carried out on LHD, to test the possibility of impurity control and the feasibility of real time carbonization (RTC). Although the methane mixed discharges itself did not show clear differences compared with the hydrogen gas puff shots, only four discharges introducing ~ 20 Pa·m^3 of methane (consisting of about 5×10^{21} of carbon atoms) caused the reduction of metal impurity emission, together with the increased confinement in the shot fueled by hydrogen ice-pellets. In this chapter, the effect of methane discharges on the confinement property is investigated; especially we perform the transport analysis of pellet shots before and after methane discharges.

3.1.1. Methane gas puff experiment

Results of experiments to test the feasibility of RTC are demonstrated in Fig. 3.1.1, where the

maximum plasma stored energy, $(W_p)_{max}$, which is derived from diamagnetic signals, the level of CIII emission, the radiation loss, P_{rad}, and the ratio of τ_E^{EXP} to τ_E^{ISS95}, F_{ISS95} (= $\tau_E^{EXP}/\tau_E^{ISS95}$; τ_E^{EXP} is the experimental energy confinement time, and τ_E^{ISS95} is what expected from the international stellarator scaling 95 (ISS95) [1]) are shown from top to bottom. The abscissa is a line-averaged electron density, $\bar{n}_e$. These discharges were carried out continuously in a day with typical experimental parameters fixed; i.e. the magnetic field strength on magnetic axis, $B_0 \sim 2.85$ T, the major radius of magnetic axis, $R_{ax} = 3.6$ m, and the averaged minor radius of plasma, $a \sim 0.6$ m. All of the data points are extracted from neutral beam (NB) heated discharges of 3.6 – 4.5 MW total heating power, P_{NB}. Here, P_{NB} is estimated from the NB port-through power and the direct heat-load measurement of NB shine-through power [2], which shows sufficient agreement with the three-dimensional Monte Carlo simulation [3] in the dense plasmas of $\bar{n}_e > 2 \times 10^{19}\,m^{-3}$. Typical LHD plasma shows a favorable dependence of $W_p \propto \bar{n}_e^{0.51}$, as predicted by ISS95 scaling [1]. A deterioration of the scaling in the high-density regime ($\bar{n}_e > 5 \times 10^{19}$ m^{-3}) can bee seen in Fig. 3.1.1 (a), where F_{ISS95} also decreases (see Fig. 3.1.1 (d)). Four successive CH_4 mixed hydrogen gas puff discharges were carried out, introducing about 20 Pa·m^3 of CH_4 in total. Data from two of the four CH_4 discharges are also depicted by open triangles in Fig. 3.1.1, which has slightly improved F_{ISS95} compared with that before the CH_4 discharges. In the meanwhile, significant differences are observed between the pellet shots before and after CH_4 discharges, where $(W_p)_{max}$, the emission of CIII, and F_{ISS95} systematically increase, and P_{rad} for higher density decreases after CH_4 discharges. Hereinafter, we focus on the differences in the pellet shots before and after the methane discharges.

3.1.2. Phenomenological differences

Two typical pellet shots before and after CH_4 discharges are compared in Fig. 3.1.2. At the time $t = t_0 = 1.1$ s in the both discharges, W_p, $\bar{n}_e$, P_{NB}, and the electron temperature T_e are almost the same. However, the decay time of $\bar{n}_e$ in the pellet shot after CH_4 discharges (#23114) is mitigated to about twice of that before CH_4 discharges (#23046). This directly results in the larger W_p for $t > t_0$, since the temporal behaviors of T_e are almost the same. Here we compare the time slice of #23046 at $t = t_1 = 1.25$ s and that of #23114 at $t = t_1' = 1.4$ s, to keep $\bar{n}_e$ in both slices the same. In these time slices, the energy confinement time and F_{ISS95}

in #23114 are larger than that in #23046, since P_{NB}, dW_p/dt (~ 0) and $\bar{n}_e$ are identical. As shown in Fig. 3.1.2 (b) and (c), the total radiation loss P_{rad} and the emission of FeXVI become smaller after CH_4 discharges. This suggests the reduction of metal impurity, which is expected as the real time carbonization (RTC) effect. Metal impurity reduction is also seen in the soft X-ray spectra as shown in Fig. 3.1.3, where the K_α lines of Ti, Cr, and Fe are significantly reduced in #23114.

To see the difference between these two shots more precisely, radial profiles of the electron density, $n_e(\rho)$, the electron temperature, $T_e(\rho)$, and the radiation loss power density, $p_{rad}(\rho)$, are compared in Fig. 3.1.4 ($\rho = r/a$ is the normalized minor radius). The radial profiles at $t = t_0$ and $t = t_1$ of #23046 and those at $t = t_0$ and $t = t_1$' of #23114 are chosen to compare the change in T_e and p_{rad} profiles, while keeping the similar n_e profile. As seen in Fig. 3.1.4 (a), n_e profile of #23114 has a hump at the plasma boundary of $\rho > 0.8$, indicating relatively enhanced recycling after CH_4 discharges. There also are other indications of the enhanced recycling in the divertor flux and the neutral pressure, i.e. both of them increased significantly after CH_4 discharges. However, the n_e profiles inside the plasma ($\rho < 0.7$) are almost identical. This suggests that the particle source from the enhanced recycling is negligible in the core region. As for the T_e profiles (Fig. 3.1.4 (b)), there is a significant difference between #23046 ($t = t_1$) and #23114 ($t = t_1$'). After CH_4 discharges, the central electron temperature increases up to 120% of that before CH_4 discharges. Metal impurity reduction is recognized again in the p_{rad} profiles shown in Fig. 3.1.4 (c), where the hump observed at $\rho \sim 0.6$ in #23046 disappears in #23114.

3.1.3. Particle transport analysis

Particle transport analysis is carried out using the n_e profile such as shown in Fig. 3.1.4 (a). Here, the particle diffusion coefficient, D, and the convection velocity, V, are directly estimated from the temporal behavior of n_e profile [4]. The particle balance equation is given as below;

$$\frac{\partial n_e}{\partial t} = -\nabla \cdot \Gamma + S = -\frac{1}{r}\frac{\partial}{\partial r} r\Gamma + S, \qquad (3.1.1)$$

where S is the particle source rate, Γ is the particle flux defined by;

$$\Gamma = -D\frac{\partial n_e}{\partial r} + Vn_e. \tag{3.1.2}$$

Integrating Eq. (3.1.1) with r, $\Gamma(r)$ is expressed as;

$$\Gamma(r) = \frac{1}{r}\int_0^r r\left(S - \frac{\partial n_e}{\partial t}\right)dr. \tag{3.1.3}$$

It is straightforward from Eq. (3.1.2) that a linear regression $y = Ax + B$ of a scatter plot with $x = (dn_e/dr) / n_e$ and $y = \Gamma / n_e$ at a fixed position ρ gives $D(\rho)$ as -A and $V(\rho)$ as B. An example of the scatter plot is shown in Fig. 3.1.5. Using this method, the radial profiles of D (Fig. 3.1.6 (a)) and V (Fig. 3.1.6 (b)) are obtained. Number of time points used for the fitting is 16 (31) for #23046 (#23114). Note that the analysis is carried out in the region of $\rho = 0.25 - 0.65$ assuming $S = 0$. Since the particle source from the recycling is localized in the plasma edge ($\rho > 0.65$), and the particle source from NBI is less than 10^{19} $m^{-3}s^{-1}$ while the typical order of $-dn_e/dt$ in this region is around 10^{20} $m^{-3}s^{-1}$, the assumption of $S = 0$ is acceptable. It can be concluded from Figs. 3.1.6 (a) and (b) that the value of D is reduced to 35 – 45 % after CH_4 discharges, while V is almost unchanged and nearly zero in the core region of $\rho < 0.5$.

3.1.4. Thermal transport analysis

The effective thermal transport coefficient, χ_{eff}, is directly derived from the energy balance equation;

$$3\frac{\partial(nT)}{\partial t} = \frac{1}{r}\frac{\partial}{\partial r}r\left(2n\chi_{eff}\frac{\partial T}{\partial r} - 5T\Gamma\right) - p_{rad} + p_{NB}, \tag{3.1.4}$$

where p_{rad} and p_{NB} are the radiation loss power density and the total heating power density of NBI, respectively. Note that we assumed $n = n_e = n_i$, $T = T_e = T_i$, and $\Gamma = \Gamma_e = \Gamma_i$. Using profiles at $t = 1.2 - 1.25$ s of #23046 and that at $t = 1.3 - 1.4$ s of #23114, χ_{eff} profiles are estimated and shown in Fig. 3.1.6 (c). Here the particle flux Γ is calculated using the result obtained in the former subsection, and p_{NB} is calculated by the three-dimensional Monte Carlo simulation [3]. In Fig. 3.1.6 (c), thin solid and broken lines denote the χ_{eff} estimated without the convection term of $-5T\Gamma$. Even taking into account the large contribution of the convection term in #23046, the χ_{eff} is still smaller in #23114. Although the profile of p_{rad}

significantly differs in these two shots as seen in Fig. 3.1.4, this is not influential because p_{NB} is about ten times larger than p_{rad}. The difference of χ_{eff} between the two shots mainly comes from the large difference in $n\mathrm{d}T/\mathrm{d}r$ profile.

References

[1] U. Stroth et al., Nucl. Fusion **36**, 1063 (1996).

[2] M. Osakabe et al., Rev. Sci. Instrum. **72**, 590 (2001).

[3] S. Murakami, N. Nakajima, and M. Okamoto, Trans. Fusion Technol. **27**, 256 (1995).

[4] K. Tanaka et al., in Proceedings of the 26th EPS Conference on Controlled Fusion and Plasma Physics, Maastricht, ECA Vol. 23J, 1329 (1999).

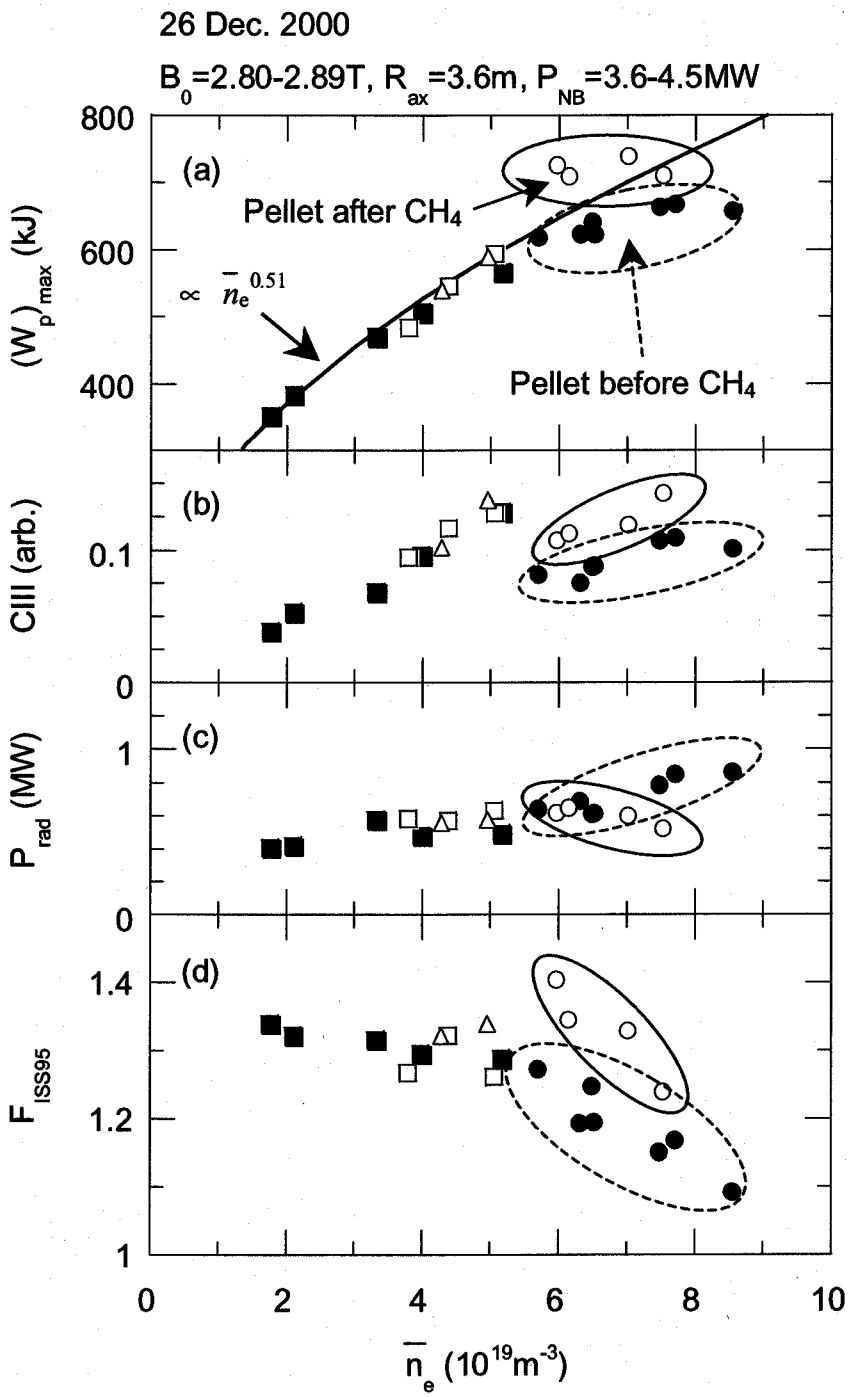

Fig. 3.1.1. Typical plasma parameters in relation to the line-averaged electron density, $\bar{n}_e$. Here, (a) $(W_p)_{max}$, (b) the intensity of CIII emission, (c) P_{rad}, and (d) F_{ISS95} are shown from top to bottom. Solid and open circles (rectangles) denote pellet (gas puff) shots before and after CH_4 mixed hydrogen gas puff discharges (open triangles), respectively.

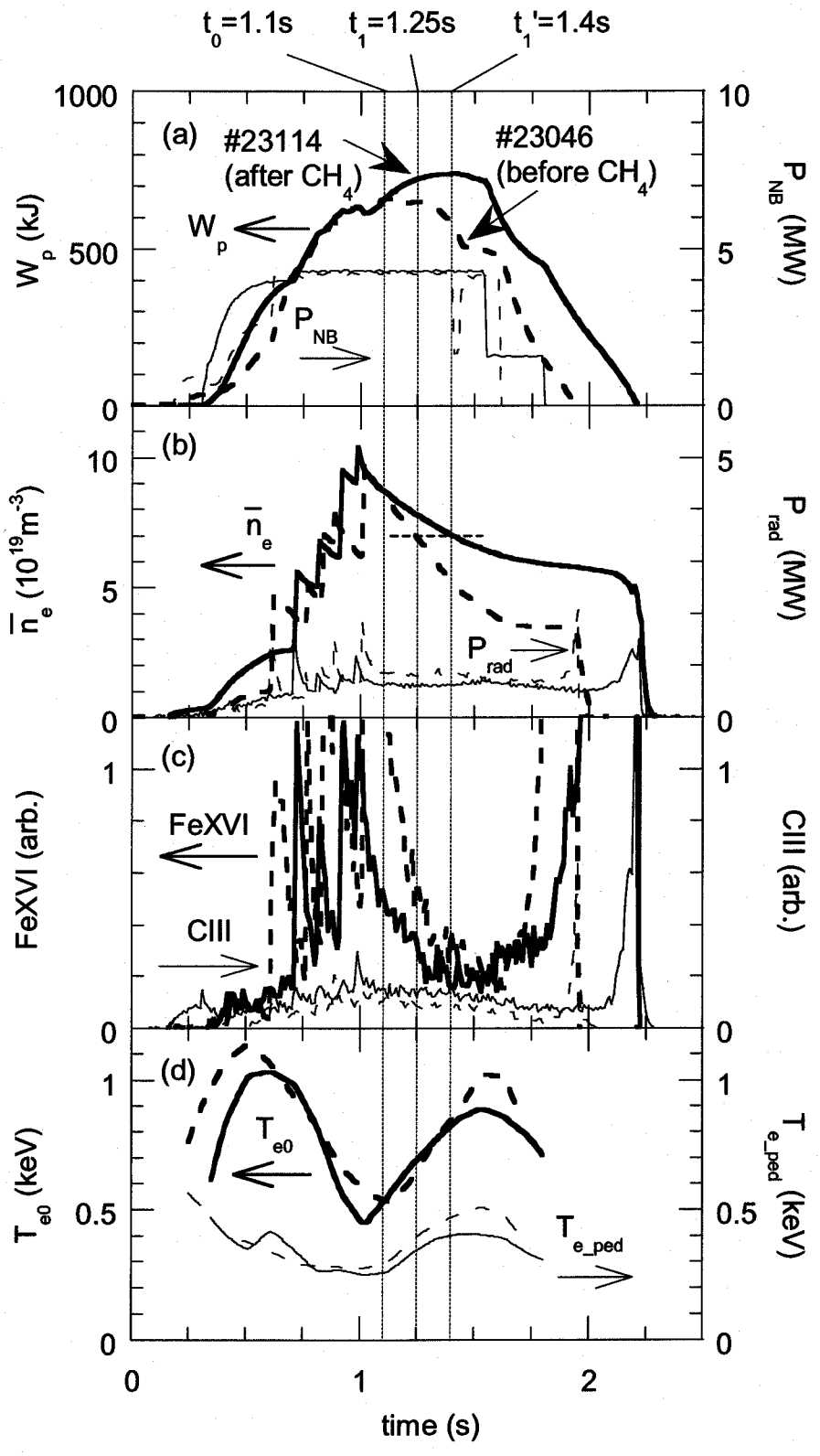

Fig. 3.1.2. Waveforms of (a) W_p and P_{NB}, (b) $\bar{n}_e$ and P_{rad}, (c) the emission intensities of FeXVI and CIII, (d) the electron temperature at the plasma center, T_{e0}, and the pedestal (ρ = 0.9), T_{e_ped}. Broken and solid lines denote #23046 (before CH_4 discharges) and #23114 (after CH_4 discharges). Times t_1 and t_1' are chosen so that values of $\bar{n}_e$ are similar.

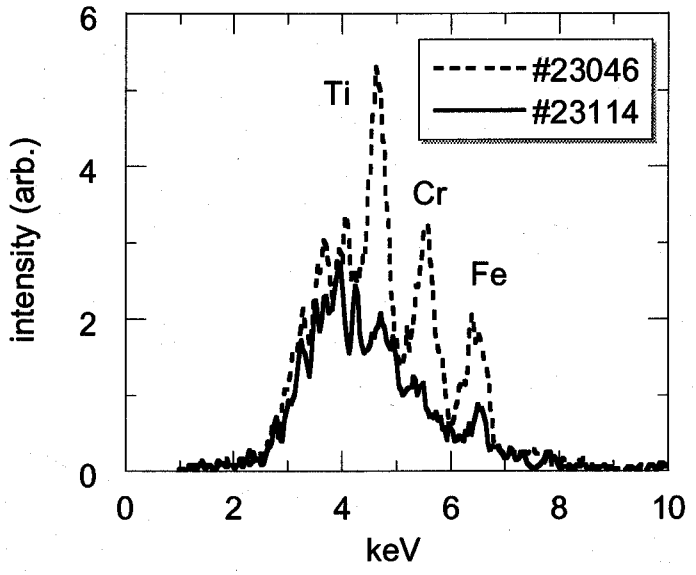

Fig. 3.1.3. Integrated soft X-ray spectra before (#23406) and after (#23114) CH_4 discharges. Each of spectra is integrated from t = 1.2 s to t = 1.5 s. The K_α lines of Ti (4.5 keV), Cr (5.4 keV), and Fe (6.4 keV) are included in the spectra.

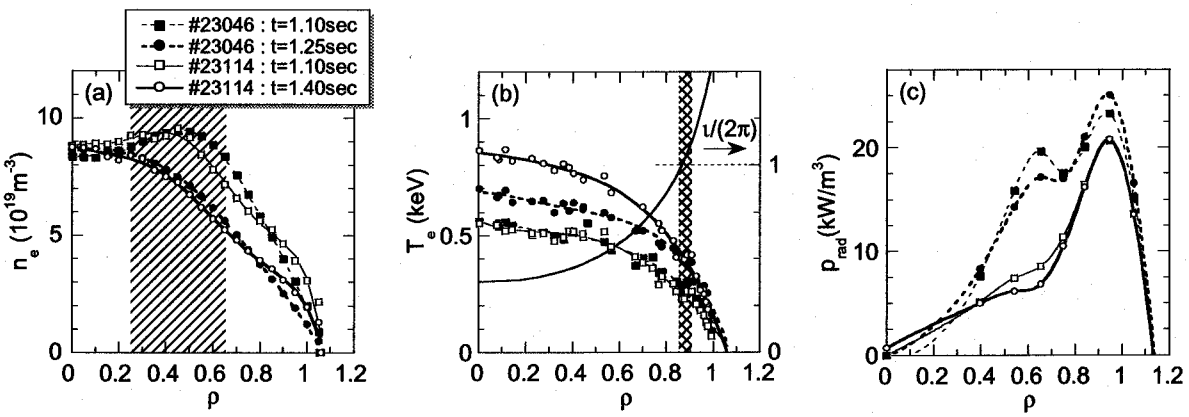

Fig. 3.1.4. Radial profiles of (a) n_e, (b) T_e and the rotational transform, ι, and (c) p_{rad}. Hatched region in (a) is where the particle transport analysis is carried out, and that in (b) indicates the position of the magnetic island at $\iota \sim 1$.

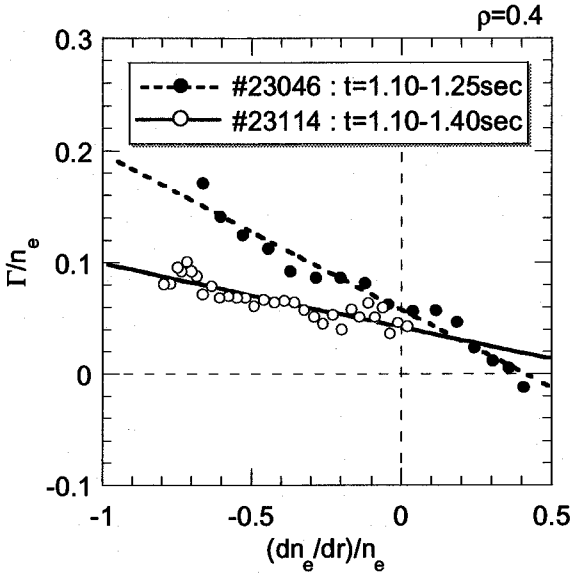

Fig. 3.1.5. Scatter plot of $(dn_e/dr) / n_e$ vs Γ / n_e at $\rho = 0.4$.

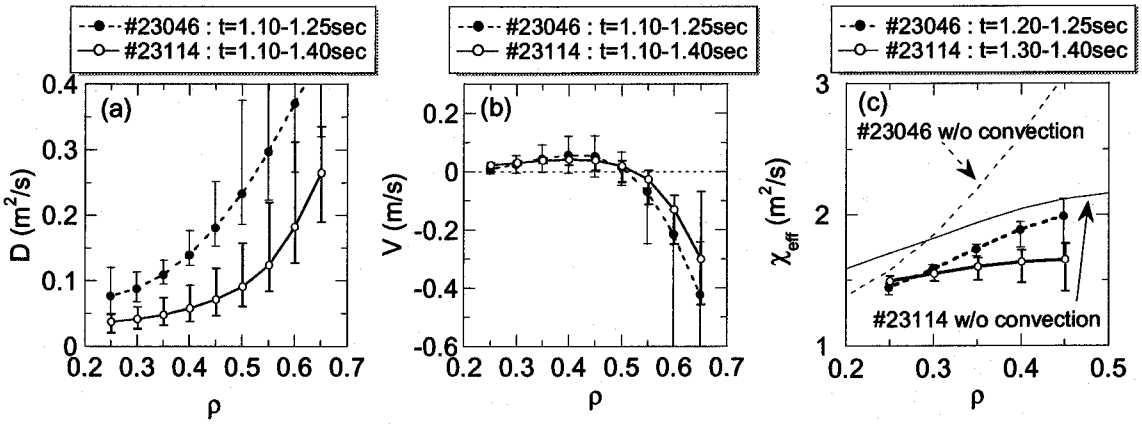

Fig. 3.1.6. Radial profiles of (a) D, (b) V, and (c) χ_{eff}. Radial profiles of broken and solid lines denote #23046 (before CH_4 discharges) and #23114 (after CH_4 discharges), respectively. Error-bars in (a) and (b) denote the upper and lower limits of estimation resulting from the error in the Abel inversion of n_e profile. Error-bars in (c) are calculated from that of D. Thin broken (solid) line in (c) is the estimation of χ_{eff} without considering the convection term in # 23046 (#23114).

3.2. Global electron energy confinement of neon plasmas

Neon gas puff experiment has been performed on LHD, to investigate the effect of electric charge and mass of plasma ions on the energy confinement property. Here, we focus on the global energy confinement of electrons in the plasmas heated by the neutral beam (NB) injection. The major radius of the magnetic axis, R, and the plasma minor radius, a, are fixed to 3.6 m and 0.62 m, respectively. Meanwhile, the magnetic field strength at the plasma center, B_0, is changed from 1.5 T to 2.893 T.

3.2.1. Neon gas puff experiment

Comparison between the neon discharge and the hydrogen discharge at the similar electron density is shown in Fig. 3.2.1, where the hydrogen plasma is created without gas puffing and the recycled hydrogen atoms are thought to increase the density. The NB shine-through power is reduced in the neon plasmas due to its large ionization rate between the NB particles and neon atoms, at the similar $\bar{n}_e$ (see Figs. 3.2.1 (a) and (b)). Both of the electron (T_{e0}) and the ion temperature (T_{i0}) at the plasma center are higher in the neon plasma (Figs. 3.2.1 (c) and (d)). The plasma-stored energy estimated from the diamagnetic signal, W_{p_dia}, is larger in the neon plasma, while the electron-stored energy, W_{e_kin}, estimated from the radial profiles of the electron temperature and the electron density, is identical (Fig. 3.2.1 (e)). The radiation loss power, P_{rad}, in the neon plasma is larger than that of the hydrogen plasma (Fig. 3.2.1 (f)). Furthermore, the beam driven current is larger in the neon plasma (not shown).

The favorable points in the neon plasmas are then summarized as: larger W_{p_dia}, higher T_{e0} and/or T_{i0}. However, one should note that W_{p_dia} possibly overestimates the plasma stored energy due to the high-energy beam component, especially in the low-density plasmas. To avoid this, it is necessary to estimate the ion-stored energy, W_{i_kin}, from the radial profiles of the ion temperature and the ion density, which have not measured in LHD to date. Therefore, we mainly discuss the global energy confinement of the electrons based on the W_{e_kin}, in this study. Since the electron heating by high-energy beam ions is dominant in LHD, it is especially important to understand the energy confinement of electrons.

The relation between T_{e0} (T_{i0}) and the volume averaged electron density, $\langle n_e \rangle$, is plotted in Fig. 3.2.2 (a) (Fig. 3.2.2 (b)). Only the hydrogen (or the neon) gas is puffed into plasmas denoted as 'hydrogen' (or, 'neon') plasmas. Shown in the figure are the data

extracted from the high (B_0 = 2.8 T) and the low (B_0 = 1.5 T) magnetic field experiments. The highest T_{e0} is obtained in the neon plasmas, although the difference from the hydrogen data is not remarkable. As for the T_{i0}, which is plotted in Fig. 3.2.2 (b), there is a significant difference between the hydrogen plasmas and the neon plasmas; i.e. T_{i0} of the neon plasmas is more than 1.5 times higher than that of the hydrogen plasmas, in the high B_0 case. In Fig. 3.2.2 (c), drawn is the $\langle n_e \rangle$ dependence of the electron-stored energy, W_{e_kin}, which is estimated from the profiles of $T_e(\rho)$ and $n_e(\rho)$, where $\rho = r/a$ is the normalized radius. The energy confinement time of the helical plasmas usually exhibits the positive dependence on density as summarized in the international stellarator scaling 95 (ISS95) [1]. In the experiment, the positive density dependence of W_{e_kin} can be recognized only in the low-density regime of $\langle n_e \rangle < 2 \times 10^{19}\,\mathrm{m}^{-3}$ (see Fig. 3.2.2 (c)). This 'saturation' of the global confinement in the high-density regime is not fully understood at this moment. In this study, however, our interest lies in the difference between the hydrogen plasmas and the neon plasmas. Therefore, we restrict the density range as $\langle n_e \rangle < 2 \times 10^{19}\,\mathrm{m}^{-3}$ in the analysis below, to eliminate the saturated data.

3.2.2. Electron heating power of the neutral beam

To discuss the electron- and the ion- energy confinement individually, it is necessary to estimate the electron / ion heating power of the NB. The equations below are used to estimate the ratio of the ion heating power, R_i;

$$R_i = \frac{E_{bc}}{E_{NB}} \int_0^{E_{NB}/E_{bc}} \frac{dt}{1+t^{3/2}} \qquad (t \equiv E_b/E_{bc}), \tag{3.2.1}$$

$$E_{bc} = 14.8 T_e \left(\frac{1}{n_e} \sum_i \frac{n_i Z_i^2 A_b^{3/2}}{A_i} \right)^{2/3}. \tag{3.2.2}$$

In Fig. 3.2.3, depicted is E_{NB} / E_{bc} vs R_i. Distributions of P_{NB} and P_{NB_e} are shown in Fig. 3.2.4. In LHD, negative-ion based NB injection systems are adopted and E_{NB} is much larger than T_e (typically, E_{NB} > 150 keV). This results in the large fraction of the electron heating power, P_{NB_e}, of about 0.8 P_{NB}. Here, 'pure' plasmas are assumed for both of the hydrogen (Z_{eff} = 1) and the neon (Z_{eff} = 10), to give P_{NB_e}. The errors due to this assumption will be discussed later in this subsection. As seen in Fig. 3.2.2 (a) and (b), $T_{i0} < T_{e0}$ is observed in the low-density hydrogen plasmas, and therefore the heat transfer from the electrons to the ions,

P_{ei}, which is also plotted in Fig. 3.2.4 (b), should be considered carefully. Since we have no information about the ion temperature profile to date, $T_i(\rho) = T_e(\rho) \times (T_{i0} / T_{e0})$ is assumed to estimate P_{ei} in Fig. 3.2.4 (b). The maximum P_{ei} reaches to 1 MW at $\langle n_e \rangle < 2 \times 10^{19}$ m^{-3} and is not small enough to be neglected. Hereinafter, we eliminate the data that has $P_{ei} / P_{NB} > 0.1$, and neglect P_{ei} to reduce its influence.

In this study, 'pure' plasmas are assumed for both of the hydrogen and the neon plasmas. To investigate the error in P_{NB_e} due to this assumption, we recalculate it with the impurity contamination. According to the experimental fact that the dominant impurities in LHD plasmas are the carbon and the oxygen, we assume that the impurity of $Z / A = 7 / 15$ with the density of 5×10^{17} m^{-3} is contaminating to the hydrogen plasmas (Z (A) is the charge (mass) of the impurity ions). As for the neon plasmas, 0.7 $\langle n_e \rangle$ of hydrogen atoms are considered as the impurity and therefore Z_{eff} is fixed to 3.7. Under these assumptions, the power dependence of the collisionality ν^* in the hydrogen and the neon plasmas becomes similar, while it is not in the 'pure' plasmas (Fig. 3.2.5 (a)). Comparison of P_{NB_e} with or w/o taking into account the impurity contamination is shown in Fig. 3.2.5 (b). In the hydrogen plasmas, P_{NB_e} increases due to the impurity contamination, while it decreases in the neon plasmas. However, the errors due to the impurity contamination are less than 10 %.

The relation between T_{e0} and the electron heating power per an electron, $P_{NB\_e} / \langle n_e \rangle$, is plotted in Fig. 3.2.6. In the range of $P_{NB\_e} / \langle n_e \rangle < 5$ MW / 10^{19} m^{-3}, T_{e0} increases with $P_{NB\_e} / \langle n_e \rangle$, and any particular differences between the hydrogen and the neon plasmas can be recognized. The maximum T_{e0} obtained in the neon plasmas can be attributed to the increased heating power due to the small fraction of the NB shine-through power at the low-density regime. Above $P_{NB\_e} / \langle n_e \rangle > 5$ MW / 10^{19} m^{-3}, however, T_{e0} gradually decreases. These data are taken from the low-density discharges, where the estimation of P_{NB} and/or P_{NB_e} possibly has a systematic error. Hereinafter, we adopt one more criterion to eliminate the low-density data; i.e. $P_{NB\_e} / \langle n_e \rangle < 5$ MW / 10^{19} m^{-3}.

3.2.3. Global electron energy confinement

Next, we compare the global energy confinement of the electrons in the hydrogen and the neon plasmas. The non-dimensional regression analysis of the experimental electron energy confinement time, $\tau_{E\_e}^{exp}$ ($\equiv W_{e\_kin} / P_{NB\_e}$) is examined. In the non-dimensional form, $\tau_{E\_e}^{exp}$ can be expressed as

$$\tau_{E\_e}^{exp}\,\Omega_e \propto B_0\,\tau_{E\_e}^{exp} \propto (\rho_e^*)^{\phi}(\nu^*)^{\gamma}(\beta_e)^{\eta}, \tag{3.2.1}$$

where Ω_e is the electron gyro frequency, $\rho_e^* = \rho_e / a$ is the normalized electron gyro radius, ν^* is the collisionality, and β_e is the normalized electron pressure [2]. For the hydrogen data, however, the linear correlation coefficients of each components are 0.89, 0.35 and 0.54 for ρ_e^*, ν^*, and β_e, respectively. Here, we neglect the dependence on ν^* and β_e, since these are not strongly correlating with $\tau_{E\_e}^{exp}$. Regression analysis with ρ_e^* alone gives;

$$B_0\,\tau_{E\_e}^{exp}\,(\mathrm{H}) = 3.57 \times 10^{-13}\,(\rho_e^*)^{-2.74\pm0.07}. \tag{3.2.2}$$

As for the neon data, the linear correlation coefficients for each components are 0.91, 0.49 and 0.27 for ρ_e^*, ν^*, and β_e, respectively. Again, ν^* and β_e are not strongly correlating with $\tau_{E\_e}^{exp}$. Regression analysis with ρ_e^* alone results in

$$B_0\,\tau_{E\_e}^{exp}\,(\mathrm{Ne}) = 1.15 \times 10^{-12}\,(\rho_e^*)^{-2.61\pm0.09}. \tag{3.2.3}$$

In both of the hydrogen and the neon plasmas, $B_0\,\tau_{E\_e}^{exp}$ is strongly related to ρ_e^* and the exponents are identical within the standard deviations. These relations are plotted in Fig. 3.2.7 (a). This suggests that both plasmas have similar parameter dependence of the global electron energy confinement. The difference in the coefficients between Eqs. (3.2.2) and (3.2.3) is possibly due to the small ρ_e^* of $\sim 10^{-4}$ (note that even the small difference of 0.1 in the exponents causes an error of factor 2.5 in the coefficients). To compare the coefficients more accurately, we assume a model equation with the exponent of - 2.7;

$$\tau_{E\_e}^{fit}\,\Omega_e \propto B_0\,\tau_{E\_e}^{fit} \propto (\rho_e^*)^{-2.7}. \tag{3.2.4}$$

In the gyro-Bohm model, where micro-turbulences are considered as the cause of the anomalous energy transport [3, 4], the exponent of - 3 is assumed, while it is - 2 in the Bohm model, for example (see Appendix, and note that ρ_i^* is used instead of ρ_e^*, in these models). Equation (4) can be rewritten using the conventional terms as below;

$$\tau_{E\_e}^{fit} = C_0\,a^{2.30}\,R^{0.574}\,B_0^{0.723}\,P_{NB\_e}^{-0.574}\,\langle n_e\rangle^{0.574}, \tag{3.2.5}$$

where C_0 is the fitting parameter, and the units of each terms are; m, m, T, MW, and $10^{19}\,\mathrm{m}^{-3}$, for a, R, B_0, P_{NB_e}, and $\langle n_e\rangle$, respectively. The exponents are determined using the relations in the Appendix (see Table A.1). Fitting the data with Eq. (3.2.5), the distributions of $\tau_{E\_e}^{exp}$ in the plasmas with different ion species can be compared. Using hydrogen dataset, C_0 = 0.060±0.007 is obtained, while C_0 = 0.056±0.004 is obtained with the neon dataset. In both

cases, C_0 is identical within the standard deviations. Assuming $C_0 = 0.06$, $\tau_{E\_e}^{exp}$ and $\tau_{E\_e}^{fit}$ are compared in Fig. 3.2.7 (b). As is seen in the figure, $\tau_{E\_e}^{fit}$ well reproduces $\tau_{E\_e}^{exp}$, and its absolute value is similar in both of the hydrogen and the neon plasmas.

3.2.4. Discussion

The results obtained here are contrastive to the Z-mode [5] and the RI-mode [6 - 8] in tokamaks, where a reduction of the electron thermal diffusivity induced by the impurity (including the neon) gas puff has been observed. In LHD, where the high-energy neutral beam injection is the main heating method and therefore the electron heating is dominant, the electron energy confinement is important to study the whole plasma confinement. In the fusion reactor plasmas, where α particles are the energy source, the electron heating also dominates. The result of this study shows that the global electron energy confinement is not depending on the ion species, or the ion gyro radius. Instead, the electron energy confinement time shows a strong dependence on the electron gyro radius. In the gyro-Bohm model, the turbulence that drives the anomalous transport has a scale length of the order of the ion gyro radius [9 - 12]. On the analogy of this, our result suggests that the scale length of the turbulence in LHD plasmas will have the order of the electron gyro radius.

References

[1] U. Stroth et al., Nucl. Fusion **36**, 1063 (1996).

[2] H. Yamada et al., Plasma Phys. Control. Fusion **43**, A55 (2001).

[3] R. J. Goldston et al., Bull. Am. Phys. Soc. **34**, 1964 (1989).

[4] M. Murakami et al., Phys. Fluids B **3**, 2261 (1991).

[5] E. A. Lazarus et al., Nucl. Fusion **25**, 135 (1985).

[6] G. R. McKee et al., Phys. Plasmas **7**, 1870 (2000).

[7] A. M. Messiaen et al, Phys. Rev. Lett. **77**, 2487 (1996).

[8] K. W. Hills et al., Phys. Plasmas **6**, 877 (1999).

[9] F. W. Perkins, in *Heating in Toroidal Plasmas*, Rome, 1984 (International School of Plasma Physics, Varenna, 1984), Vol. 2, p. 977.

[10] R. J. Goldston, et al., Bull. Am. Phys. Soc. **34**, 1964 (1989).

[11] M. Murakami, et al., Phys. Fluids B **3**, 2261 (1991).

[12] J. G. Cordey et al., Nucl. Fusion **39**, 301 (1999).

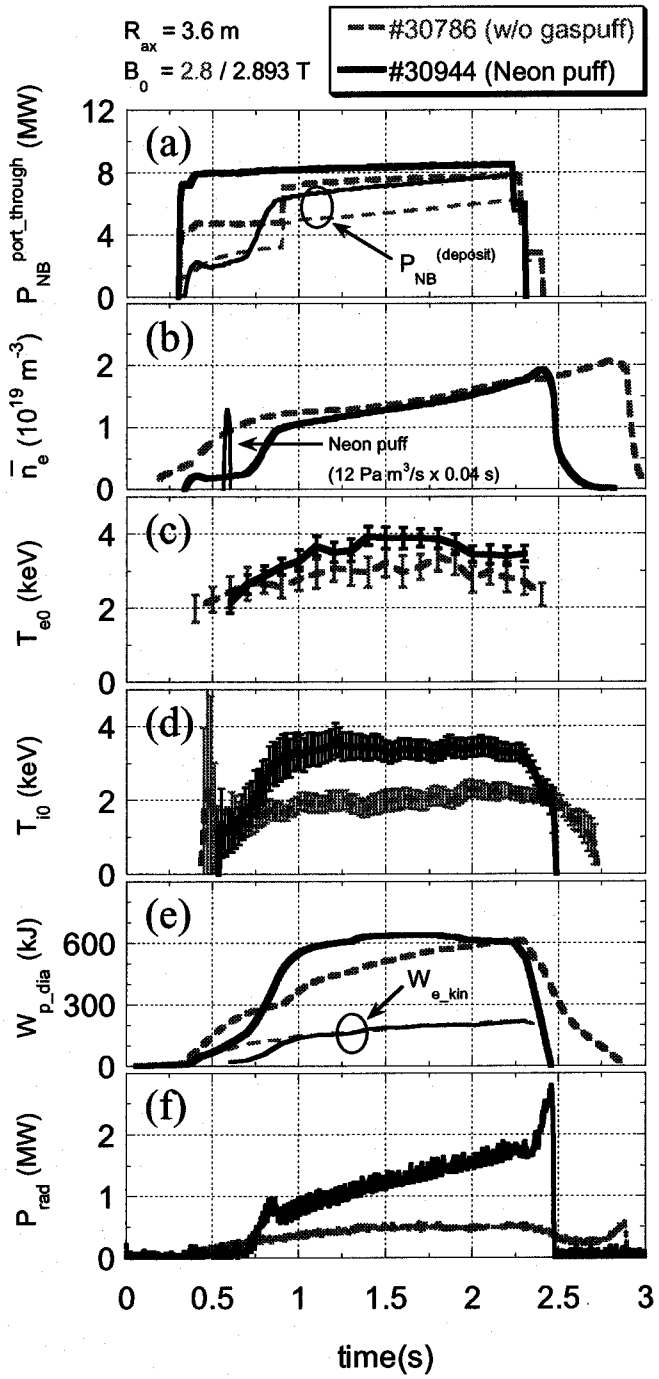

Fig. 3.2.1. Comparison between the neon discharge (solid lines) and the hydrogen discharge (broken lines). From top to bottom, shown are (a) NB port-through power, $P_{NB}^{port\_through}$, and NB deposition power, $P_{NB}^{(deposit)}$, the line-averaged electron density, $\bar{n}_e$, (c) the electron temperature at the plasma center, T_{e0}, (d) the ion temperature at the plasma center, T_{i0}, (e) the plasma stored energy estimated from diamagnetic signals, W_{p_dia}, and the electron stored energy estimated from the profiles of electron temperature and density, W_{e_kin}, and (f) the radiation loss, P_{rad}.

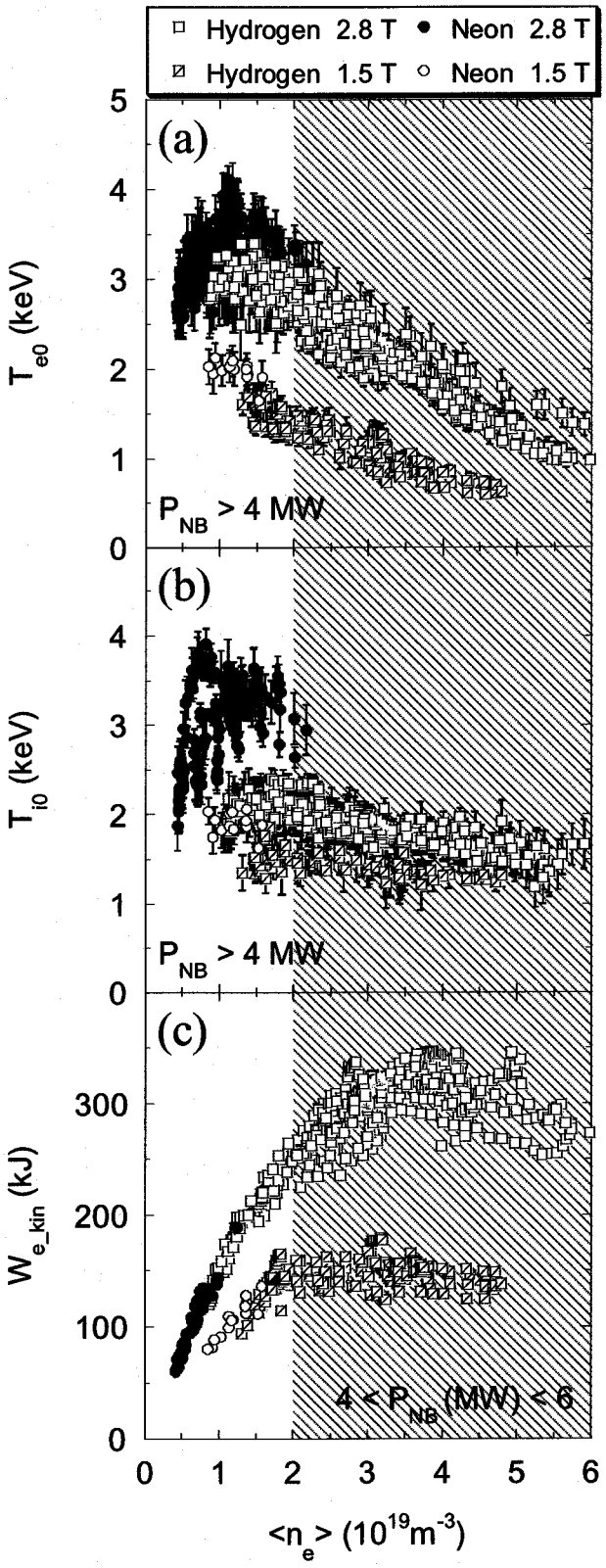

Fig. 3.2.2. Distributions of (a) T_{e0}, (b) T_{i0}, and (c) W_{e_kin}.

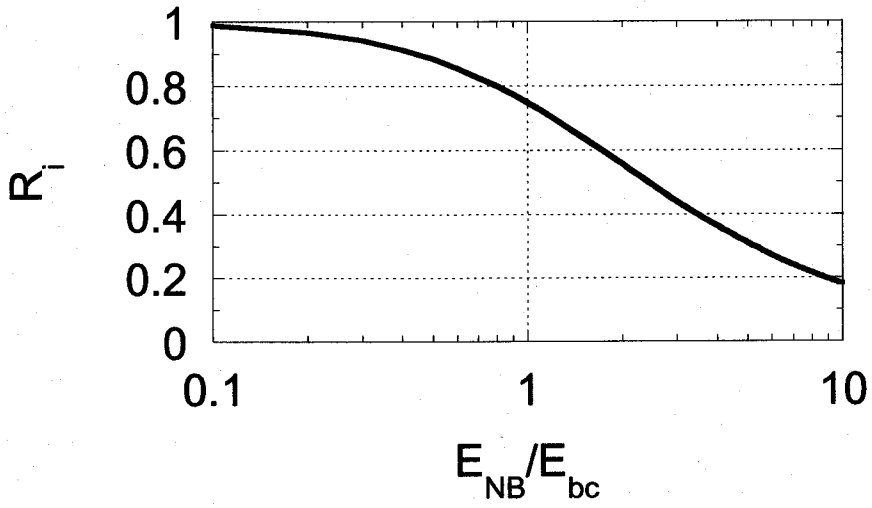

Fig. 3.2.3. The fraction of the beam energy (E_{NB}) to the critical energy (E_{bc}) vs the ratio of the ion heating power, R_i.

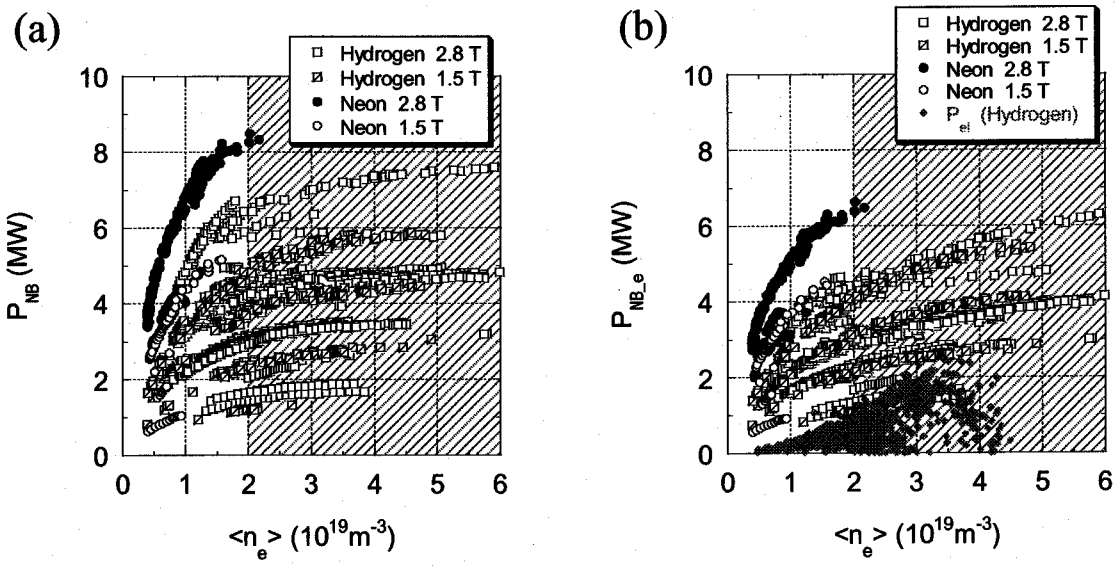

Fig. 3.2.4. (a) Distribution of P_{NB}. (b) Distribution of the electron heating power, P_{NB_e}, and the heat transfer from electrons to ions, P_{ei}.

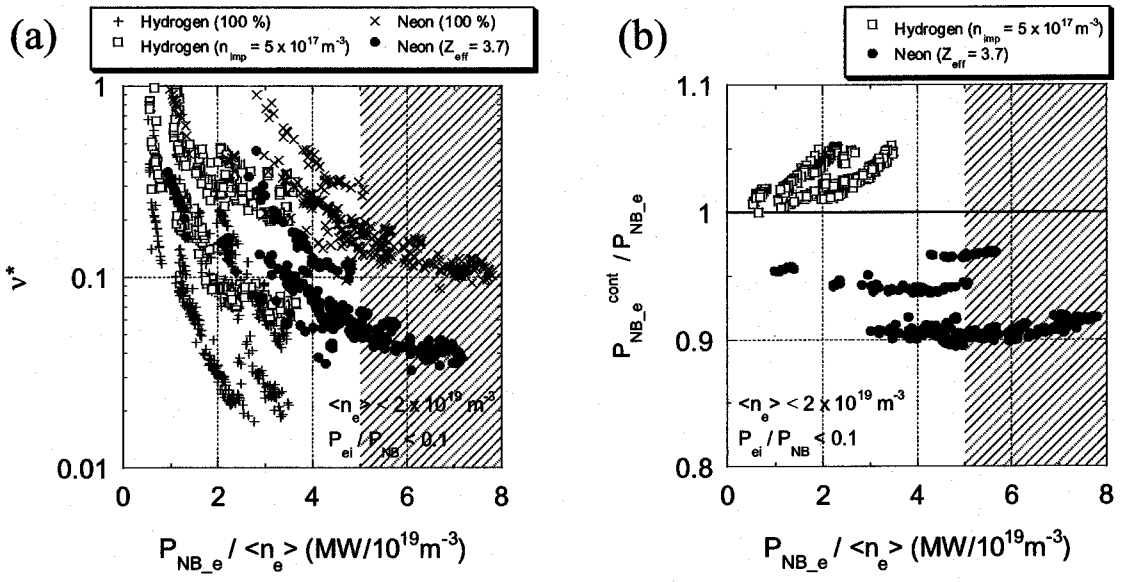

Fig. 3.2.5. Error resulted from the impurity contamination. (a) Distribution of the collisionality, ν^*, and (b) the comparison between P_{NB_e} and that estimated with the impurity contamination, $P_{NB\_e}^{cont}$.

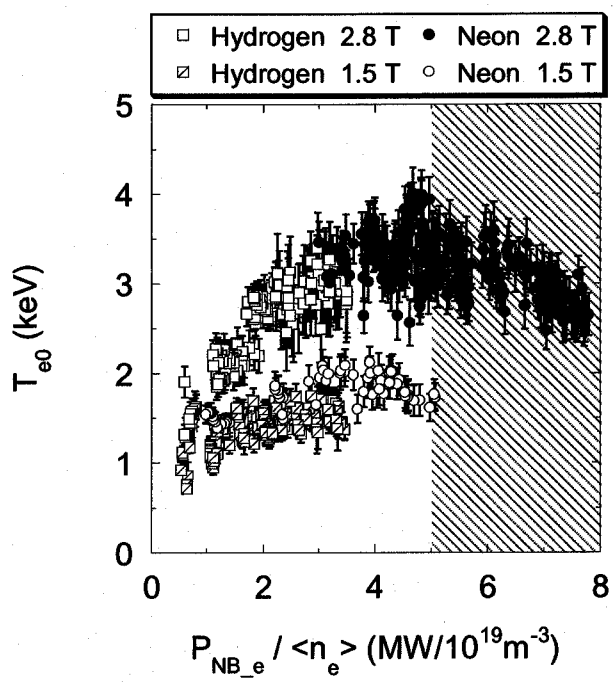

Fig. 3.2.6. Dependence of T_{e0} on P_{NB_e} / $\langle n_e \rangle$. Plotted are the data that satisfy the two criteria; $\langle n_e \rangle < 2 \times 10^{19}$ m^{-3}, and $P_{ei} / P_{NB} < 0.1$.

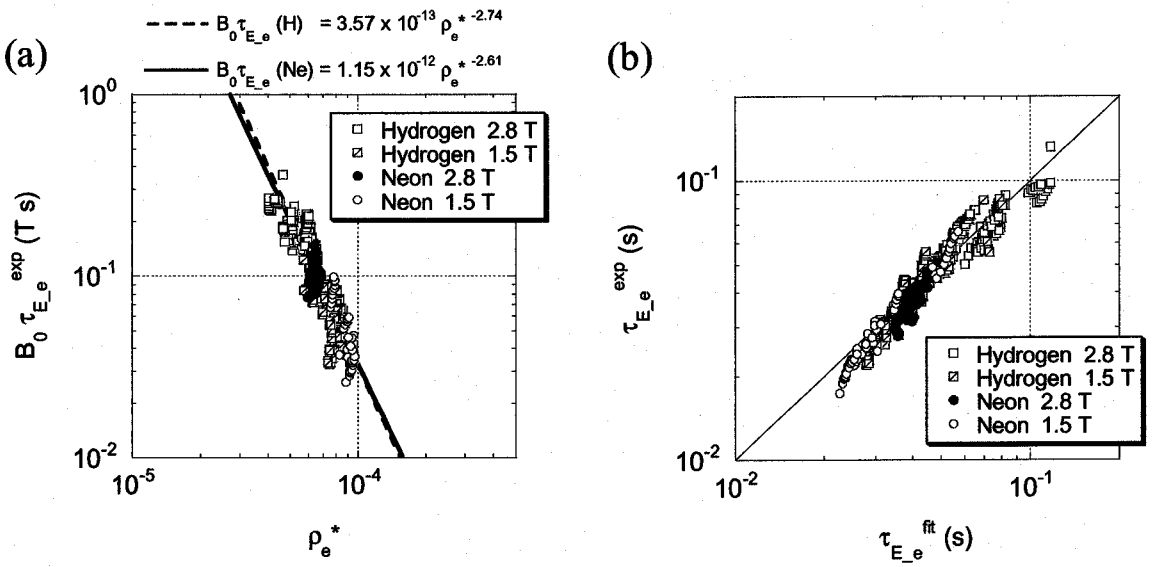

Fig. 3.2.7. (a) Dependence of $B_0\ \tau_{E\_e}{}^{exp}$ on ρ_e*, and (b) the comparison of $\tau_{E\_e}{}^{exp}$ and $\tau_{E\_e}{}^{fit}$. Plotted are the data that satisfy the three criteria; $\langle n_e \rangle < 2 \times 10^{19}\,m^{-3}$, $P_{ei} / P_{NB} < 0.1$, and $P_{NB\_e} / \langle n_e \rangle < 5\,MW / 10^{19}\,m^{-3}$.

3.3. Summary

Methane gas puff experiment has been carried out on LHD. Although the CH_4 discharges itself showed only slight difference compared with the hydrogen gas puff shots, a significant improvement was observed in the shots fuelled with hydrogen ice-pellets, following the CH_4 discharges. The intensity of metal impurity emissions in the visible and soft X-ray range, the total radiation loss, and the hump observed in p_{rad} profile are largely reduced in the pellet shots after CH_4 discharges. These phenomena together with the increased n_e at the edge region are that expected as RTC effect. In addition, the decreasing rate of n_e was mitigated in the pellet shot after CH_4 discharges. The transport analysis has revealed 40% reduction in D at ρ = 0.5, and χ_{eff} was also reduced. The improvement in the confinement is not due to the reduction of the radiation loss, but due to the reduction of D and χ_{eff}.

Neon gas puff discharges have been successfully performed on LHD. Both of the electron and the ion temperature at the plasma center are higher in the neon plasmas compared with the hydrogen plasmas at the same density and NB port-through power. The beam deposition power is increased in the neon plasmas especially at the low-density regime. The dependence of the electron temperature on the heating power per electron is similar in both cases. The non-dimensional analysis also reveals that the global energy confinement in neon plasmas is similar to that of hydrogen plasmas. In both cases, the global electron energy confinement strongly depends on the electron gyro-radius. This suggests that the scale length of the turbulence that drives the anomalous transport is determined by the electron gyro-radius in LHD, where the electron heating by the high-energy beam ions is dominant as in the fusion reactor. A new scaling law that can describe the global electron energy confinement of LHD plasmas is obtained as Eq. (3.2.5) together with the coefficient of C_0 = 0.06. This equation can be applied to both of the hydrogen and the neon plasmas.

These are the good examples showing that the gas puffing can be a powerful tool due to its flexibility in the working gas selection. Gas puffing enables the experiments needed to understand the important plasma physics, such as the recycling and the confinement property, as has been shown.

There were few operational problems to carry out the impurity gas puff experiments on LHD. In tokamaks, such an experiment might be more difficult since the current profile also changes with the Z_{eff} profile and the risk of current disruption probably increases. Although the enhanced radiation tends to terminate the plasma, such a radiative collapse is

less harmful to the vacuum vessel wall compared with the current disruption, which induces a large electro-magnetic force on the device structure. The experimental results of this chapter demonstrate that LHD has a wide permission range, which enables various plasma experiments.

Chapter 4 Development of CT Injector for LHD

CT injection is one of the most recent fueling methods, and has a possibility of the direct fueling into the core of high-temperature fusion plasma. In LHD, CT injection experiment is scheduled in near future. This chapter describes the theoretical bases of CT injection and the development of the CT injector for LHD, which is named SPICA (SPheromak Injector using Conical Accelerator). At first, the background of CT injection experiment in LHD is described in section 4.1. CT orbit in the LHD magnetic field is calculated in section 4.2. In section 4.3, the point-model is introduced and the design of CT acceleration electrode is given. Machine overview of SPICA and the experimental results are given in section 4.4. Summary is given in section 4.5.

4.1. Introduction to the CT injection experiment

4.1.1. Background of the CT injection experiment

Recently, a new type of fueling method, compact toroid (CT) injection, has been proposed [1 - 5]. CT is a dense magnetized plasmoid and can be easily accelerated over hundreds of km/s by the electro-magnetic force. When a CT is in a magnetic field, magnetic pressure is exerted on the CT surface and it is pushed out to the weaker magnetic field region due to the magnetic pressure gradient. A high-speed CT that has a sufficient kinetic energy can penetrate into the hot main plasma that is confined in the strong magnetic field. Magnetic reconnection is supposed to take place in the main plasma and then the particle confined in the CT is fueled to the main plasma. The peaked density profile obtained after the center fueling is favorable because the density gradient causes the rotation of plasmas. The plasma rotation is considered to be favorable for the better confinement. The large momentum carried by the high-speed CT is also useful to rotate the main plasma.

Spheromak is one of the CT configurations where both of the toroidal and the poloidal magnetic fields are generated and sustained by currents flowing inside the spheromak itself [6]. This CT is usually formed using a co-axial plasma gun, and accelerated by another co-axial accelerator connected to the formation electrode [7]. An example of the co-axial magnetized plasma gun, consisting of two stages of formation and acceleration, is shown in Fig. 4.1.1. Formation scheme of spheromak-type CT by the co-axial magnetized plasma gun

is explained in Fig. 4.1.2 [4]. At first, the biasing poloidal (axial direction) magnetic field is applied on the formation electrode (Fig. 4.1.2 (a)). Next, the working gas is injected and then the formation bank is triggered to ionize the gas. The radial formation current $\boldsymbol{J}$ flows from the outer electrode to the inner electrode through the plasma and generates the toroidal magnetic field $\boldsymbol{B}$ (Fig. 4.1.2 (b)). The plasma is pushed out to the acceleration electrode due to the $\boldsymbol{J} \times \boldsymbol{B}$ force. As the plasma moves from the formation electrode to the acceleration electrode, the poloidal magnetic field strength becomes smaller. Therefore, the toroidal current is induced within the plasma to preserve the poloidal magnetic flux (Fig. 4.1.2 (c)). After the plasma moves away from the formation electrode, the magnetic reconnection takes place and the plasma becomes to the isolated plasma ring (Fig. 4.1.2 (d)). When the plasma ring deeply enters to the acceleration electrode, the acceleration bank is triggered and the radial current accelerates the plasma ring with its $\boldsymbol{J} \times \boldsymbol{B}$ force. Finally, the plasma ring is shot out from the acceleration electrode. Toroidal and poloidal magnetic field in the plasma ring relaxes to the minimum energy state, which is given by the force-free configuration [8]. A spherical plasmoid that has the force-free magnetic field profile is called the spheromak.

CT acceleration has been first demonstrated in RACE (Ring ACcelerator Experiment) project at Lawrence Livermore National Laboratory in USA [9 - 11]. The main object of the RACE was to establish the CT acceleration technology. An accelerated CT is compressed by a focusing cone to achieve the high energy density, which has a wide range application such as an intense X-ray source. Formation part of the RACE is 0.5 m long with an outer (inner) radius of 0.175 m (0.1 m). RACE is equipped with a 6 m long acceleration electrode and conically converging electrode for ring focusing. High speed CT of 2,500 km/s and high CT kinetic energy of 40 kJ (400 km/s and 0.5 mg) were reported from RACE. The largest CT acceleration device is the MARAUDER operated in US Air Force Phillips Laboratory [12, 13]. The outer (inner) radius of the formation electrode is 0.5239 m (0.4477 m).

CT injection into the high temperature plasmas has been examined in small and medium size tokamaks, such as TdeV [14, 15] and STOR-M [16, 17] in Canada, Caltech's ENCORE [18, 19] and TEXT-U [20] in USA, and JFT-2M [4, 21] in Japan. CT fueling on the tokamak plasma with the toroidal magnetic field strength of up to 1.5 T was demonstrated on TdeV (R = 0.86 m, a = 0.27 m, where R and a is the major and the minor radius of the torus, respectively). Central penetration of the CT was observed at < 1 T toroidal magnetic field. The fueling efficiency was estimated as more than 50 %. Confinement improvement associated with the H-mode transition due to the CT injection was also observed. In STOR-M

(R = 0.46 m, a = 0.12 m), tangential CT injection was applied and resulted in the brief drop of the loop voltage, increase of the plasma beta, and decrease of the H_α radiation level. Current drive by CT injection, based on the idea of the helicity conservation, was demonstrated on ENCORE (R = 0.38 m, a = 0.12 m). Helicity is a measure of the linked flux and defined as a product of toroidal and poloidal fluxes. Simple and small (outer electrode is 0.051 m in diameter) plasma gun without acceleration electrode was adopted in the experiment. Increase or decrease in the plasma current was observed according to the sign of the helicity. Experimental results from TEXT-U (R = 1.05 m, a = 0.27 m) have pointed out that the plasma gun should avoid the linkage with the stray magnetic field. The trapped magnetic flux causes the drag force on the CT and resultant penetration is shallow. In JFT-2M, CT injection into the high-performance H-mode plasmas has been carried out. Rapid increase in the line-averaged electron density of 0.2×10^{19} m^{-3} was observed and the fueling efficiency was estimated as ~ 20 %. Acceleration electrode of the plasma gun is 1 m long with outer and inner radius of 0.055 m and 0.024 m, respectively. CT is compressed to 0.07 m radius in the focus cone at the end of the acceleration electrode. The maximum CT density of 9×10^{21} m^{-3} and the maximum CT velocity of 300km/s have been achieved.

In Fig. 4.1.3, compared are the sizes of these CT injectors, where the horizontal axis indicates the length of the acceleration part and the vertical axis indicates the volume of the target plasmas. The radius of each circle corresponds to the outer radius of the formation part. As will be described later, SPICA has an acceleration electrode of 2.6 m long and a formation electrode of 0.172 m outer radius. These are the largest among the CT injectors utilized in the small / medium tokamaks. The plasma volume of LHD (28 m^3) is also the largest in the world as the target of the CT injection experiment.

As for the detailed review of the CT injection experiment, see refs 4 and 5.

4.1.2. CT injection in helical devices

Since the magnetic field structure in a helical device is more complicated than in tokamaks, the injected CT traces a complicated three-dimensional trajectory. In some cases, a CT that is vertically injected traces tangential orbit in the main plasma. Such a tangentially moving CT has a trajectory that is parallel to the equilibrium magnetic field, and causes the main plasma rotation as a tangential NB injection. In the case of LHD, we are planning to inject a spheromak weighing 0.1 mg with over 200 km/s of velocity into the main plasma weighing 1

mg. A large CT momentum may induce the rotation of the main plasma. Tangential injection of CT is difficult in high magnetic field devices because the CT needs to pass nearby the magnetic field coils where a strong magnetic field gradient exists. Therefore, the possibility of momentum injection other than the tangential injection in a helical device is favorable.

Another possible use of CT injection than fueling and momentum injection is the direct control of the electric field using electrically non-neutral CT. The electric field structure of the main plasma is thought to have a very important influence on the confinement property as has been shown in H-mode studies. The direct control of the electric field profile using the biased electrode has been carried out in many devices [22 - 25]. These biased electrode experiments have shown efficient improvement in the confinement property although such a solid electrode cannot be inserted into hot fusion plasma. The non-neutral CT might be generated using a biased electrode set at the CT injection port. A non-neutral CT with velocity $\boldsymbol{v}$ and electric charge q injected into the magnetic field $\boldsymbol{B}$ traces a curved trajectory due to Lorentz force, $q\,\boldsymbol{v} \times \boldsymbol{B}$. Under some circumstances, the non-neutral CT cannot reach the main plasma. Three-dimensional orbit of the non-neutral CT in a helical magnetic field will be also analyzed in section 4.2.

4.1.3. Design parameters of CT injector for LHD

The standard magnetic flux surfaces in LHD, which are calculated using the three-dimensional equilibrium code VMEC [26], are shown in Fig. 4.1.4. Two sets of flux surfaces calculated with low averaged beta ($<\beta> = 2.04 \times 10^{-5}$) and high averaged beta ($<\beta> = 4.56 \times 10^{-2}$) are depicted. As can be seen in the figure, the magnetic surfaces are well approximated by ovals especially in the low beta case (Fig. 4.1.4 (a)), and this will be used in some parts of the calculation in section 4.2 for simplicity.

The design parameters of CT injector for LHD are summarized in Table 4.1.1. About 0.1 mg of fuel plasmoid, which corresponds to about 10 % of typical LHD plasma particles, is supposed to be supplied. In section 4.2, it is assumed that CT is a perfect diamagnetic sphere of radius $a_{CT} = 0.1$ m and the electron density of 10^{22} m^{-3}. The case of hydrogen CT injection into hydrogen LHD plasma is considered there. The magnetic field in LHD is the standard configuration with a magnetic field of 1.5 T at the magnetic axis. LHD employs several kinds of observation and/or NB injection ports, namely, outer (O-) ports, inner (I-) ports, upper (U-) ports, lower (L-) ports, and tangential (T-) ports. Although one can choose any one of these

ports to set up the CT injector, T-port and I-port seem to be unfavorable, because the CT orbit through these ports should pass nearby the helical coils where a strong magnetic field gradient exists. Therefore, O-port and L-port are chosen for the orbit calculation. Note that L-port and U-port are the same in a physical sense because of the symmetrical configuration of LHD. As shown in Fig. 4.1.5, the CT orbit calculation in section 4.2 starts from one of the cross points of the lattices defined at O-port and L-port. The lattice has 0.1 m intervals, and a CT is assumed to have an initial velocity vector normal to the lattice.

References

[1] P. B. Parks, Phys. Rev. Lett. **61**, 1364 (1988).

[2] L. J. Perkins, S. K. Ho and J. H. Hammer, Nucl. Fusion **28**, 1365 (1988).

[3] W. A. Newcomb, Phys. Fluids B **3**, 1818 (1991).

[4] T. Uyama and M. Nagata, J. Plasma and Fusion Res. **74**, 200 (1998), in Japanese.

[5] K. Thomassen *et al.*, Fusion Tech. **34**, 86 (1998).

[6] M. N. Rosenbruth and M. N. Bussac, Nucl. Fusion **19**, 489 (1979).

[7] Charles W. Hartman and James H. Hammer, Phys. Rev. Lett. **48**, 929 (1982).

[8] J. B. Taylor, Phys. Rev. Lett. **33**, 1139 (1974).

[9] J. H. Hammer, C. W. Hartman, J. L. Eddleman, H. S. McLean, Phys. Rev. Letters **61**, 2843 (1988).

[10] J. H. Hammer, J. L. Eddleman, C. W. Hartman, H. S. McLean and A. W. Molvik, Phys. Fluids B **3**, 2236 (1991).

[11] J. Eddleman *et al.*, "Final Report on the LLNL Compact Torus Acceleration Project", UCRL-ID-120238, Lawrence Livermore National Laboratory (Mar. 1995).

[12] E. L. Ruden *et al.*, Phys. Fluids B **4**, 1800 (1992).

[13] J. H. Degnan *et al.*, Phys. Fluids B **5**, 2938 (1993).

[14] R. Raman *et al.*, Phys. Rev. Lett. **73**, 3101 (1994).

[15] R. Raman *et al.*, paper presented at the 24th EPS Conference on Controlled Fusion and Plasma Physics, Berchtesgaden, Germany (1997).

[16] C. Xiao *et al.*, IAEA-CN-64/AP1-1, in 16th IAEA Fusion Energy Conference, Montreal, Canada (1996).

[17] C. Xiao *et al.*, IAEA-CN-77/EXP4/31, in 18th IAEA Fusion Energy Conference, Sorrento, Italy (2000).

[18] M. R. Brown and P. M. Bellan, Phys. Rev. Lett. **64**, 2144 (1990).

[19] M. R. Brown and P. M. Bellan, Nucl. Fusion **32**, 1125 (1992).

[20] J. Yee and P. M. Bellan, Nucl. Fusion **38**, 711 (1998).

[21] T. Ogawa *et al.*, Nucl. Fusion **39**, 1911 (1999).

[22] R. J. Taylor, M. L. Brown, B. D. Fried, H. Grote, J. R. Liberati, G. J. Morales and P. Pribyl, Phys. Rev. Lett. **63**, 2365 (1989).

[23] L. G. Askinazi, V. E. Golant, S. V. Lebedev, V. A. Rozhanskij and M. Tendler, Nucl. Fusion **32**, 271 (1992).

[24] E. Y. Wang *et al.*, Nucl. Fusion **35**, 467 (1995).

[25] S. Inagaki *et al.*, Jpn. J. Appl. Phys. **36**, 3697 (1997).

[26] S. P. Hirshman, W. Van Rij and P. Merkel, Comput. Phys. Commun. **43**, 143 (1986).

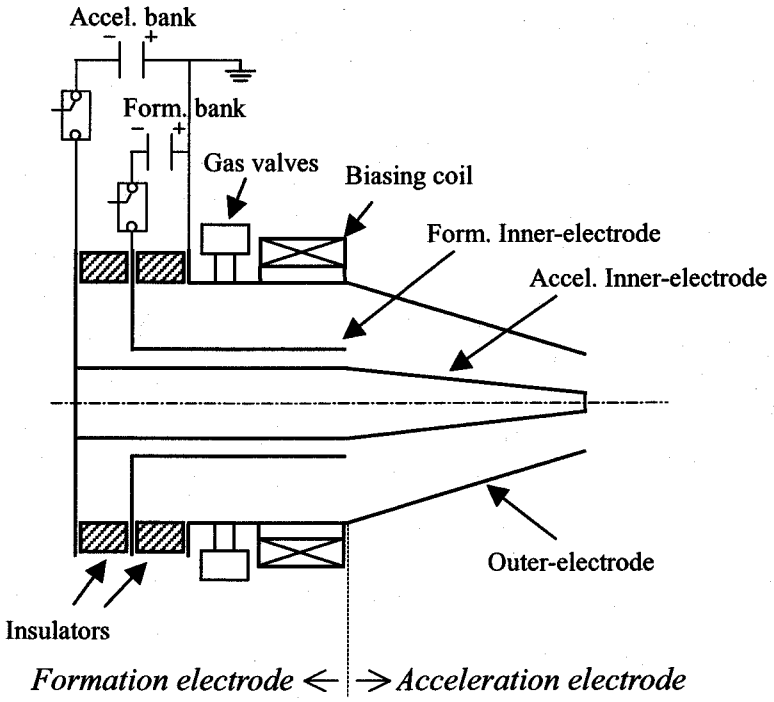

Fig. 4.1.1. Example of the co-axial magnetized plasma gun, consisting of two stages for CT formation and CT acceleration.

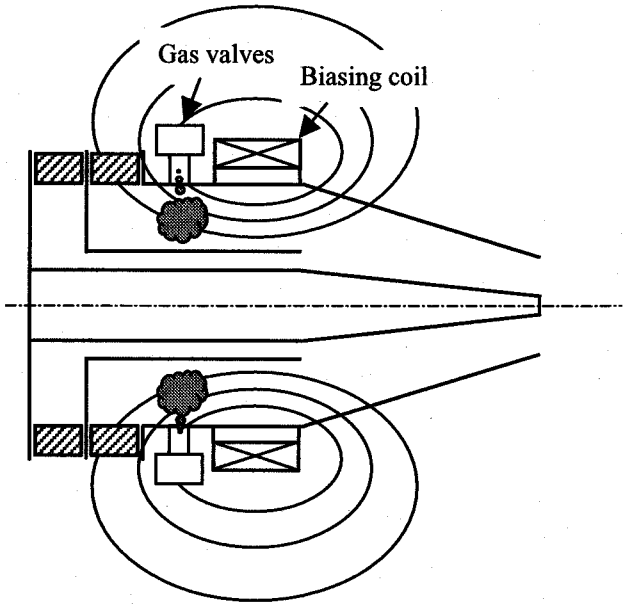

(a) Application of the bias magnetic field and pulsed gas injection.

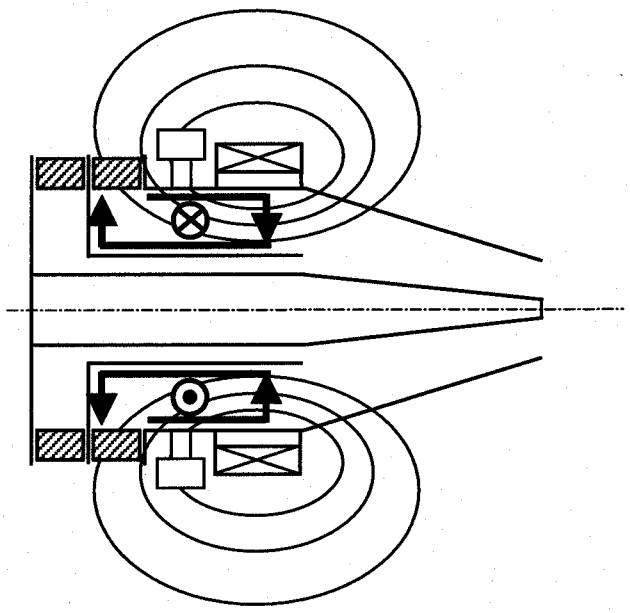

(b) Plasma production by the formation bank discharge.

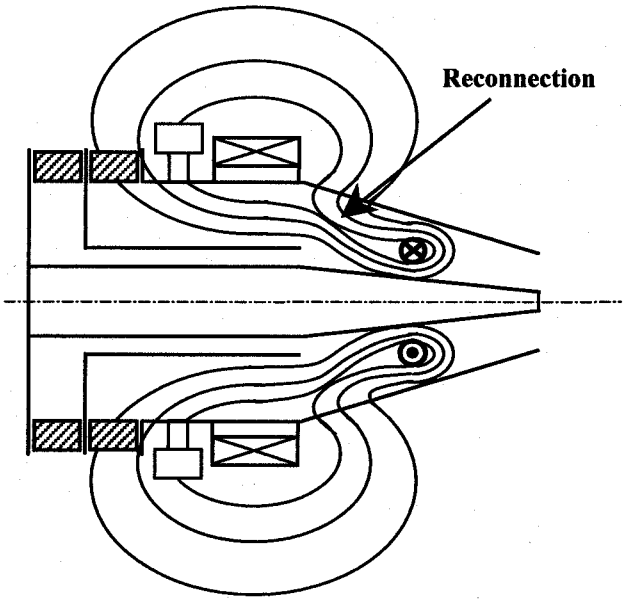

(c) Magnetized plasma ring is pushed out by the $\boldsymbol{J} \times \boldsymbol{B}$ force and magnetic reconnection takes place.

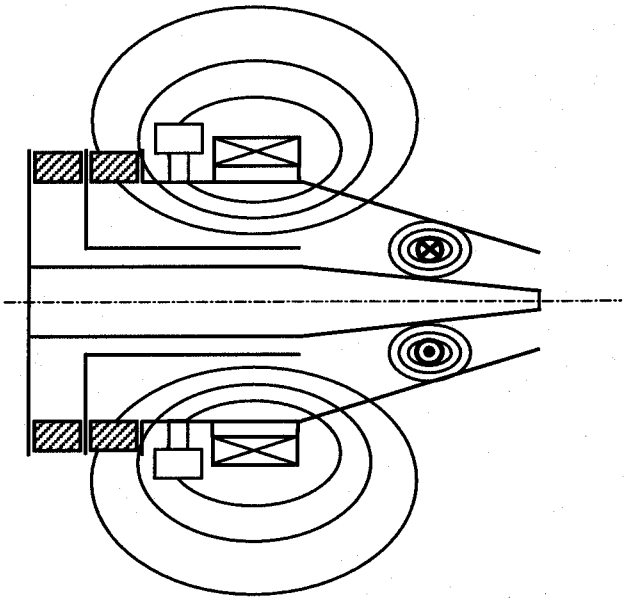

(d) Isolated plasma ring is formed after the magnetic reconnection.

Fig. 4.1.2. Formation scheme of spheromak-type CT by a co-axial magnetized plasma gun.

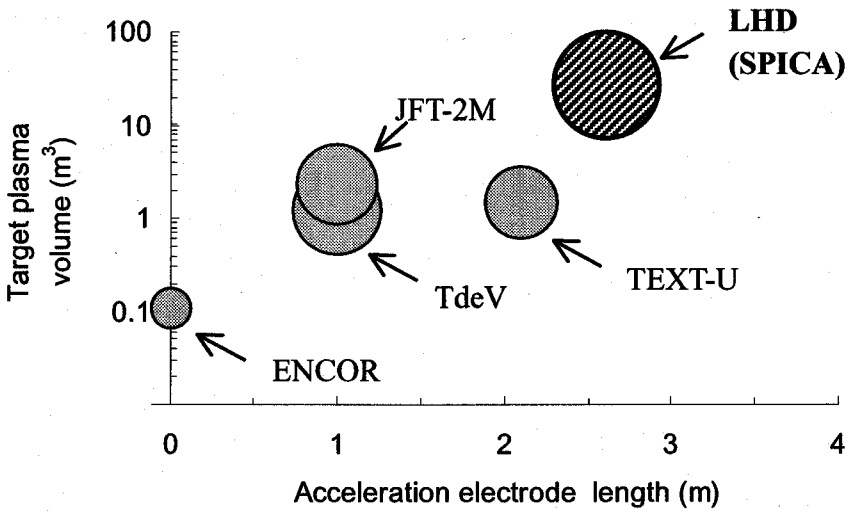

Fig. 4.1.3. Comparison of the CT injectors for fueling. The horizontal (vertical) axis indicates the length of the acceleration part (the volume of the target plasmas). The radius of each circle corresponds to the outer radius of the formation part.

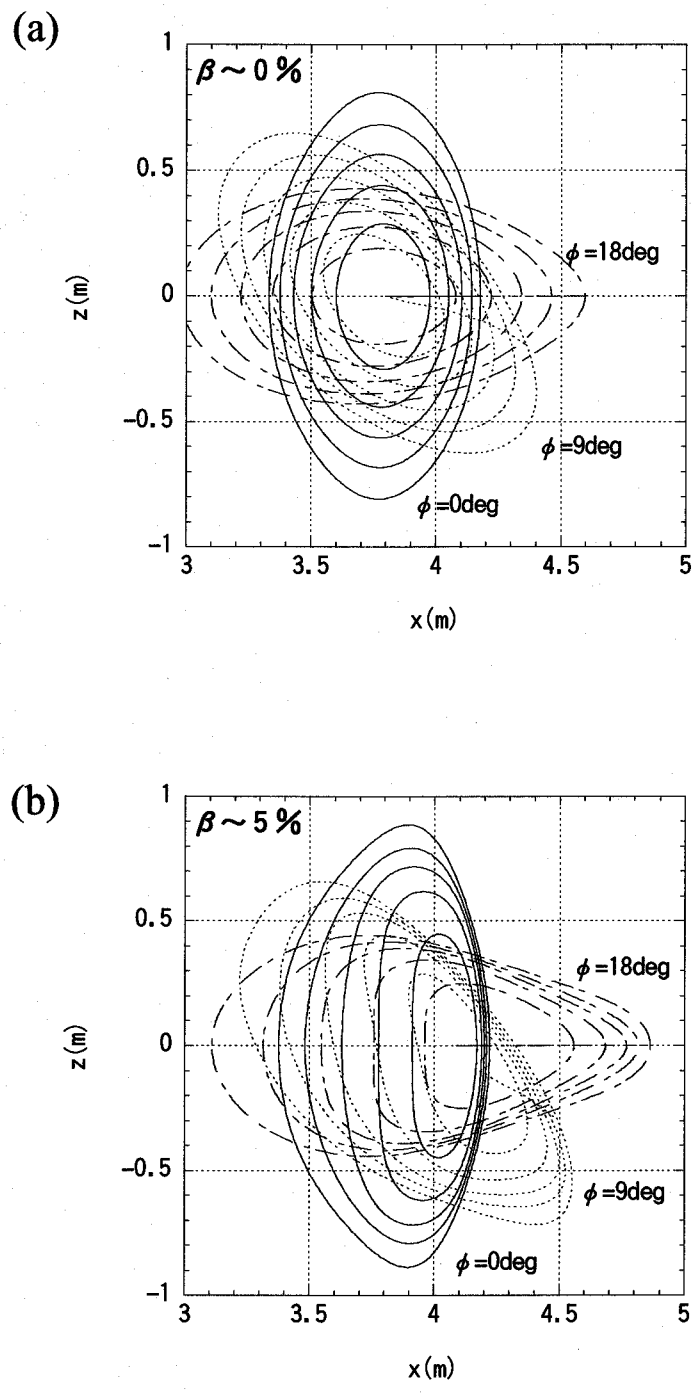

Fig. 4.1.4. Standard magnetic flux surfaces of LHD calculated in (a) low averaged beta condition ($<\beta> = 2.04 \times 10^{-5}$) and (b) high averaged beta condition ($<\beta> = 4.56 \times 10^{-2}$).

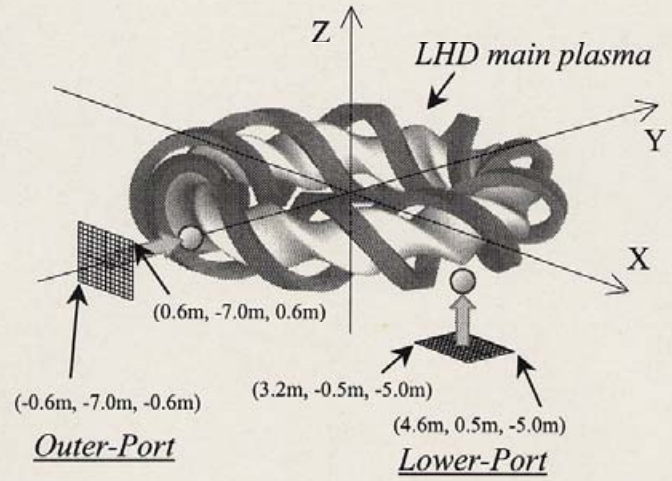

Fig. 4.1.5. Schematic view of starting grids for CT orbit calculation set at outer port and lower port. The interval between each grid is 0.1 m, and CT is injected into the main plasma from one of the cross points in the grids. The initial velocity vector of CT is normal to the starting grid.

Table 4.1.1. Design parameters of CT injector for LHD.

CT volume, V_{CT} (m^3)	1×10^{-3} to 5×10^{-3}
CT electron density, n_e (m^{-3})	1×10^{21} to 2×10^{22}
CT mass, m_{CT} (μg)	2 to 170
Particle inventory, N_{CT}	1×10^{18} to 1×10^{20}
CT magnetic field, B_{CT} (T)	1.0 to 3.0
CT initial velocity, v_0 (km/s)	200 to 500
CT maximum kinetic energy (kJ)	~ 20
CT electron temperature (eV)	10 to 100
Working gas	H_2, He, Ne etc.

4.2. CT orbit calculation

4.2.1. Calculation method

CT trajectories in a helical magnetic field are calculated while changing the initial injection velocity and the injection point, to determine the optimum conditions for CT injection (CTI) in LHD. The equation of motion of a CT in a magnetic field is given by

$$m_{\mathrm{CT}} \frac{\mathrm{d}\boldsymbol{v}}{\mathrm{d}t} = q\,\boldsymbol{v} \times \boldsymbol{B} + \boldsymbol{F}_{\nabla B^2}, \tag{4.2.1}$$

where m_{CT} is the CT mass and q is the electric charge of CT. The second term $\boldsymbol{F}_{\nabla B^2}$ is the force given by integrating the magnetic pressure $P_{\mathrm{m}} = B^2 / (2\mu_0)$ on the CT surface, and when the CT diameter is small enough compared to the scale length on which the magnetic pressure changes, $\boldsymbol{F}_{\nabla B^2}$ is approximated by the gradient of P_{m}, that is,

$$\boldsymbol{F}_{\nabla B^2} \equiv \int P_{\mathrm{m}}\,\mathrm{d}\boldsymbol{s} \approx \frac{V_{\mathrm{CT}}}{2\mu_0} \nabla B^2, \tag{4.2.2}$$

where V_{CT} is the CT volume.

Some terms are neglected in the equation of motion above. CT moving in the plasma is thought to radiate its power as Alfvén waves and sound waves [1, 2]. This mechanism causes a drag force, $\boldsymbol{F}_{\mathrm{WD}}$, as below;

$$\boldsymbol{F}_{\mathrm{WD}} = -2\pi I c_{\mathrm{s}} {a_{\mathrm{CT}}}^2 \rho_{\mathrm{LHD}} \boldsymbol{v}, \tag{4.2.3}$$

$$I = \left(\frac{2}{9}\right) + \left(\frac{2}{9}\log_{\mathrm{e}} \frac{v_{\mathrm{A}}}{c_{\mathrm{s}}} - 0.37\right), \tag{4.2.4}$$

where I is given by Newcomb [1], v_{A} is the Alfvén velocity, c_{s} is the sound velocity, and ρ_{LHD} is the mass density of the LHD plasma. Using typical parameters of LHD plasma and CT (see Table 4.1.1), $\boldsymbol{F}_{\mathrm{WD}}$ is less than one percent of $\boldsymbol{F}_{\nabla B^2}$. Stokes drag force due to viscous losses also has a similar order or less [2]. Therefore, these are neglected in this study.

A term that describes the interaction between the LHD magnetic field and the magnetic moment $\boldsymbol{\mu}$ of CT is also neglected. Toroidal current flowing inside the spheromak is the source of $\boldsymbol{\mu}$. Interaction with the LHD magnetic field generates the force $\boldsymbol{F}_{\nabla \boldsymbol{\mu}\cdot\boldsymbol{B}} = \nabla(\boldsymbol{\mu} \cdot \boldsymbol{B})$

on the CT. While other studies on CT orbit calculation in refs. 2 - 4 deal with this force, we neglect this for three reasons. First, $\boldsymbol{F}_{\nabla\mu\cdot\boldsymbol{B}}$ is less than $0.1 \times \boldsymbol{F}_{\nabla B^2}$. Second, since the CT is assumed to have a perfect diamagnetic nature, toroidal currents in the CT cannot interact with the magnetic field outside. And third, even if $\boldsymbol{F}_{\nabla\mu\cdot\boldsymbol{B}}$ were taken into account, this force, which can be described as $\nabla(\mu B \cos\alpha)$ using the angle α between $\boldsymbol{\mu}$ and $\boldsymbol{B}$, would change very rapidly. Therefore, CT orbit of the 0th order is not affected by $\boldsymbol{F}_{\nabla\mu\cdot\boldsymbol{B}}$. This change in angle α is due to the torque $d^2\alpha/dt^2 = (\boldsymbol{\mu}\times\boldsymbol{B}) / I_m$, where I_m is the moment of inertia of the CT (= 0.4 $a_{CT}^2 m_{CT}$), and the characteristic time of tilting, $\tau_{tilt} \approx (\mu B / I_m)^{-1/2}$ is less than a microsecond in our case.

In the case of non-neutral CT, one should consider the term $q\boldsymbol{E}$ when the CT is in the electric field $\boldsymbol{E}$. This term is neglected because no electric field in the LHD plasma is assumed.

The fourth-order Runge-Kutta method is used to solve Eq. (4.2.1). The LHD magnetic field is calculated using the Bio-Savart law. CT orbit calculation is carried out in the Cartesian coordinates (x, y, z) as defined in Fig. 4.1.4. It is convenient to convert this into toroidal coordinates (ρ, θ, ϕ), where ρ is the normalized radius, θ is the poloidal angle, and ϕ is the toroidal angle. As the first step, flux surfaces are approximated by ovals with no shift of the magnetic axis (similar to that in low beta equilibrium shown in Fig. 4.1.3 (a)), to reduce calculation time. In this approximation, ρ, θ, and ϕ, are obtained from x, y, and z as follows:

$$\phi = \tan^{-1}(y/x), \tag{4.2.5}$$

$$\theta = \tan^{-1}(z/r), \tag{4.2.6}$$

$$\rho = \frac{(r^2+z^2)^{1/2}}{((a\cos(\theta+5\varphi))^2+(b\sin(\theta+5\varphi))^2)^{1/2}}, \tag{4.2.7}$$

where $r = \sqrt{x^2+y^2} - R_0$, a = 0.46 m, b = 0.88 m, and R_0 = 3.75 m is the major radius of the magnetic axis.

Typical results of CT orbit calculation obtained by integrating Eq. (4.2.1) with conditions of zero CT electric charge (q = 0) and no CT decay (dm_{CT}/dt = 0) are shown in Fig. 4.2.1. Each of the starting points is located on the grids defined in Fig. 4.1.4. The trajectories are projected on the R' – z' plane or x' – y' plane in Fig. 4.2.1, where x', y', z', and R' are obtained from ρ, θ, and ϕ as

$$x' = R'\cos\phi, \tag{4.2.8}$$

$$y' = R'\sin\phi, \tag{4.2.9}$$

$$z' = r_0\rho\sin\theta, \text{ and} \tag{4.2.10}$$

$$R' = r_0\rho\cos\theta + R_0, \tag{4.2.11}$$

where $r_0 = \sqrt{ab} = 0.6362$ m is the averaged radius of the last closed flux surface. Note that five orbits calculated with different initial velocities are depicted in each of the six plots in Fig. 4.2.1. The direction of LHD magnetic field $\boldsymbol{B}$ is also shown in each plot. When CT has a slower initial velocity, its orbit tends to be bent more, reflecting the helical magnetic field structure of LHD, and it does not reach the plasma center. The starting position of the CT is one of the most important parameters that determines the orbit as seen from the differences of the trajectories depicted in Figs. 4.2.1 (1a) and (1b). The electric charge of CT is also a key parameter as seen from the differences between Figs. 4.2.1 (1a) and (2a). Trajectories of negatively charged CT shown in Fig. 4.2.1 (2a) are affected by the Lorentz force and bent in the direction of $-\boldsymbol{v}\times\boldsymbol{B}$. Positively charged CT and negatively charged CT injected from the same position trace the same trajectory when they have same kinetic energy and the LHD magnetic field is reversed. The top view of the orbits shown in Fig. 4.2.1 (2a) is depicted in Fig. 4.2.1 (2b). Orbits of the CT injected from the L-port are shown in Fig. 4.2.1 (3a) and the top view is shown in Fig. 4.2.1 (3b). Toroidal motion of CT can be seen in Figs. 4.2.1 (2b) and (3b), even though they are not injected tangentially. Indeed, almost all of the CT orbits in a helical magnetic field show a similar three-dimensional motion. The exceptional orbit that shows one-dimensional motion is obtained when the CT is injected from the center of O-port, for example.

From the viewpoint of applying the CT injector for LHD, one should choose the best injection point carefully. Otherwise, it is impossible to achieve the central fueling or the momentum injection. In the next subsection, we compare the differences between orbits that are injected in different manners, to obtain the optimized injection point.

4.2.2. Optimization of the injection point

Since the first purpose of CT injection is to fuel a dense plasma into the core of LHD plasma, the most favorable orbit should pass the plasma center. To inject the momentum effectively,

the orbit should align with the magnetic lines of force. Using such an orbit, one can deposit the CT momentum in the direction parallel to $\boldsymbol{B}$. To find out the optimum orbit, two optimization parameters, ρ_{min} and S_{para}, are defined. Here, ρ_{min} is the normalized radius of the position where the CT orbit is the nearest to the magnetic axis, and S_{para} is defined as the integration of the value $\boldsymbol{v}\cdot\boldsymbol{B}/B$ inside the LHD plasma:

$$S_{para} \equiv \int_{t_1}^{t_2} \frac{\boldsymbol{v}\cdot\boldsymbol{B}}{B} \mathrm{d}t, \tag{4.2.12}$$

where t_1 (t_2) is the time when the CT enters (exits) the LHD plasma. Parameters ρ_{min} and S_{para} are the functions of the starting point (x_0, y_0, z_0) and the initial velocity (v_{0x}, v_{0y}, v_{0z});

$$\rho_{min} = \rho_{min}(x_0, y_0, z_0, v_{0x}, v_{0y}, v_{0z}), \tag{4.2.13}$$

and

$$S_{para} = S_{para}(x_0, y_0, z_0, v_{0x}, v_{0y}, v_{0z}). \tag{4.2.14}$$

The optimized orbit should simultaneously have small ρ_{min} and large S_{para}. The evaluation function f is defined as

$$f \equiv (1 - \rho_{min}) \times 100 + S_{para} \times 50. \tag{4.2.15}$$

This function combines two different properties of the orbit, and one of the purposes of this study is to find out the optimum starting point (x_0, y_0, z_0) to obtain the largest f value. The profiles of ρ_{min} and S_{para} in the x - z plane for the case of CT injected from the O-port are depicted in Fig. 4.2.2. In this calculation, some of the parameters are fixed: y_0 = - 7 m, v_{0x} = v_{0z} = 0 m/s, dm/dt = 0 kg/s, and q = 0 C. Five different cases are considered in the calculation for different initial velocities v_{0y} = 300, 350, 400, 450 and 500 km/s. Then, the results for these five cases are averaged before the f value calculation to eliminate the initial velocity dependence. As can be seen in the figure, the area that has small ρ_{min} is not necessarily the same as that with large S_{para}; ρ_{min} is small at the center, and S_{para} is large at the periphery. This means that the CT injected from the periphery of O-port traces an orbit parallel to the LHD magnetic field, and this effect is also seen in Fig. 4.2.1 (1a) where CT orbits well align with the flux surfaces. The CT injected from near the center of O-port scarcely traces such an aligned trajectory and propagates straight toward the magnetic axis (see Fig. 4.2.1 (1b)). If the purpose of CT injection lies in the center fueling (or the momentum injection), one should choose the center (or the periphery) of O-port. The optimum injection points that have a large

f value are shown in Fig. 4.2.3. Depicted in the figure are the profiles of f in the x - z plane for the case of CT injected from O-port (Fig. 4.2.3 (a)) and that in the x - y plane for the case of CT injected from L-port (Fig. 4.2.3 (b)).

References

[1] W. A. Newcomb, Phys. Fluids B **3**, 1818 (1991).

[2] S. V. Bozhokin, Sov. J. Plasma Phys. **16**, 702 (1990).

[3] L. J. Perkins, S. K. Ho and J. H. Hammer, Nucl. Fusion **28**, 1365 (1988).

[4] C. Xiao, A. Hirose and W. Zawalski, Nucl. Fusion **38**, 249 (1998).

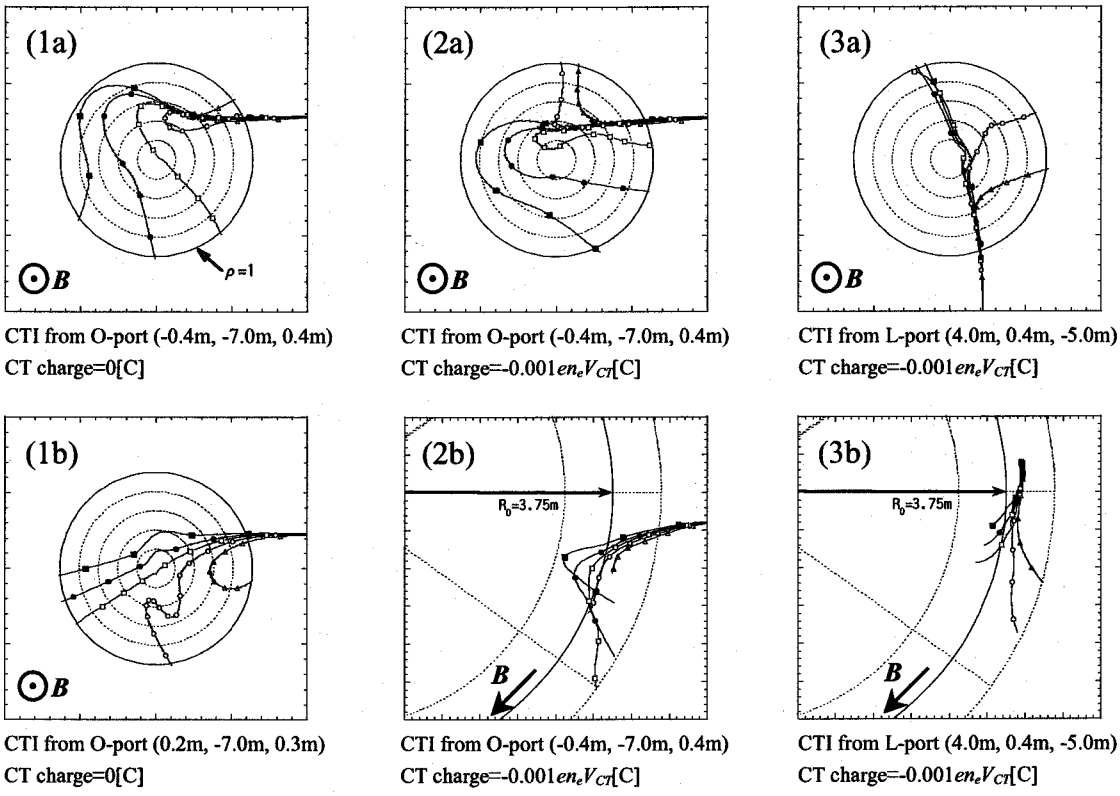

Fig. 4.2.1. CT trajectories projected on the normalized planes ($R' - z'$ plane: (1a), (1b), (2a) and (3a); $x' - y'$ plane: (2b) and (3b). Trajectories calculated with different initial velocities are depicted (250 km/s, open triangles; 300 km/s, open circles; 350 km/s, open squares; 400 km/s, solid circles; and 500 km/s, solid squares). The starting position and CT charge are denoted below each figure.

(a) ρ_{min} profile at O-port

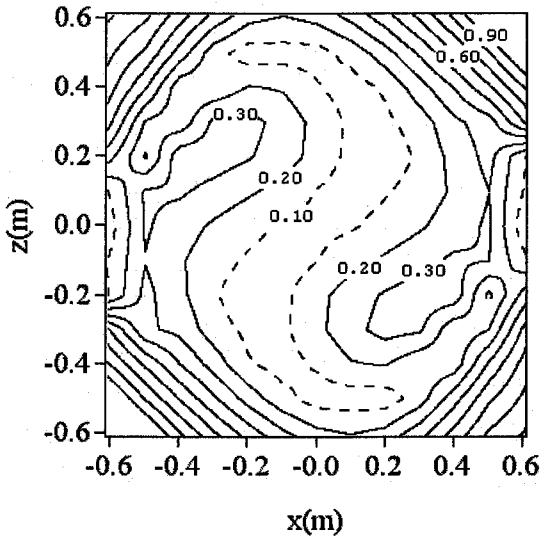

(b) S_{para} profile at O-port

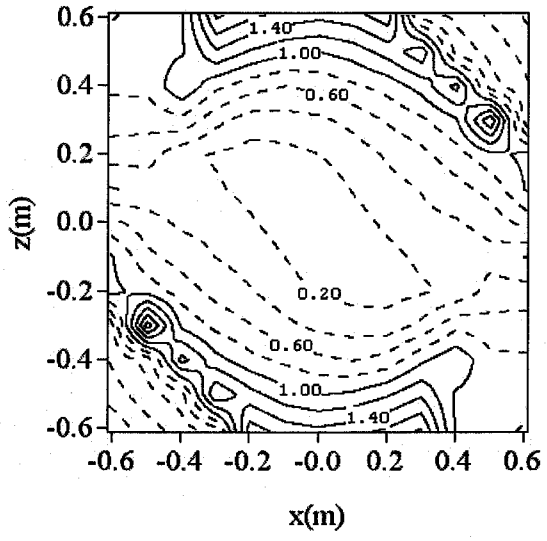

Fig. 4.2.2. (a) ρ_{min} profile and (b) S_{para} profile at O-port (see Fig. 4.1.4). In the area enclosed by broken lines in (a), ρ_{min} is less than 0.1. In the area enclosed by solid lines in (b), S_{para} is larger than 1m. The initial velocity of CT is fixed to 400km/s.

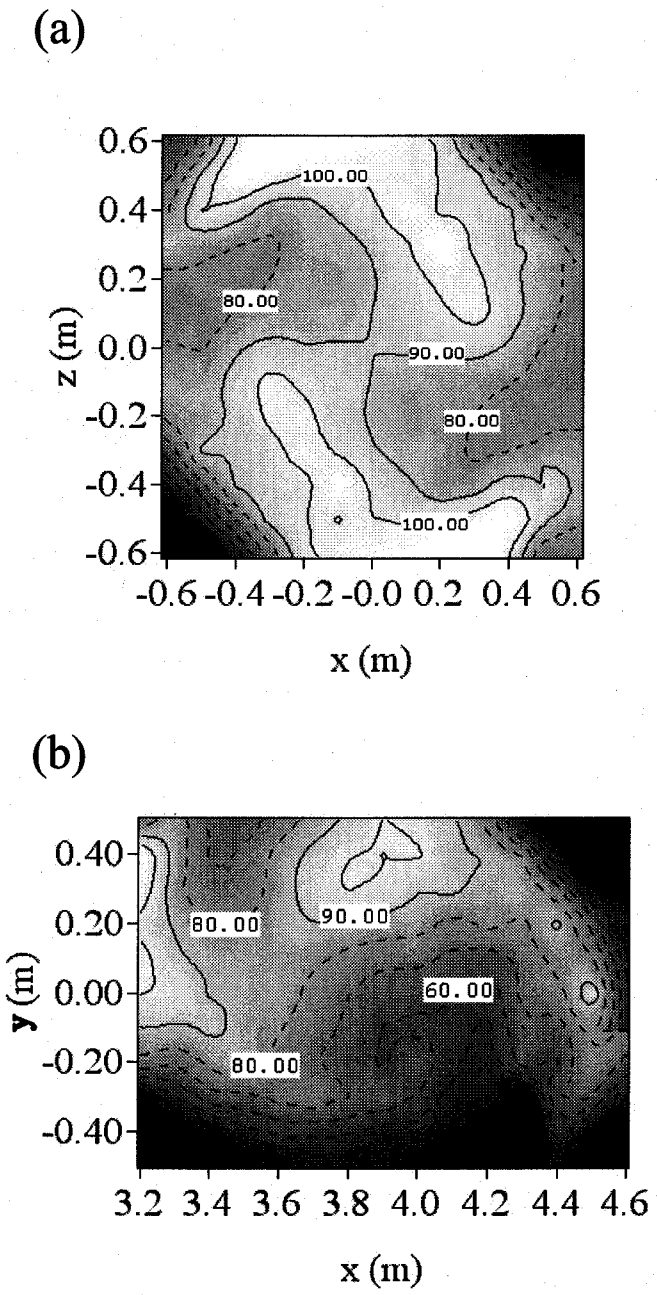

Fig. 4.2.3. Profiles of the parameter f at (a) O-port and (b) L-port. Inside the area enclosed by solid lines, f is larger than 90. This is calculated using Eq. (4.2.15), after averaging ρ_{min} and S_{para} obtained for five different initial velocities (v_0 =300, 350, 400, 450 and 500 km/s).

4.3. Design of the acceleration electrode

4.3.1. Background of the CT injector design

A CT injected into the magnetically confined fusion plasmas suffers from the repelling force due to the gradient of magnetic field strength $\nabla \boldsymbol{B}^2$ [1 - 3]. Therefore, sufficient kinetic energy that is comparable to the magnetic potential energy $V_{CT} B^2 / (2\mu_0)$ (V_{CT}: CT volume) is necessary to inject the CT deep inside the strong magnetic field. CT kinetic energy of more than 3.75 kJ should be supplied to inject a spherical CT of 0.1 m radius into 1.5 T magnetic fields, for instance. The acceleration efficiency ε is defined as the ratio of CT kinetic energy to the bank energy. High efficiency is required to reduce the total cost of a CT injector that largely depends on the capacitor bank energy. It will be shown here that ε is a function of L/L_{ext} (where L is the inductance of the co-axial accelerator, L_{ext} is the external inductance of the acceleration circuit). Large L and/or small L_{ext} are favorable to attain large ε. The ratio R_{out}/R_{in} (R_{in}: the inner electrode radius, and R_{out}: the outer electrode radius) and the electrode length l determine L. When R_{out}/R_{in} and/or l are large, L is also large.

The lifetime of a CT, τ_{CT}, is one of the important parameters especially in the large devices like LHD. As the distance from the injection port to the main plasma is long, the time-of-flight is expected to be long comparable to τ_{CT} of a usual CT in these large devices. For the case of dense and low-temperature CT, τ_{CT} is determined by the resistive decay as $\tau_{CT} \sim \mu_0 / (\lambda^2 \eta)$, where η is the Spitzer resistivity, λ is the Taylor eigenvalue ($\nabla \times \boldsymbol{B} = \lambda \boldsymbol{B}$ in the force-free spheromak) and $1/\lambda = a_{CT} / 4.493$ (a_{CT}: the radius of CT sphere) in the spherical geometry [4, 5]. Typical electron temperature of a spheromak is a few tenth of eV [6, 7] and this gives η of the order of 10 $\mu\Omega \cdot$ m. Accordingly, τ_{CT} is 50 μsec in the case of $a_{CT} = 0.1$ m, for example. Because α is determined by the CT radius that cannot exceed the main plasma radius, it is efficient to heat up the CT and increase the electron temperature to extend τ_{CT}.

The adiabatic compression is an effective method to improve the CT parameters such as the magnetic field strength, the density and the temperature. To carry out the adiabatic compression, it is necessary to keep proper relations between the CT compression time τ_{comp} and other time-constants such as collision time, energy confinement time, and the time of Alfvén wave transmission across the CT radius, τ_A [8 - 11]. For example, $\tau_A \ll \tau_{comp}$ is required to compress the CT self-similarly without generating shock waves. Although the typical CT injectors have been equipped with the compression cones after the straight co-axial electrodes,

the condition $\tau_A \ll \tau_{comp}$ has not been achieved due to insufficient length of the cones. In this study, a conical shaped accelerator is proposed to extend τ_{comp} as long as the CT acceleration time, τ_{acc}. Changes in CT parameters, such as the magnetic field strength, the temperature, and the density, before and after the compression are calculated assuming the adiabatic condition.

As will be discussed, one can obtain the high acceleration efficiency when the ratio R_{out}/R_{in} is large enough. Large R_{out}/R_{in} means relatively small R_{in} that results in the comparatively strong magnetic field around the inner-electrode. If the acceleration current I_{acc} is extremely large, the current blows out CT and normal acceleration is hardly achieved. Experimentally, the threshold to avoid this "blowby" phenomenon is given by $B_{CT} > B_{acc}$, where B_{CT} is CT magnetic field and B_{acc} is the magnetic field generated by I_{acc} [12 – 14]. Therefore, B_{CT}, which is mainly determined by the bias magnetic field, should be larger than B_{acc}, which is large when R_{in} is small. On the other hand, smaller bias magnetic field is favorable because that requires the less formation current, which should be large enough to push the current sheet out of the formation electrode, and mitigates the capacitor banks for CT formation. The minimum CT magnetic field to avoid the blowby phenomenon is derived through the optimization of the acceleration part.

Nine parameters listed in Table 4.3.1 are used to describe the CT acceleration electrodes. This acceleration part has conical shape as shown in Fig. 4.3.1. Three parameters (R_{in1}, C_{acc}, and E_{acc}) are mainly discussed in this paper while other six parameters are determined as below. The outer electrode radius at the exit of acceleration part R_{out2} determines the radius of an injected CT. Small CT is favorable because the perturbation caused by CT injection should be smaller and localized. In our case, R_{out2} (= 0.07 m) is determined to be about one tenth of the typical averaged minor radius of LHD. Total amount of particles N_{CT} and the CT lifetime τ_{CT} are related to the size of CT at the entrance of the acceleration part that is defined as R_{out1}. Although large R_{out1} is favorable to increase both of N_{CT} and τ_{CT}, extremely large R_{out1} results in an unfavorably large size CT injector. In the present case, R_{out1} (= 0.17 m) is more than twice larger than R_{out2}, while it allows the use of standard ICF flange (ICF406). Aspect ratio of CT at the exit of the acceleration part A_2 is determined by R_{out2} and R_{in2} as $A_2 \equiv R_2/a_2$ ($a_2 \equiv (R_{out2}-R_{in2})/2$, and $R_2 \equiv R_{in2}+a_2$). Because the aspect ratio just after the exit of the acceleration part is one, A_2 should be as small as possible to avoid the large modification of CT shape. Therefore, R_{in2} = 0.02 m is adopted. Note that extremely small R_{in2} might not be chosen because the Joule heating by the acceleration current would melt down the electrode. The external inductance L_{ext} and the circuit resistance R_c

should be as small as possible to maximize the acceleration efficiency ε as will be discussed in the next section. The length of the acceleration part l should be long enough to have large L that results in large ε and to realize slow and self-similar compression. Extremely large l might increase the impurity level contained in a CT and enlarge the size of CT injector, on the other hand. In this study, l = 3.2 m is adopted. Other cases with l = 0.8 m and l = 1.6 m are also examined in sections 4.3.3 and 4.3.4. As will be mentioned there, l = 0.8 m is adopted in our first CT injector named SPICA.

4.3.2. Point-model and acceleration efficiency ε

One-dimensional motion of a CT in the acceleration electrode is described by the point-model introduced by Hammer et al. in ref. 12. Although their model assumes no resistivity in the acceleration circuit, it agrees well with experimental results. The point model with consideration of circuit resistivity R_c consists of three equations below,

$$L_t = L_{ext} + L, \tag{4.3.1}$$

$$\frac{d^2 I_{acc} L_t}{dt^2} + R_c \frac{dI_{acc}}{dt} + \frac{I_{acc}}{C_{acc}} = 0, \tag{4.3.2}$$

$$m_{CT} \frac{d^2 x}{dt^2} = \frac{1}{2} L' I_{acc}^{\ 2} - F_{drag}, \tag{4.3.3}$$

where $L = \int_0^x L' dx$ ($L' = \mu_0/(2\pi) \ln(R_{out}(x)/R_{in}(x))$, and $0 \le x \le l$) is the inductance of the co-axial electrode, L_t is the total inductance of the acceleration circuit, I_{acc} is the circuit current, C_{acc} is the capacitance of the acceleration bank, m_{CT} is the CT mass, and F_{drag} is the drag force. In this study, F_{drag} = 0 is assumed to be negligibly small as in ref. 12. Time dependence of R_c is neglected in Eq. (4.3.2), although it consists of time-dependent component such as plasma resistivity and electrode resistivity that depends on the CT position in the electrode. Since the plasma resistivity of the order of 10^{-4} Ω is negligible in our case, this approximation is valid as long as the electrode resistivity (of the order of 10^{-3} Ω) is smaller enough than the other circuit resistivity. In a general straight co-axial electrode, the inner-electrode radius R_{in} and the outer-electrode radius R_{out} are constant and $L_t = L_{ext} + L'x$. In the case of the conical accelerator, $R_{in}(x) = R_{in1} + (R_{in2} - R_{in1}) \cdot x/l$ and $R_{out}(x) = R_{out1} + (R_{out2} - R_{out1}) \cdot x/l$. Using the expressions in Eqs (4.3.1) - (4.3.3), the CT kinetic energy E_{CT} is given by

$m_{CT}(dx/dt)^2/2$ and the acceleration bank energy E_{acc} is given by $C_{acc}V_{acc}^2/2$, where V_{acc} is the bank voltage.

The fourth-order Runge-Kutta method is used to solve Eqs. (4.3.1) - (4.3.3). Figure 4.3.2 shows the calculation results for a straight co-axial electrode with $R_{out}/R_{in} = 2$ and $l = 3.2$ m. Three different cases are calculated while changing C_{acc} and R_c. As seen in the differences between Fig. 4.3.2 (a) and Fig. 4.3.2 (b), CT obtains less kinetic energy when R_c is not zero. The energy loss due to R_c occurs mainly in the current increasing phase (before $t \sim 5$ μsec) and then E_{CT} gradually increases. In other words, the transfer of the energy from the acceleration bank (E_{acc}) to the CT (E_{CT}) occurs mainly after the current peaks. Therefore the current peak should be obtained before the CT exits the acceleration electrode and smaller C_{acc} should be used because the oscillation frequency of this LCR circuit is proportional to $1/C_{acc}^{1/2}$. Note that extremely small C_{acc} results in the large acceleration bank voltage V_{acc}, which might be not realistic, to obtain the same bank energy as in moderate C_{acc} case. Moreover, too small C_{acc} results in the oscillation of the current as shown in Fig. 4.3.2 (c) and E_{CT} is not necessarily larger than that obtained with moderate C_{acc} (as in Fig. 4.3.2 (b)).

The acceleration efficiency ε as a function of C_{acc} is calculated using different values of R_c and E_{acc}, where the other parameters such as L_{ext} and the electrode shape L' are fixed. The results are shown in Fig. 4.3.3. When $R_c = 0$ Ω, the maximum of ε (ε_{max}) does not depend on E_{acc}. Finite R_c reduces ε_{max} and the reduction rate is larger when E_{acc} is smaller. Although R_c degrades ε_{max}, the optimum C_{acc} that gives ε_{max} is not affected by R_c. Coulomb numbers of the bank $Q = C_{acc}V_{acc}$ calculated for the optimum cases are also constant, and $Q \sim 2.4$ C in the case shown in Fig. 4.3.3. These observations mean that once an electrode is designed and assembled, the acceleration efficiency that can be achieved with the electrode is already determined, and the optimum C_{acc} for each E_{acc} should be adopted to attain the largest ε.

It is possible to show that ε_{max} does not depend on E_{acc} but on the ratio of the electrode inductance to the external inductance. Let us consider a general LCR circuit without external power supplies. The circuit equation is given by

$$L\frac{dI}{dt} + RI + \frac{Q}{C} = 0. \tag{4.3.4}$$

Zero-resistivity condition gives the harmonic oscillation with the eigenfrequency $\omega_0 = 1/\sqrt{LC}$ as the solution. When the resistivity is finite, the solution is the damped oscillation where the amplitude decreases with time as $\exp(-\gamma t)$ ($\gamma = R/(2L)$). In the present

case, dL/dt is not zero and the circuit equation is given by

$$\frac{d(LI)}{dt}+RI+\frac{Q}{C}=L\frac{dI}{dt}+\left(\frac{dL}{dt}+R\right)I+\frac{Q}{C}=0, \tag{4.3.5}$$

instead of Eq. (4.3.4). Note that Eq. (4.3.2) is obtained by differentiating Eq. (4.3.5) with t. It can be seen in Eq. (4.3.5) that dL/dt plays the same role as R, and therefore gives the damped oscillation as the solution even if $R = 0$. Here let L and dL/dt be fixed to evaluate the order of damping time constant γ. These are not constant in practical situation since L is the function of the current sheet position x in the electrode and dL/dt depends on the velocity $v = dx/dt$. Using fixed parameters, *i.e.*, $L^* = L_{ext} + L/2$ and $dL^*/dt = L / \tau_{acc}$, the approximated damping time constant γ^* for zero-resistivity is given by

$$\gamma^*=\frac{dL^*/dt}{2L^*}=\frac{L}{2L_{ext}+L}\frac{1}{\tau_{acc}}=\frac{m}{2+m}\frac{1}{\tau_{acc}}, \tag{4.3.6}$$

where $m \equiv L/L_{ext}$. The energy of the circuit decreases as $(\exp(-\gamma^* t))^2$ and the lost energy should be equal to the CT kinetic energy to fulfill the energy conservation law. Therefore, the approximated CT kinetic energy E_{CT}^* is given by

$$E_{CT}^*=E_{acc}(1-\exp(-2\gamma^* t)). \tag{4.3.7}$$

The ratio of E_{CT}^* with $t = \tau_{acc}$ to the bank energy E_{acc} gives the approximated efficiency ε^*;

$$\varepsilon^*=\frac{E_{CT}^*}{E_{acc}}=1-\exp(-2\gamma^*\tau_{acc})=1-\exp\left(-\frac{m}{2+m}\right). \tag{4.3.8}$$

This function is shown in Fig. 4.3.4 with a solid line. The maximum efficiencies calculated using the fourth-order Runge-Kutta method with different parameters are also plotted in the figure. It can be seen that ε^* approximates ε_{max} well. As seen in Fig. 4.3.4, ε_{max} increases with m. Therefore, large L and/or small L_{ext} are the indispensable conditions for a high performance CT injector.

4.3.3. Design of the formation electrode

The adiabatic compression heating using a conical accelerator might be effective to increase the CT density and/or the CT magnetic field. The adiabatic conditions τ_{ee}, τ_{ii}, τ_A « τ_{comp} « τ_E,

τ_{CT} , should be fulfilled to realize compression heating, where τ_{ee} and τ_{ii} are electron-electron and ion-ion collision time, respectively, and τ_E is energy confinement time. The relations between these time constants, which are calculated using typical parameters described in Table 4.1.1, are depicted in Fig. 4.3.5. Although τ_E is unknown, τ_{comp} should be sufficiently larger than τ_A, because $\tau_A \ll \tau_{comp}$ is needed to realize the self-similar compression. The largest τ_{comp} is obtained when the length of the compression cone and that of the acceleration electrode are the same and $\tau_{comp} = \tau_{acc}$ as is the case of the conical accelerator. Here let us calculate the compression parameters assuming the adiabatic condition. Each of parameters of general toroidal plasma depends on the CT minor radius a and the CT major radius R as listed in Table 4.3.2. The relations in Table 4.3.2 are obtained assuming the adiabatic condition $T \cdot n^{1-5/3} = constant$, and $B_p \sim B_t$. The increment factors are calculated and shown in Fig. 4.3.6. The temperature (density) increases more than four (eight) times after the compression when R_{in1} is smaller than the half of R_{out1} (= 0.17 m). The large plasma pressure might cause some pressure driven instability on the other hand. In the present case, the pressure increases more than thirty times when $R_{in1} < R_{out1}/2$. However, the increase in the magnetic field pressure helps to suppress the increase of plasma beta lower than a factor of three even in that case. The CT magnetic field B_{CT} should be larger than the magnetic field B_{acc} generated by the acceleration current, to avoid the blowby. In the case of a conical accelerator, B_{CT} increases during acceleration when the compression is effective. The least magnetic field strength at the entrance of conical accelerator, B_{01}, should be determined using the condition that B_{CT} is always larger than B_{acc} during the acceleration phase.

To optimize the electrode design, C_{acc} is scanned to obtain the largest ε for each R_{in1} where l = 3.2 m, R_{out1} = 0.17 m, R_{out2} = 0.07 m, R_{in2} = 0.02 m, and E_{acc} = 75 kJ are fixed. Three different cases of (L_{ext}, R_c) = (0.2 μH, 0 Ω), (0.5 μH, 0 Ω), and (0.5 μH, 0.03 Ω) are calculated and the optimum values of C_{acc}, V_{acc}, and ε are plotted as functions of R_{in1} in Fig. 4.3.7. The least B_{01} in each case are also shown in the figure. The maximum ε increases as R_{in1} decreases, and in this sense, R_{in1} should be as small as possible. On the other hand, the optimum V_{acc} is large when R_{in1} is small. One can determine the optimum R_{in1} using Fig. 4.3.7. First, the target CT kinetic energy and ε determine the bank energy. In our case, $E_{CT} \geqq 15$ kJ should be achieved and more than 38 % of ε is expected for $R_{in1} \leq 0.07$ m. Therefore, E_{acc} = 40 kJ is enough to obtain the target CT. Note that ε is not affected by E_{acc} when $R_c = 0$, as already mentioned in section 4.3.3. Using the fact that the optimum $Q = C_{acc}V_{acc}$ is also unchanged by E_{acc}, the relation $E_{acc} \propto V_{acc}$ is obtained at the optimum condition. Thus V_{acc}

in Fig. 4.3.7 can be reduced to about half because E_{acc} = 75 kJ is used to obtain the figure. When V_{acc} is limited to ~ 40 kV, for instance, R_{in1} = 0.07 m can be chosen with E_{acc} = 42.4 kJ, and the achievable E_{CT} is 14.5 kJ in that case (L_{ext} = 0.5 μH and R_c = 0.03 Ω). One should note that the maximum ε slightly decreases with E_{acc} when R_c is not negligible (see Fig. 4.3.3). The least B_{01} for R_{in1} = 0.07 m is 0.62 T in Fig. 4.3.7. This can be also reduced if small E_{acc} is adopted. In the case of E_{acc} = 42.4 kJ, B_{01} is calculated to be 0.46 T.

Three types of conical accelerator are considered. The difference between them is the length of the acceleration electrode l. Although the long electrode of l = 3.2 m has the merit of large efficiency, both of the construction cost and the technological difficulty increase. Therefore, other two cases with l = 0.8 m and l = 1.6 m are also optimized according to the process already mentioned above for l = 3.2 m. The optimized parameters are listed in Table 4.3.4. The available voltage for V_{acc} is limited to 40 kV or 20 kV in this series of optimization. The moderate length electrode of l = 1.6 m is still usable since the achievable E_{CT} is over 7 kJ which is enough for CT injection into 1.5 T LHD magnetic field. The shortest length electrode of l = 0.8 m can achieve only 3.4 kJ of E_{CT} in the optimum condition, and it is also difficult to fulfill the adiabatic condition because of the small τ_{acc} (= τ_{comp}).

Up to this point, the CT mass is fixed to 0.1 mg. Here, let us examine the dependence of ε on m_{CT}. Scanning m_{CT} for the case of short acceleration electrode of l = 0.8 m, Fig. 4.3.8 is obtained. Two cases with V_{acc} = 20 kV and V_{acc} = 40 kV are calculated using optimized parameters listed in Table 4.3.4. As can be seen, there is an optimum m_{CT} that maximizes ε for each V_{acc}. The CT mass might be controlled by the fuel-gas amount injected into the formation part. In the case of V_{acc} = 40 kV, the maximum ε of 16.4 % is obtained at m_{CT} = 0.06 mg, which is slightly larger than that in Table 4.3.4. Larger ε and E_{CT} can be also achieved by reducing R_c and L_{ext}, or increasing V_{acc}.

References

[1] J. Miyazawa, H. Yamada and O. Motojima, "Possibility of Profile Control using Compact Toroid Injection on Large Helical Device", Jpn. J. Appl. Phys. **37**, 6620 (1998).

[2] S. V. Bozhokin, Sov. J. Plasma Phys. **16**, 702 (1990).

[3] C. Xiao, A. Hirose and W. Zawalski, Nucl. Fusion **38**, 249 (1998).

[4] M. N. Rosenbruth and M. N. Bussac, Nucl. Fusion **19**, 489 (1979).

[5] L. J. Perkins, S. K. Ho and J. H. Hammer, Nucl. Fusion **28**, 1365 (1988).

[6] Y. Ono, R. A. Ellis, Jr., A. C. Janos, F. M. Levinton, R. M. Mayo, R. W. Motley, Y. Ueda and M. Yamada, Phys. Rev. Lett. **61**, 2847 (1988).

[7] T. R. Jarboe, F. J. Wysocki, J. C. Fernández, I. Henins and G. J. Marklin, Phys. Fluids B **2**, 1342 (1990).

[8] V. E. Golant, *Proc. of 11th European Conf. on Plasma Phys. and Controlled Fusion,* Aachen (1983), Plasma Phys. and Controlled Fusion **26**, 77 (1984).

[9] K. Bol, R. A. Ellis *et al.*, Phys. Rev. Letters **29**, 1495 (1972).

[10] K. Bol, J. L. Cecchi *et al.*, *Proc. of 5th Int. Conf. on Plasma Phys. and Controlled Nucl. Fusion Research,* Tokyo (1974), Vol. 1, p.83.

[11] R. A. Ellis, H. P. Eubank *et al.*, Nucl. Fusion **16**, 524 (1976).

[12] J. H. Hammer, C. W. Hartman, J. L. Eddleman, H. S. McLean, Phys. Rev. Letters **61**, 2843 (1988).

[13] J. H. Hammer, J. L. Eddleman, C. W. Hartman, H. S. McLean and A. W. Molvik, Phys. Fluids B **3**, 2236 (1991).

[14] J. Eddleman *et al.*, "Final Report on the LLNL Compact Torus Acceleration Project", UCRL-ID-120238, Lawrence Livermore National Laboratory (Mar. 1995).

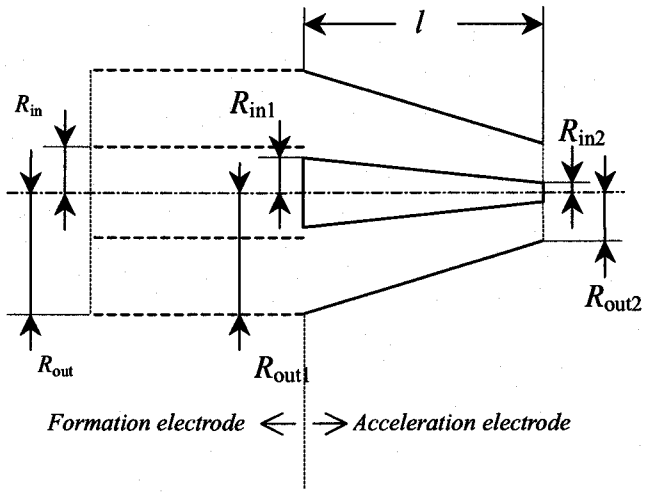

Fig. 4.3.1. Geometry of the conical accelerator. CT enters from the left-hand-side and exits to the right-hand-side. CT formation electrode is drawn by broken lines.

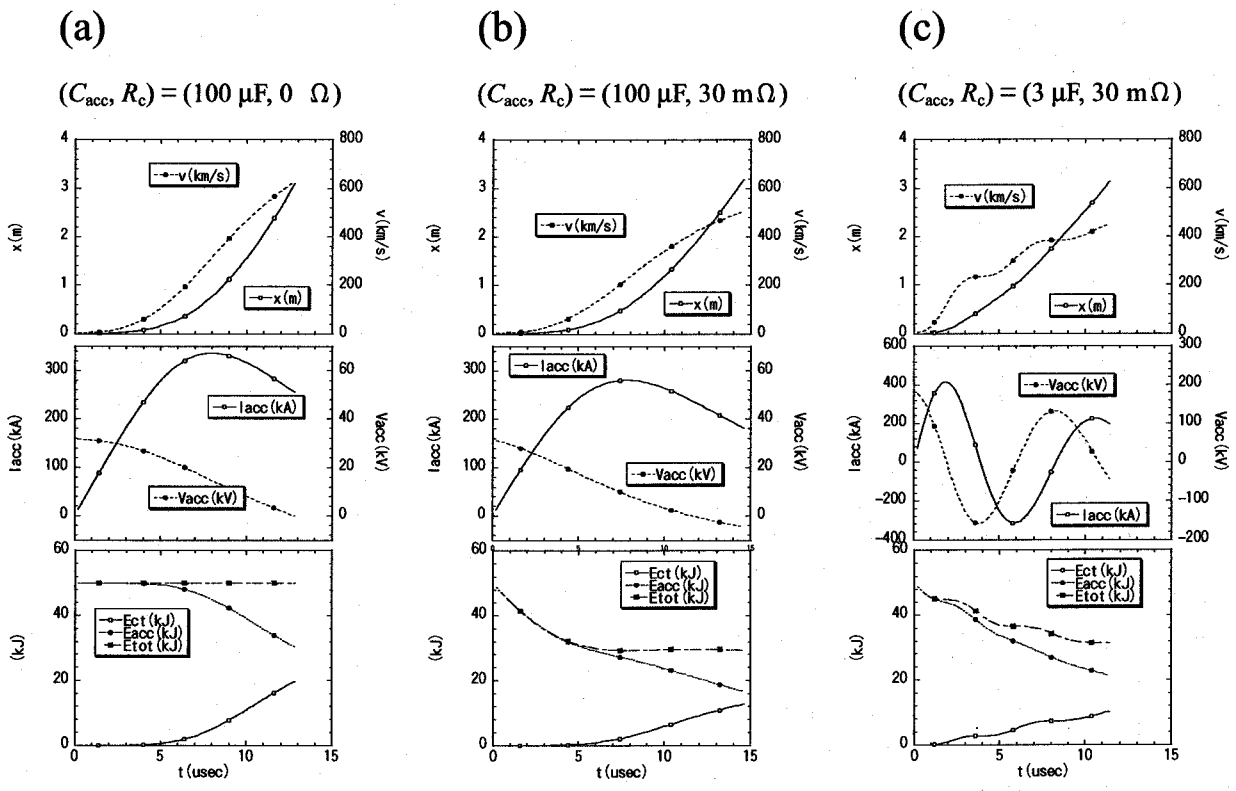

Fig. 4.3.2. Calculated waveforms of CT position x and CT velocity v (top), acceleration current I_{acc} and acceleration voltage V_{acc} (middle), CT kinetic energy E_{CT}, circuit energy E_{acc} and the total energy $E_{tot} = E_{CT} + E_{acc}$ (bottom). Assumed C_{acc} and R_c are indicated on the top of each column.

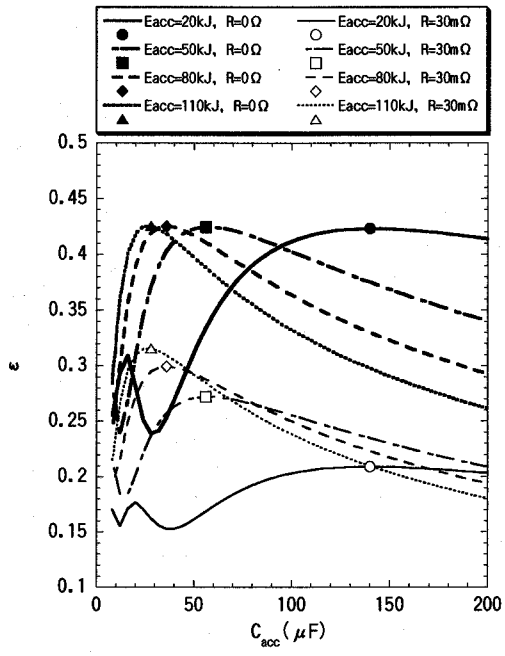

Fig. 4.3.3. Acceleration efficiency as a function of C_{acc}. Straight co-axial electrode geometry with $l = 3.2$ m, $R_{out}/R_{in} = 2$, $m_{CT} = 0.1$ mg, $F_{drag} = 0$ N, $v_0 = 5$ km/s and $L_{ext} = 0.5$ μH are used in this calculation, where E_{acc} and R_c are scanned as indicated on the top of the figure. The maximum efficiencies are marked with symbols.

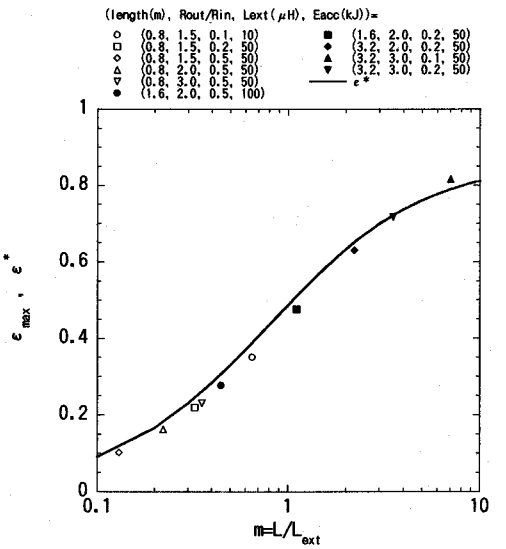

Fig. 4.3.4. The maximum efficiencies calculated for various parameter sets and the approximated efficiency ε^* (solid line). Straight co-axial electrode geometry, $m_{CT} = 0.1$ mg, $F_{drag} = 0$ N, $v_0 = 5$ km/s are fixed throughout the optimization.

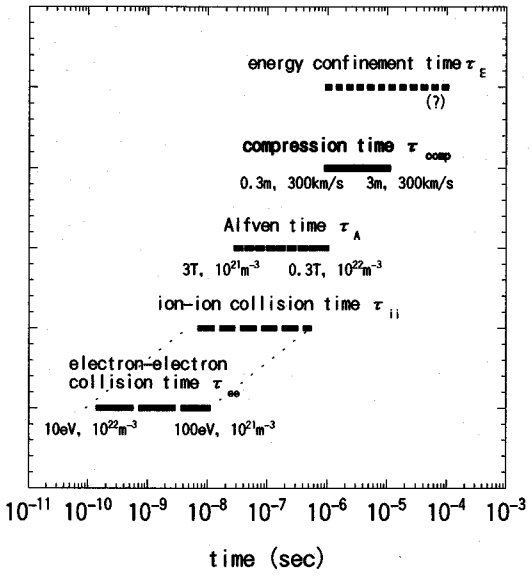

Fig. 4.3.5. Characteristic time scales of typical CTs and accelerators.

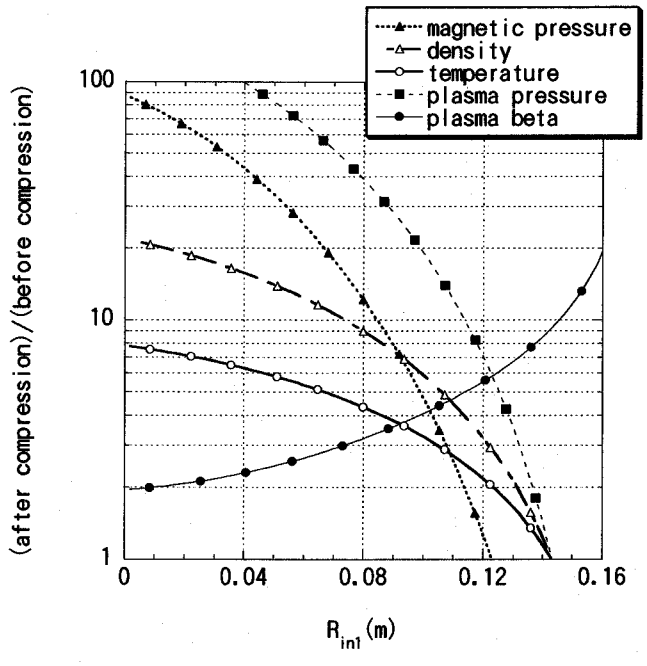

Fig. 4.3.6. Compression parameters of adiabaticaly compressed toroidal plasmas, where R_{out1} = 0.17 m, R_{out2} = 0.07 m and R_{in2} = 0.02 m are fixed. Adiabatic condition of $T \cdot n^{1-5/3}$ = *constant* and $B_p \sim B_t$ are assumed.

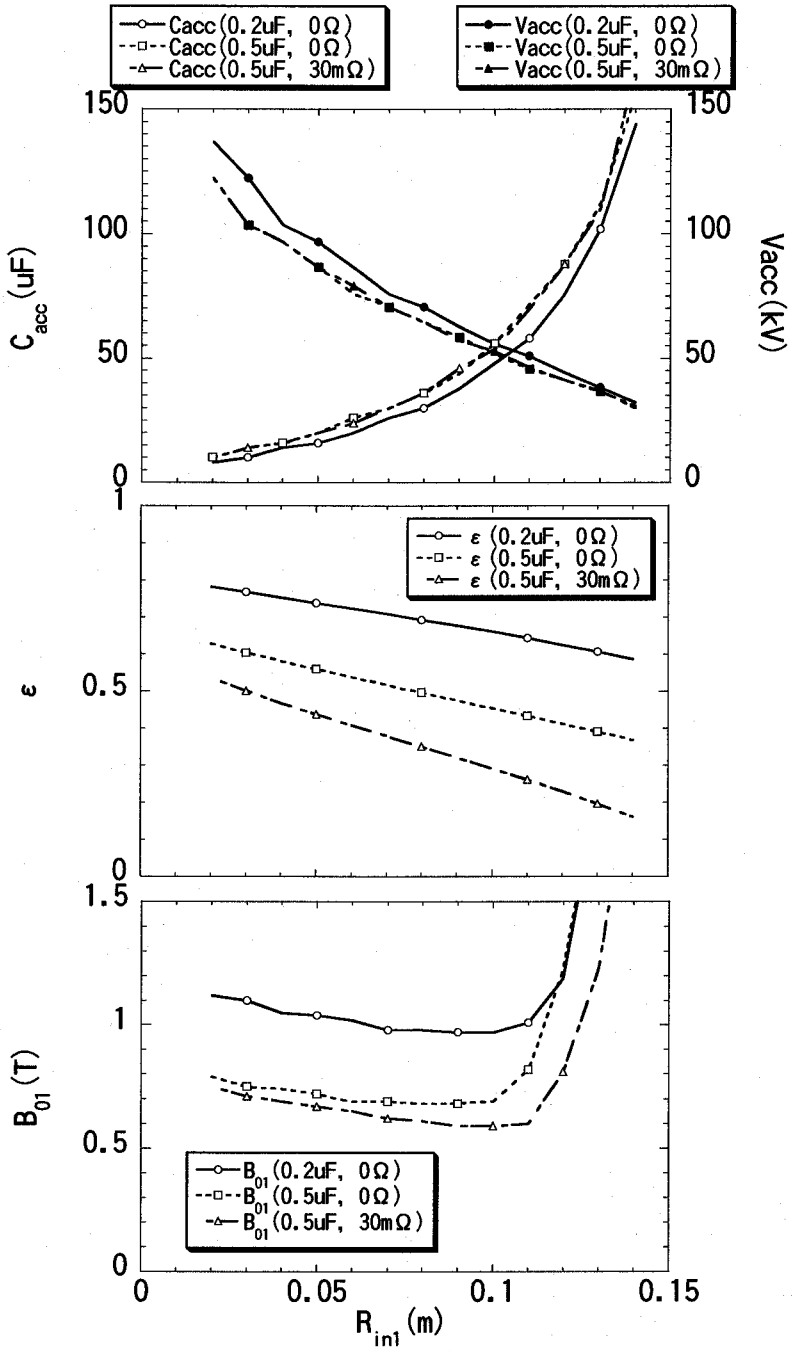

Fig. 4.3.7. Optimized parameters in three different cases. The optimum C_{acc} and V_{acc} (top), the acceleration efficiency ε (middle), and the least magnetic field strength at the entrance of the acceleration part B_{01} (bottom) are shown as functions of R_{in1}. Assumed R_c and L_{ext} are indicated in each plot. The other parameters such as E_{acc} = 75 kJ, l = 3.2 m, R_{out1} = 0.17 m, R_{out2} = 0.07 m, R_{in2} = 0.02 m, m_{CT} = 0.1 mg, F_{drag} = 0 N, v_0 = 1 m/s are fixed throughout this optimization.

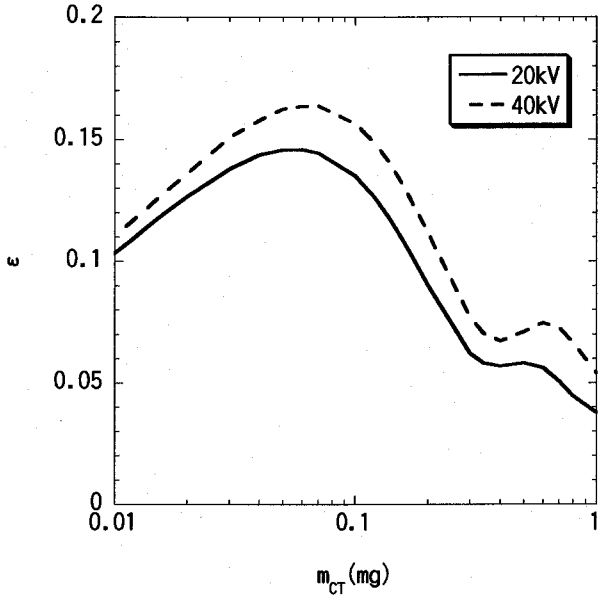

Fig. 4.3.8. The mass dependence of acceleration efficiency ε of the CT injector with short acceleration electrode of l = 0.8 m. Two cases with V_{acc} = 20 kV and V_{acc} = 40 kV are shown. The optimum parameters listed in Table 4.3.3 are used in the calculation.

Table 4.3.1. Main parameters used to design the acceleration electrode.

Inner radius at the entrance, R_{in1} (m)	*to be optimized.*
Outer radius at the entrance, R_{out1} (m)	0.17
Inner radius at the exit, R_{in2} (m)	0.02
Outer radius at the exit, R_{out2} (m)	0.07
Electrode length, ℓ (m)	3.2 (/ 1.6 / 0.8)
Resistance of the circuit, R_c (Ω)	< 0.03
Capacitance of the bank, C_{acc} (F)	*to be optimized.*
Stored energy of the bank, E_{acc} (J)	*to be optimized.*
External inductance, L_{ext} (H)	$< 5 \times 10^{-7}$

Table 4.3.2. Adiabaticaly compressed parameters as functions of the minor radius a and the major radius R of toroidal plasma. The adiabatic condition $T \cdot n^{1-5/3} =$ *constant* and $B_t \sim B_p$ are assumed.

Toroidal magnetic field strength, B_t	$\propto a^{-2}$
Poloidal magnetic field strength, B_p	$\propto a^{-1} R^{-1}$
Plasma volume, V	$\propto a^2 R$
Plasma density, n	$\propto a^{-2} R^{-1}$
Plasma temperature, T	$\propto a^{-4/3} R^{-2/3}$
Plasma pressure, p	$\propto a^{-10/3} R^{-5/3}$
Averaged magnetic pressure, $\propto B^2$	$\propto a^{-2}(a^{-2} + R^{-2})$
Plasma beta, β	$\propto a^{-4/3} R^{-5/3} (a^{-2}+R^{-2})^{-1}$

Table 4.3.3. Optimized parameters for different acceleration electrode lengths and voltage limits. The arrow (←) denotes that the parameter is identical to that in the left column.

ℓ (m)	0.8	0.8	1.6	1.6	3.2	3.2
Assumed parameters						
R_{in1} (m)	0.07	←	←	←	←	←
R_{out1} (m)	0.17	←	←	←	←	←
R_{in2} (m)	0.02	←	←	←	←	←
R_{out2} (m)	0.07	←	←	←	←	←
L (μH)	0.16	←	0.32	←	0.64	←
L_{ext} (μH)	0.5	←	←	←	←	←
R_c (mΩ)	30	←	←	←	←	←
m_{CT} (mg)	0.1	←	←	←	←	←
v_0 (m/s)	1.0	←	←	←	←	←
V_{acc} (kV)	20	40	20	40	20	40
Optimized parameters						
E_{acc} (kJ)	11.0	21.9	15.5	31.0	21.2	42.4
C_{acc} (μF)	54.8	27.4	77.5	38.7	106	53.0
I_{acc} (kA)	158	235	175	261	189	282
B_{01} (T)	0.25	0.37	0.28	0.41	0.31	0.46
τ_{acc} (μs)	11.7	8.03	14.7	9.98	19.0	12.8
ε	0.135	0.157	0.207	0.244	0.286	0.342
E_{CT} (kJ)	1.49	3.43	3.20	7.56	6.07	14.5

4.4. Experimental results on SPICA

4.4.1. Apparatus

The CT injector named SPICA (SPheromak Injector using Conical Accelerator) was successfully assembled on March 1999. Schematic view and the photograph of SPICA are shown in Fig. 4.4.1. SPICA is a co-axial plasma gun that has two electrically isolated inner electrodes to enable CT generation and CT acceleration on each electrode, which is called two-stage acceleration. A conical acceleration electrode is adopted to realize slow compression of a CT. During the initial experiments, short acceleration electrode of 0.8 m long was used to demonstrate the CT formation and acceleration. A small sized vacuum chamber of 0.15 m diameter and 2 m long (Fig. 4.4.2 (a)) was used at the earlier phase of the initial experiment, and it was then replaced with the larger vacuum chamber of 0.32 m diameter and 3.6 m long (Fig. 4.4.2 (b)). On Oct. 2001, the reconstruction of SPICA has been started to extend the acceleration electrode, and finished on Feb. 2002. Schematic of SPICA after the extension is shown in Fig. 4.4.3. The length of the outer-electrode was extended to 2.6 m. The inner radius of the outer electrode changes from 0.172 m to 0.075 m to compress the CT during the acceleration. To extend the inner electrode, a conical extension electrode is welded on the tip. In a part of the two-stage acceleration experiments, a drift tube was installed inside the large test chamber, as shown in Fig. 4.4.3. The length and the inner-radius of the drift tube are 1.95 m and 0.08 m, respectively. The influence of the drift tube on CT transfer was examined in the two-stage acceleration experiments with or without drift tube.

On June 2000, the CT generation bank of 20 kV of the maximum charging voltage and 40 kJ of the maximum stored energy was installed. The capacitance of this bank is 200 μF, and the maximum current is 300 kA. The CT acceleration bank of 40 kV – 96 kJ (120 μF of the capacitance and 400 kA of the maximum current) was also installed on April 2001, to enable the two-stage acceleration. The capacitance of this bank is similar to the optimum value of 106 μF, for the acceleration electrode of 3.2 m long with 20 kV charging voltage (see Table 4.3.3 in section 4.3). Note that although the maximum charging voltage of the acceleration bank is 40 kV, it is supposed to use the lower (and therefore safer) charging voltage in the test experiments more frequently.

SPICA is equipped with some characteristic parts that cannot be seen on the other CT injectors, such as the conical electrode, the expansion chamber for strong differential pumping, and fast piezo-valves for gas injection into the formation part. The expansion chamber is

necessary to pump out the neutral gas that is not ionized in the injector. The inflow of neutral gas into the main plasma is not favorable because this makes it difficult to see the fueling effect only by a CT. SPICA is equipped with a turbo molecular pump of pumping rate 1 m^3/s. Another turbo molecular pump of pumping rate 0.2 m^3/s is also equipped on the acceleration electrode flange to pump the volume between the two inner-electrodes of formation and acceleration. The working gas is introduced through the fast piezo-valves, of which the time for full close to full open (and vice versa) is less than 10^{-3} s. Stable flow rate and less mechanical shocks are the merits of the piezo-valve compared to the solenoid-valve. The biasing coil, which magnetizes the CT, is set around the CT formation electrode. This coil consists of copper conductor of 4 mm × 9 mm cross-section that is wound 201 turns. A DC bank supplies the biasing coil 300 A of DC current at its maximum.

Two Rogowsky coils wound around the insulators of the formation (generation) electrode and the acceleration electrode are used to measure the discharge currents of I_{gen} and I_{acc}, respectively. Fast Si photo-diodes measure the visible light to trace the CT motion. The poloidal (axially directed) magnetic field, B_p, and/or the toroidal magnetic field, B_t, are measured by the inserted magnetic probes. The line-averaged electron density, $\bar{n}_e$, is measured by the He-Ne interferometer. The full width at the half maximum (FWHM) of $\bar{n}_e$ is used as the CT length, in this study.

4.4.2. CT formation test in the initial experiment

In the initial experiment of SPICA with a short acceleration electrode of 0.8 m long, the one-stage operation was adopted. In this operation, CT was generated and accelerated continuously by the CT generation bank. CT was injected to the test chambers shown in Fig. 4.4.2. Typical waveforms in the initial experiment are shown in Fig. 4.4.4. The electron density $\bar{n}_e$ measured by a He-Ne laser interferometer reaches to the order of 10^{21} m^{-3} and its waveform resembles the magnetic field signal measured at the same location, suggesting that the high density CT is magnetized. The trajectory measured by magnetic signals at various locations indicates that the CT has a velocity exceeding 100 km/s. The CT length estimated from FWHM of $\bar{n}_e$ signal is about 1 m.

Radial profiles of the CT magnetic field are depicted in Fig. 4.4.5. These profiles were measured inside the larger vacuum chamber of 0.32 m diameter (Fig. 4.4.5 (a) and (b)), or the small vacuum chamber of 0.15 m diameter (Fig. 4.4.5 (c)). The magnetic field strength

increases with the charging voltage of the CT generation bank. The B_p profile has a reversal point, which characterizes the spheromak configuration. In Figs. 4.4.5 (a) and (b), the radial location of the reversal point is ~ 0.06 m, and this is twice larger than that observed when the small vacuum chamber was used (see Fig. 4.4.5 (c)). From this observation, the vacuum chamber seems to be working as a shell that determines the CT size. This is an expected, but severe problem, since the port of LHD has a large size of order 1 m. Therefore, a drift tube that can work as a shell is necessary to transfer the CT through the LHD port.

4.4.3. Two-stage acceleration experiment

Two-stage acceleration experiments have been carried out on SPICA. In this section, the experimental results obtained with the extended acceleration electrode as shown in Fig. 4.4.3 are presented.

4.4.3.1. Control parameters

In the two-stage acceleration experiment, discharges are controlled by five parameters; i.e. the gas puff pulse length, τ_{puff}, the biasing coil current, I_{bias}, the charging voltage of CT generation bank, V_{gen}, the charging voltage of CT acceleration bank, V_{acc}, and the trigger delay of the CT acceleration bank from the CT generation bank trigger timing, τ_{delay}.

The pre-fill pressure inside the SPICA is controlled by τ_{puff}. The relation between τ_{puff} and the pressure rise in SPICA without vacuum pumping is shown in Fig. 4.4.6 (a). In this study, four piezo-valves are used at the CT generation electrode (see Fig. 4.4.3). The product of the pressure rise and the volume of 0.56 m^3, which is the sum of the volumes inside the SPICA and the large test chamber, gives the total number of hydrogen atoms supplied by gas puffing, N_{puff} (see Fig. 4.4.6 (b)). In the experiment, τ_{puff} of 6.0 ms was frequently used and then $N_{puff} \sim 7 \times 10^{20}$, for instance.

As already mentioned in section 4.4.1, the maximum of I_{bias} is 300 A. Corresponding biasing magnetic field, B_{bias}, at the center of the coil is 0.142 T. Then, the maximum axial magnetic flux penetrating the generation inner-electrode of 0.16 m diameter is 11.4 mWb.

Due to the discharge current limitation, the charging voltage of the bank should not exceed a critical value, which is not necessarily the same as the maximum charging voltage. The peak value of the discharge currents $(I_{gen})_{max}$ and $(I_{acc})_{max}$ versus V_{gen} and V_{acc}, respectively, are plotted in Fig. 4.4.7. The current limit of the CT generation bank (300 kA) is

reached at $V_{gen} \sim 10$ kV. On the other hand, the current limit of 400 kA has not been reached for the CT acceleration bank. As shown in Fig. 4.4.7 (c), $(I_{gen})_{max}$ and $(I_{acc})_{max}$ can be fitted by the power function of $(V_{gen})^{0.88}$ and $(V_{acc})^{0.75}$, respectively. Extrapolating this, it is expected that the current limit of the CT acceleration bank will be reached at $V_{acc} \sim 30$ kV.

4.4.3.2. Typical waveforms

An example waveform in the two-stage acceleration experiment without the drift tube is shown in Fig. 4.4.8. In this case, $V_{gen} = 9.5$ kV and $V_{acc} = 15.2$ kV. The discharge currents I_{gen} and I_{acc} are ~ 300 kA and ~ 250 kA, respectively, as shown in the top of Fig. 4.4.8. The CT acceleration bank is triggered at 15.9 μs after the CT generation bank. The bias coil current I_{bias} is 240 A and then the magnetic field strength at the center of the biasing coil $B_{bias} = 0.114$ T. The gas puff pulse length $\tau_{puff} = 6$ ms. The CT position is monitored by the visible light signals, B_p, B_t, and $\bar{n}_e$, which are shown in the bottom of Fig. 4.4.8, with an offset that corresponds to the axial distance of the measurement position from the gas puff port. The CT velocity, v_{CT}, is determined from the time of flight of the signals at different location. Basically, we use the edge magnetic signals at the port **D** and **H**. The timings where B_{pa} at **D** and B_{ta} at **H** appear are defined as $t_{m@D}$ and $t_{m@H}$, respectively. Then v_{CT} is determined by

$$v_{CT} \equiv 1.36 / (t_{m@H} - t_{m@D}),$$

where 1.36 m is the distance from the port **D** to the port **H**. For example, $v_{CT} = 122.5$ km/s is obtained for the case of Fig. 4.4.8. Note that v_{CT} can be taken as a constant after the CT passes through **D**, and even in the test chamber. In the small V_{acc} discharges, however, the magnetic signal at the port **H** is small and it is difficult to determine v_{CT} in this way. Therefore, we use $\bar{n}_e$ instead of B_{ta} at **H**, in such a case.

Typical CT generated by SPICA has a head component of high magnetic field strength and short length, followed by a high-density and long tail component. Three examples of the simultaneously measured magnetic and density signals at the port **H** are shown in Fig. 4.4.9. Note that the abscissa is given by $(t - t_{m@H})\ v_{CT}$, which has a unit of length. The magnetic field strength is large at the leading edge of the CT. The length of this component is ~ 1 m. The CT density keeps comparatively small level during B_{pa} is large. At where B_{pa} sharply decreases, $\bar{n}_e$ increases to its maximum and then gradually decreases. In this study, the CT length, L_{CT}, is determined as the product of v_{CT} and the FWHM of $\bar{n}_e$.

Typical order of L_{CT} is a few meters as can be seen in the figure.

4.4.3.3. τ_{puff} scan and I_{bias} scan experiments

It is important to know how the CT parameter such as the density changes with the control parameters. Here, the response of CT density to τ_{puff} is investigated. As for the CT magnetic field strength, it is shown to be a function of I_{bias}.

The maximum of $\bar{n}_e$ measured at the port **H**, $(\bar{n}_e@H)_{max}$, is plotted in Fig. 4.4.10 (a). In this τ_{puff} scan experiment, other parameters than τ_{puff} and τ_{delay} are fixed; i.e. V_{gen} = 10.0 kV, V_{acc} = 13.3 kV, and I_{bias} = 240A (B_{bias} = 0.114 T). As seen in the figure, $\bar{n}_e$ can be controlled by τ_{puff}. The total number of hydrogen atoms in the CT, N_{CT}, is estimated from L_{CT}, the CT radius at the measured position, and the time-averaged value of $\bar{n}_e$ within the FWHM. The ratio of N_{CT} to N_{puff}, which is depicted in Fig. 4.4.10 (b), ranges from 10 to 25 %.

Next, I_{bias} is scanned to examine the response of the CT magnetic field strength. The maximum of the edge poloidal magnetic field strength measured at the port **H**, $(B_{pa}@H)_{max}$, is plotted in Fig. 4.4.11 (a). In this I_{bias} scan experiment, other parameters than I_{bias} and τ_{delay} are fixed; i.e. V_{gen} = 9.0 – 9.5 kV, V_{acc} = 15.2 kV, and τ_{puff} = 6.0 ms. In spite of the large scatter, $(B_{pa}@H)_{max}$ increases with I_{bias}. In the same figure, a solid line that denotes B_{bias} is also shown for comparison. Due to the compression effect of the conical acceleration electrode of SPICA, it is expected that $(B_{pa}@H)_{max}$ becomes larger than B_{bias}, if the CT compression time, τ_{comp}, is slower enough compared to the time of Alfvén wave transmission across the CT radius, τ_A. The results shown in Fig. 4.4.11 (a) suggest that this compression mechanism is effectively working since $(B_{pa}@H)_{max} > B_{bias}$ is achieved in many cases. Note that the B_p at the center of the CT is larger than that at the edge (see Fig. 4.4.5, for example). The large scatter in Fig. 4.4.11 (a) is mainly resulted from the different τ_{delay} used in each discharge, as depicted in Fig. 4.4.11 (b). The better τ_{delay} that achieves $(B_{pa}@H)_{max} > B_{bias}$ is plotted by closed circles. It is important to precisely adjust τ_{delay} to obtain a large CT magnetic field. In the region of large I_{bias} (> 250 A), the operation window of τ_{delay} tends to be smaller and therefore the adjustment becomes more difficult.

4.4.3.4. V_{acc} scan experiment

The most important control parameter that largely affects the CT performance is V_{acc}. In this subsection, the results of the V_{acc} scan experiment are given. According to the results of the former subsection, other four control parameters are chosen and fixed; i.e. V_{gen} = 9.0 kV, I_{bias} = 180 A (B_{bias} = 0.085 T), τ_{puff} = 6.0 ms, and τ_{delay} = 15.9 μs.

As mentioned before, v_{CT} is determined from the time-of-flight of the magnetic and/or the density signals measured at different axial location. The timings of the signal appearance for different V_{acc} are summarized in Fig. 4.4.12 (a). Other than $t_{m@D}$ and $t_{m@H}$ that are mainly used to determine v_{CT}, the timings where the density signal appears at the port **F**, **G**, and **H** are also plotted as $t_{ne@F}$, $t_{ne@G}$, and $t_{ne@H}$, respectively. The trigger timing of the CT acceleration bank, t_{acc0}, and the half period of the acceleration current, t_{acc1}, are also shown for comparison. In the range of V_{acc} < 7 kV, it is difficult to determine $t_{m@H}$ because of the low signal level. Therefore we use $t_{ne@F}$ / $t_{ne@G}$ / $t_{ne@H}$ instead of $t_{m@H}$, in that range for v_{CT} estimation. The V_{acc} dependence of v_{CT} is shown in Fig. 4.4.12 (b). In the range of V_{acc} < 7 kV, v_{CT} moderately increases with V_{acc}. A remarkable increase in v_{CT} with V_{acc} is seen in the high V_{acc} region of V_{acc} > 7 kV. Since Fig. 4.4.12 (b) is a semi-log plot, this suggests that v_{CT} exponentially increases with V_{acc}. It should be noted that the threshold V_{acc} = 7 kV is not resulted from the use of different estimation method, since a similar result is obtained even using $t_{m@D}$ and $t_{ne@H}$ in V_{acc} > 7 kV.

Other than v_{CT}, the CT magnetic field strength and the CT density also depend on V_{acc}. As shown in Fig. 4.4.13 (a), B_{pa} at the port **H** begins to increase at V_{acc} > 10 kV, and finally exceeds the B_{bias}. Again, this indicates the compression effect as discussed in the former subsection. At the port **D**, which locates at less than the half of the acceleration electrode and therefore a significant compression effect is not expected, B_{pa} tends to saturate at a value similar to B_{bias}, in the range of V_{acc} > 9 kV. As for the density shown in Fig. 4.4.13 (b), it increases in the range of V_{acc} < 10 kV and then begins to decrease with V_{acc}. However, the compression effect on the CT density cannot be recognized; i.e. there is no significant difference in $\bar{n}_e$ measured at various axial location. To achieve the density increase by the compression, the particle confinement time of the CT, τ_p, should be large enough compared with τ_{comp}, which is not the case here. In other words, it is suggested from the result that τ_p is similar or less than τ_{comp} ~ 20 μs.

CT kinetic energy, K_{CT}, is estimated from v_{CT} and N_{CT} measured at the port **H** or **H'**. The estimation results are shown in Fig. 4.4.14, where L_{CT}, N_{CT}, and K_{CT} are shown. In the

range of V_{acc} < 9 kV, L_{CT} gradually decreases to 0.7 m. However, with larger V_{acc} than 9 kV, L_{CT} begins to increase and approaches to 10 m. On the other hand, N_{CT} shows monotonic increase with V_{acc} up to 14 kV. As has been already shown in Fig. 4.4.12, v_{CT} significantly increases with V_{acc}. Resultant K_{CT} increases rapidly with E_{acc} and in proportion to the fourth power of E_{acc}.

4.4.3.5. Long distance transfer of the CT

The critical pass of the CT injection in LHD lies in the long distance transfer of the CT. This is examined by the use of the large test chamber of 3.6 m long. Under the proper experimental condition, the magnetic signals can be detected even at the farthest port **N**. Typical waveform of such a discharge is shown in Fig. 4.4.15, where $|B_0| \equiv \sqrt{{B_{p0}}^2 + {B_{t0}}^2}$ appears at **N** at the time predicted by the linear extrapolation of v_{CT}.

Based on the results of the initial experiments discussed in section 4.4.2, a drift tube is necessary to keep the CT radius as small as the inner radius of the acceleration electrode at its exit. The influence of the drift tube has been examined in the V_{acc} scan experiment. The E_{acc} dependence of $|B_0|$ at **N** is shown in Fig. 4.4.16, where the results with or without the drift tube are plotted. Without the drift tube, the peak value of $|B_0|$ measured at **N**, $(|B_0|@N)_{max}$, increases at E_{acc} = 6 – 8 kJ, and saturates to ~ 0.02 T, at the range of E_{acc} > 8 kJ. This behavior resembles to that of $(B_{pa}@H)_{max}$ discussed in the former subsection. With the drift tube, $(|B_0|@N)_{max}$ becomes smaller than that obtained w/o the drift tube, although it continues to increase within E_{acc} = 15 kJ. This suggests an enhanced decay of the CT magnetic field due to the existence of the drift tube.

One of the possible reasons for this might be the insufficient wall conditioning of the drift tube. Although the drift tube was cleaned by means of the electric polishing, the exposure time of the plasma-facing wall to plasmas remains at most a hundred times to date. At this moment, however, it can be concluded that the drift tube of 0.16 m diameter is less effective to sustain the CT magnetic field compared with the test chamber of 0.32 m diameter. Note that the test chamber is possibly working as a large-diameter drift tube. Therefore, a drift tube of 0.32 m diameter is better for the CT injection experiment on LHD.

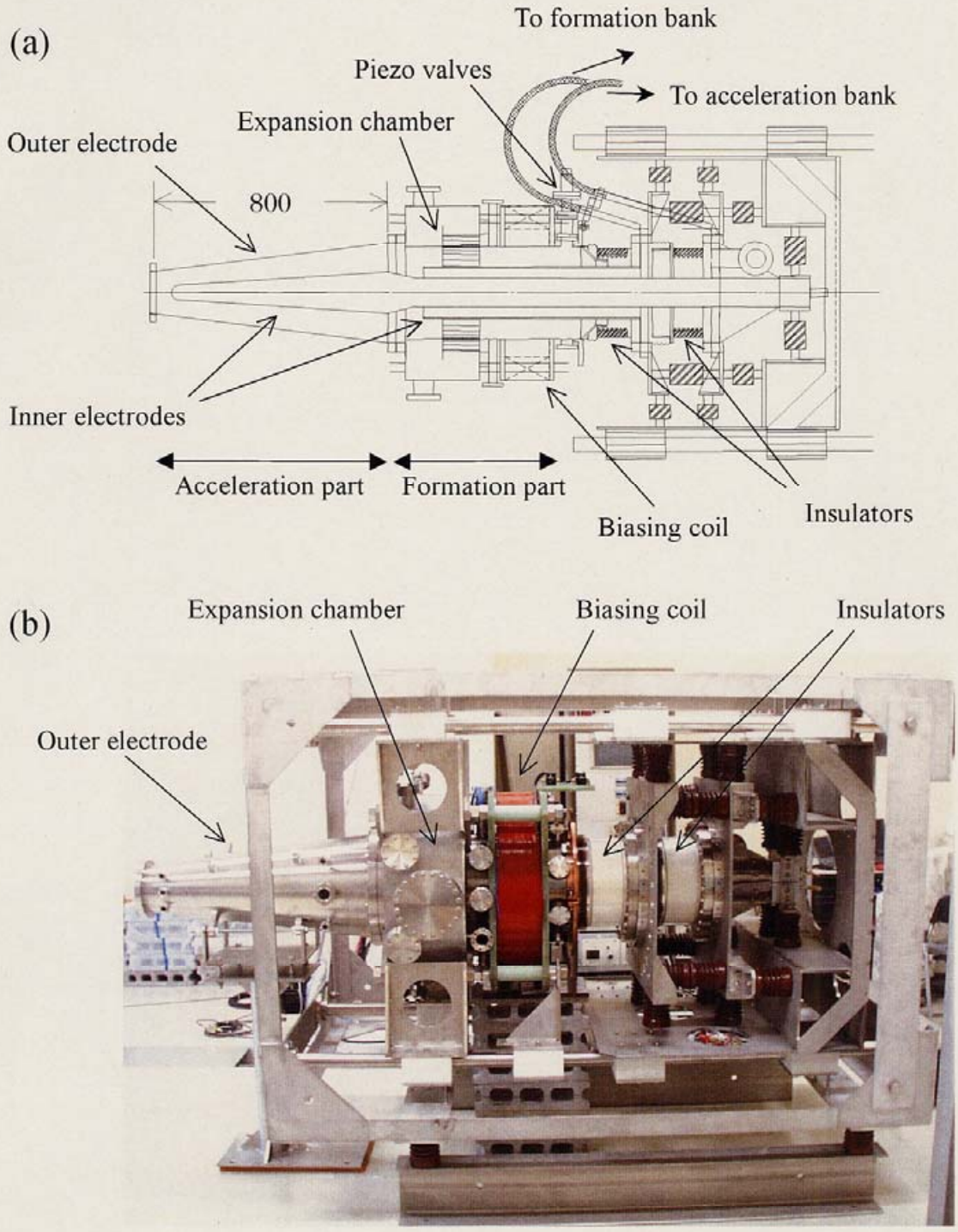

Fig. 4.4.1. (a) Schematic of SPICA with a short (0.8 m) acceleration electrode and (b) the photograph. Electrical circuit is identical to that shown in Fig. 4.1.1.

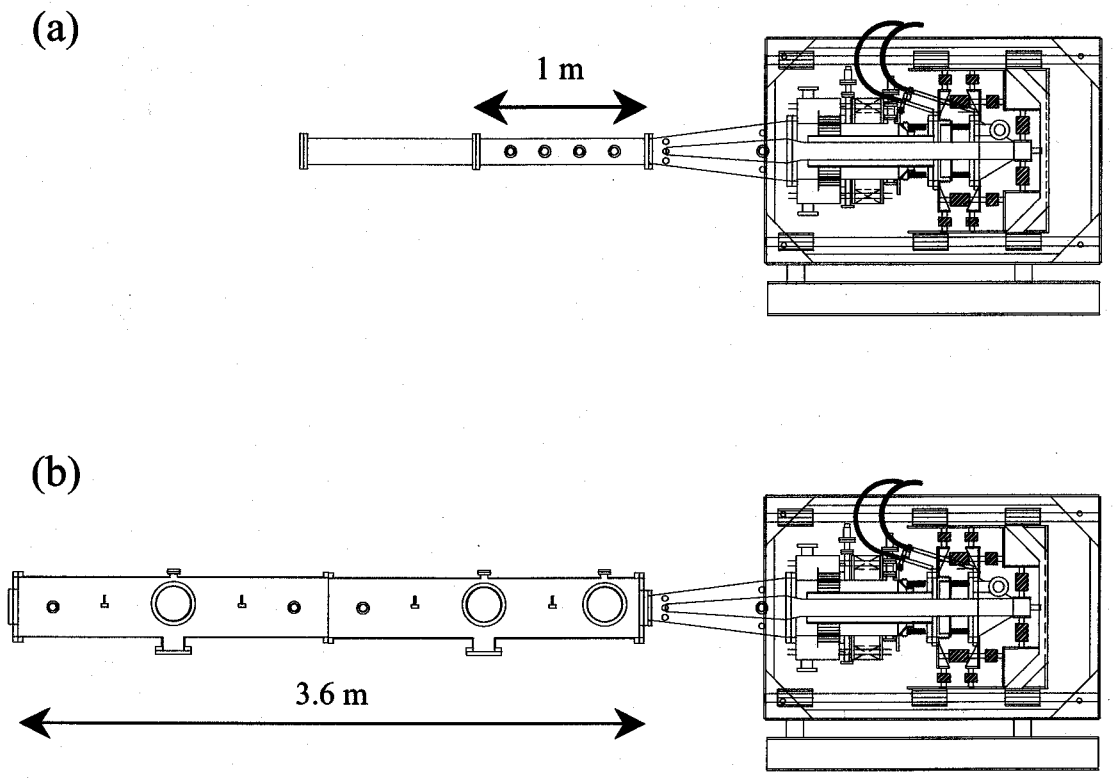

Fig. 4.4.2. Schematic view of (a) the small test chamber used in the earlier phase of the initial experiment, and (b) the large test chamber, which has been used mainly in this study.

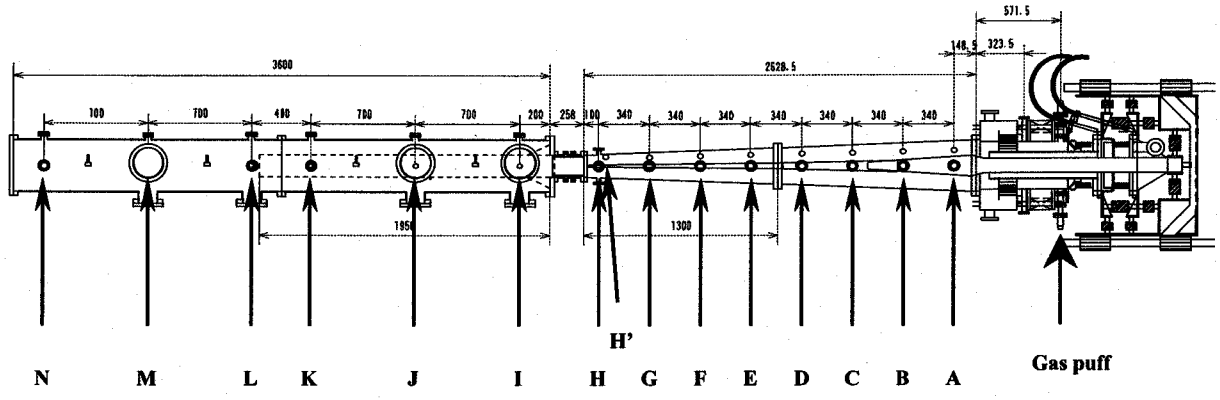

Fig. 4.4.3. Schematic view of SPICA with an extended acceleration electrode. A drift tube is installed inside the large test chamber (drawn by broken lines).

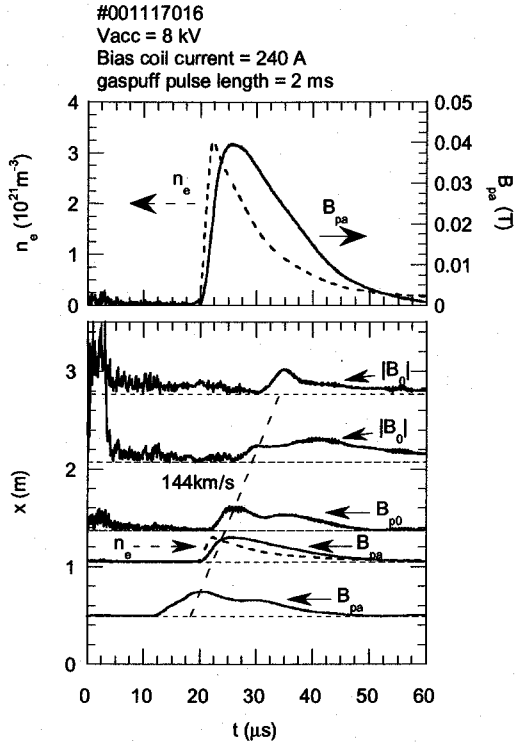

Fig. 4.4.4. Waveforms of the line-averaged electron density $\bar{n}_e$, the poloidal magnetic field strength at the plasma edge B_{pa} (top) and magnetic signals at various axial locations (bottom). In the bottom figure, each trace is offset vertically by a distance proportional to the axial location, and the broken line denotes the linear trajectory of a CT with 144km/s velocity.

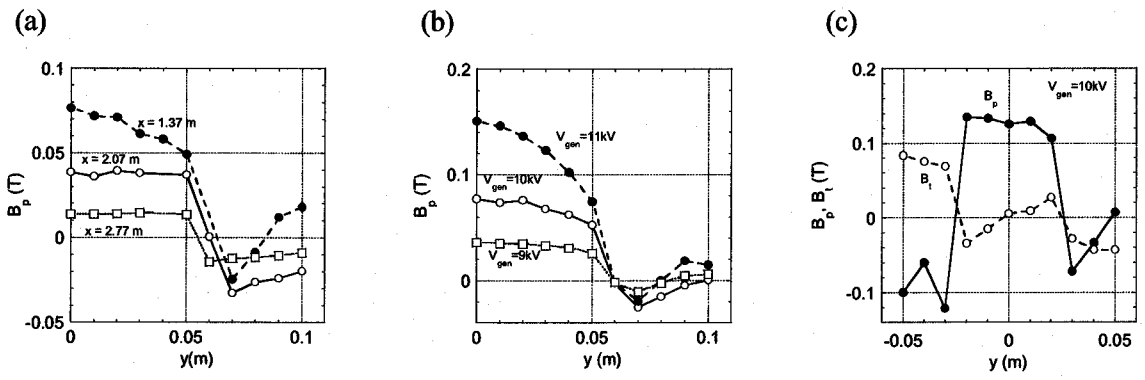

Fig. 4.4.5. (a) Radial profiles of B_p at different positions in the large test chamber. Discharge parameters are fixed as; V_{gen} = 10 kV, I_{bias} = 240 A (B_{bias} = 0.114 T), and τ_{puff} = 2 ms. (b) Radial profiles of B_p in the large test chamber. CTs are generated by different charging voltages as denoted. These profiles are measured at 0.2 m from the exit of the acceleration electrode (x = 1.37 m). (c) Radial profiles of B_p in the small test chamber of which the inner radius is 0.075 m.

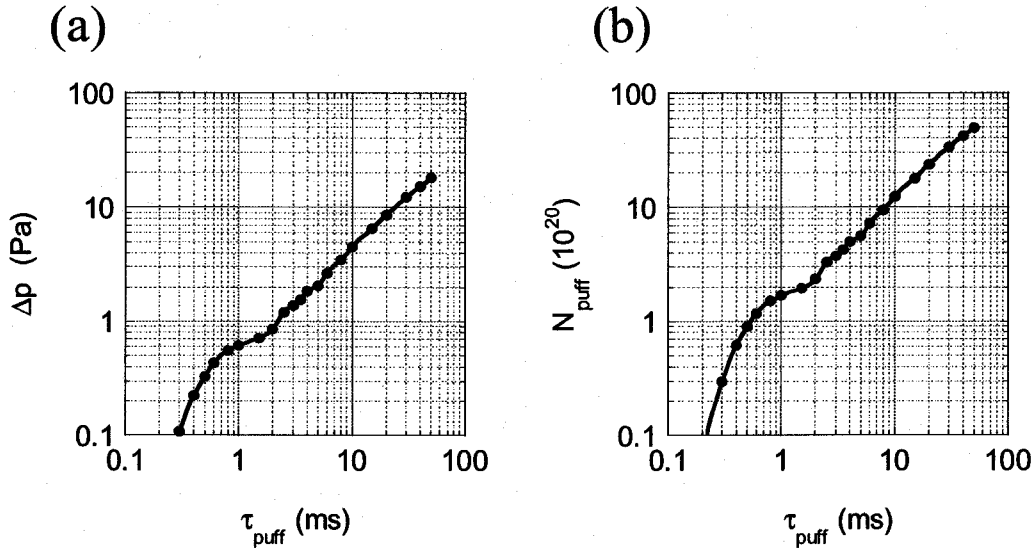

Fig. 4.4.6. (a) Pressure rise measured by an ionization gauge, Δp, and (b) the total number of hydrogen atoms, N_{puff}.

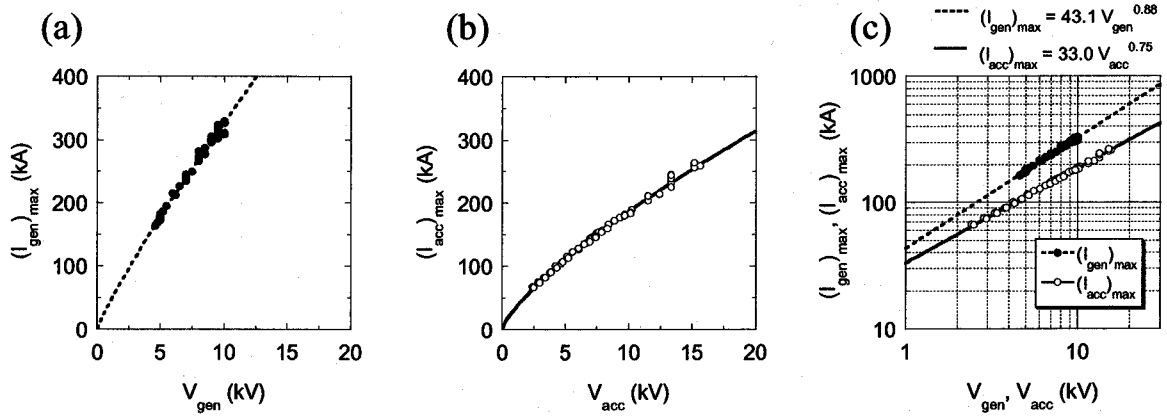

Fig. 4.4.7. (a) V_{gen} vs the peak values of the discharge current of CT generation bank, $(I_{gen})_{max}$. (b) V_{acc} vs the peak values of the discharge current of CT acceleration bank, $(I_{acc})_{max}$. (c) Power function fitting of $(I_{gen})_{max}$ and $(I_{acc})_{max}$.

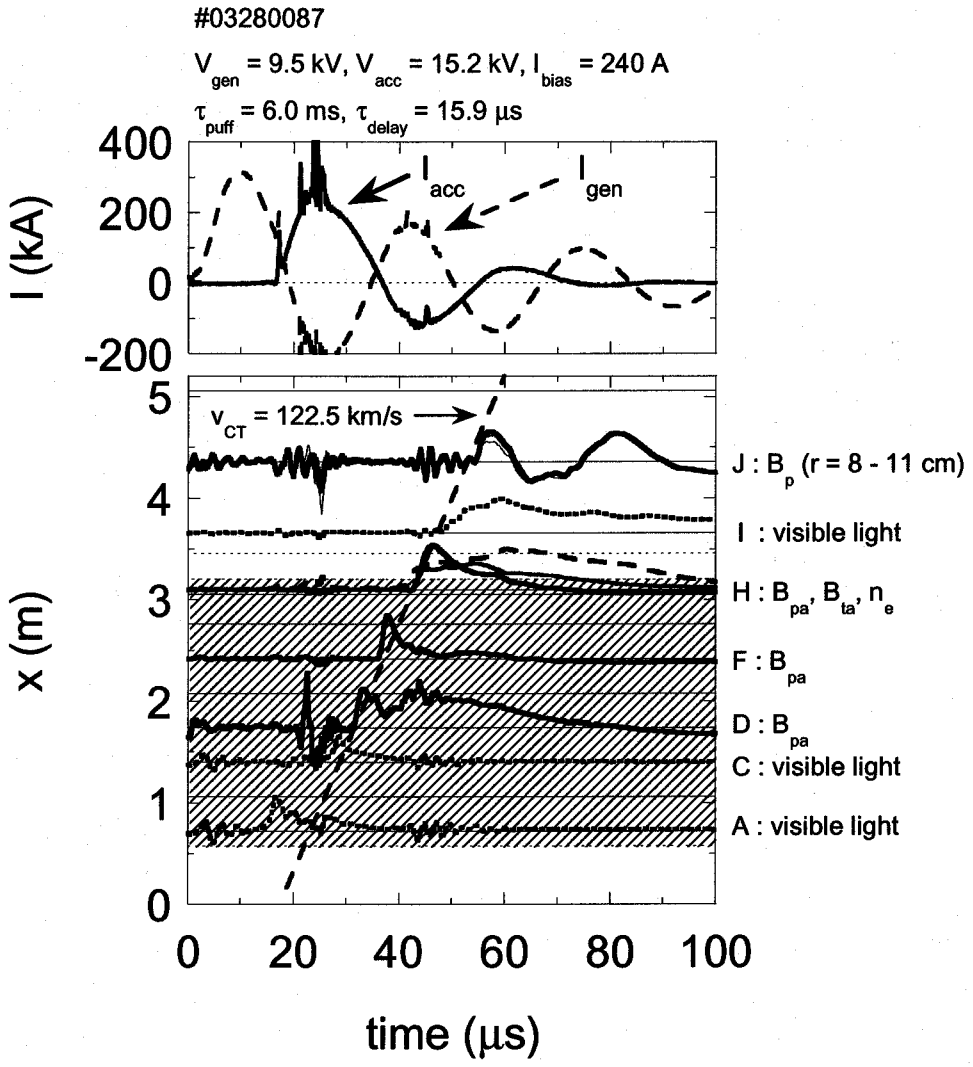

Fig. 4.4.8. Typical waveforms in the two-stage acceleration experiment with the extended acceleration electrode. Discharge currents, I_{gen} and I_{acc}, are shown on the top. In the bottom figure, CT motion is traced by the visible light signals, the magnetic signals, and the density signal. Offsets of these signals correspond to the axial location of the measurements. Hatched region in the bottom figure indicates the region of the acceleration electrode. In this case, the drift tube was not used.

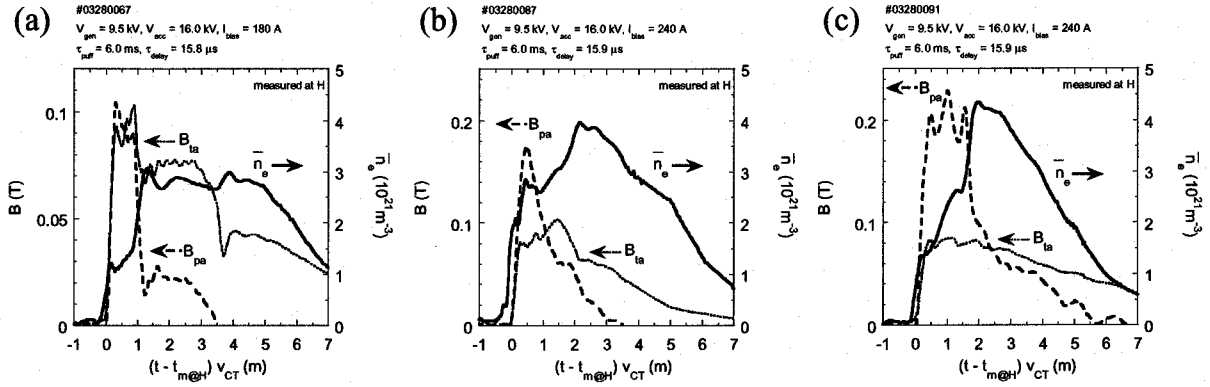

Fig. 4.4.9. CT magnetic field and CT density measured at the end of acceleration electrode (port **H**). Discharge parameters used are shown on the top of each figure. The abscissa is given by $(t - t_{m@H})\, v_{CT}$ and has a unit of length.

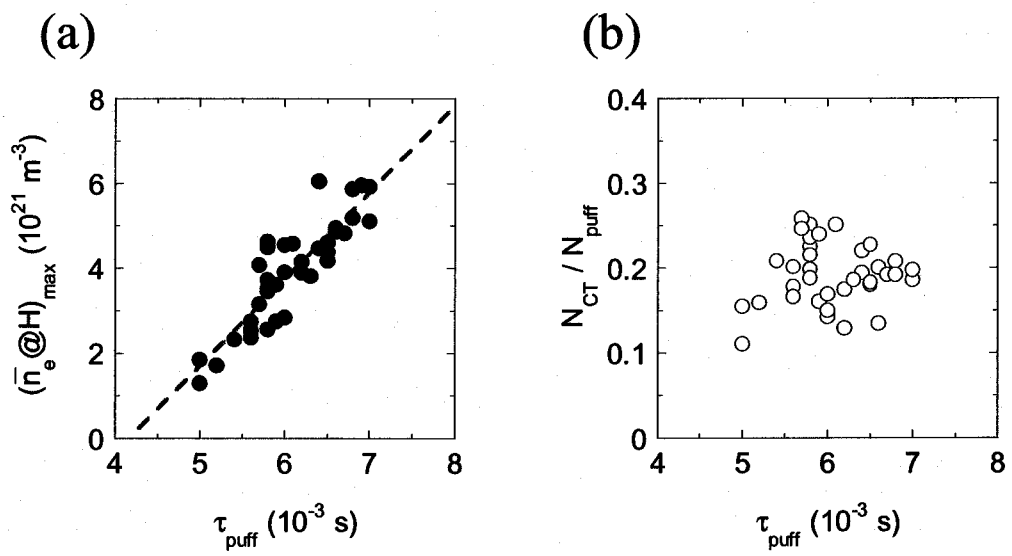

Fig. 4.4.10. Results of τ_{puff} scan experiment. (a) Peak values of the line-averaged electron density measured at the end of acceleration electrode (port **H**), $(\bar{n}_e@H)_{max}$. (b) The ratio of total number of hydrogen atoms in the CT, N_{CT}, to N_{puff}. Control parameters other than τ_{puff} and τ_{delay} are fixed; i.e. V_{gen} = 10.0 kV, V_{acc} = 13.3 kV, and I_{bias} = 240 A.

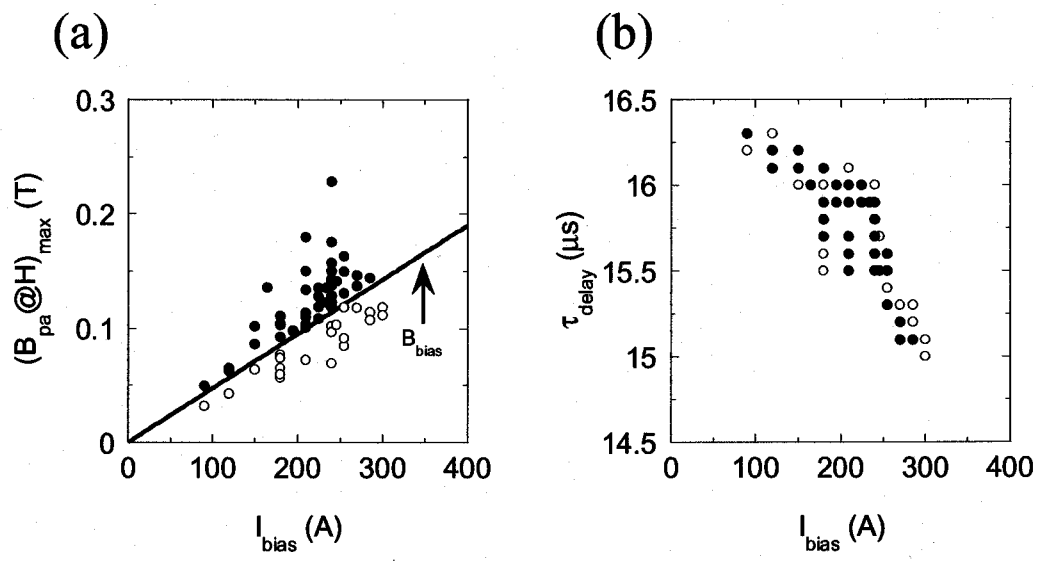

Fig. 4.4.11. Results of I_{bias} scan experiment. (a) Peak values of the edge poloidal magnetic field strength measured at the end of the acceleration electrode (port **H**), $(B_{pa}@H)_{max}$. Solid line denotes the magnetic field strength of the biasing coil, B_{bias}. (b) τ_{delay} used in the scan. Closed circles in (b) denote the τ_{delay} that achieves $(B_{pa}@H)_{max} > B_{bias}$. Control parameters other than I_{bias} and τ_{delay} are fixed; i.e. $V_{gen} = 9.0 - 9.5$ kV, $V_{acc} = 15.2$ kV, and $\tau_{puff} = 6.0$ ms.

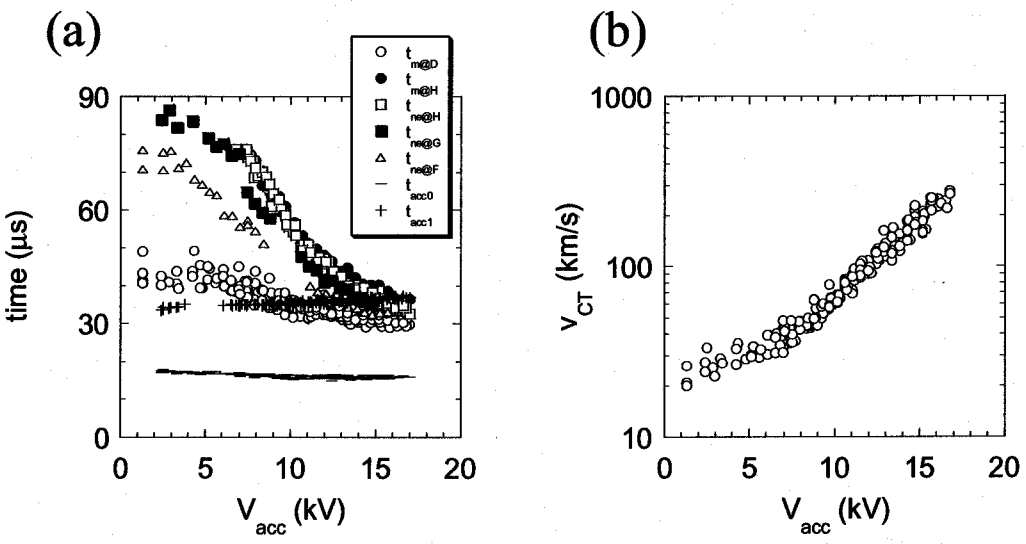

Fig. 4.4.12. Results of V_{acc} scan experiment. (a) Timings of the signal appearance, the trigger timing of the CT acceleration bank, t_{acc0}, and the half period of the acceleration current, t_{acc1}. (b) CT velocity as a function of V_{acc}. Control parameters other than V_{acc} are fixed; i.e. $V_{gen} = 9.0$ kV, $I_{bias} = 180$ A, $\tau_{puff} = 6.0$ ms, and $\tau_{delay} = 15.9$ μs.

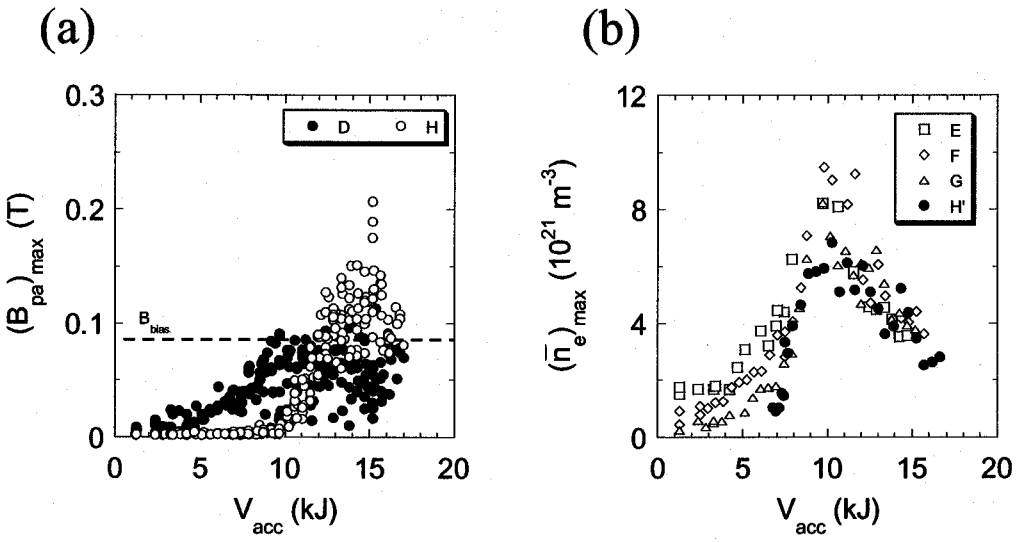

Fig. 4.4.13. Results of V_{acc} scan experiment. (a) Peak values of the edge poloidal magnetic field measured at the port **D** or **H**. (b) Peak values of $\bar{n}_e$ measured at **E**, **F**, **G**, and **H'**. Analyzed discharges are identical to that in Fig. 4.4.12.

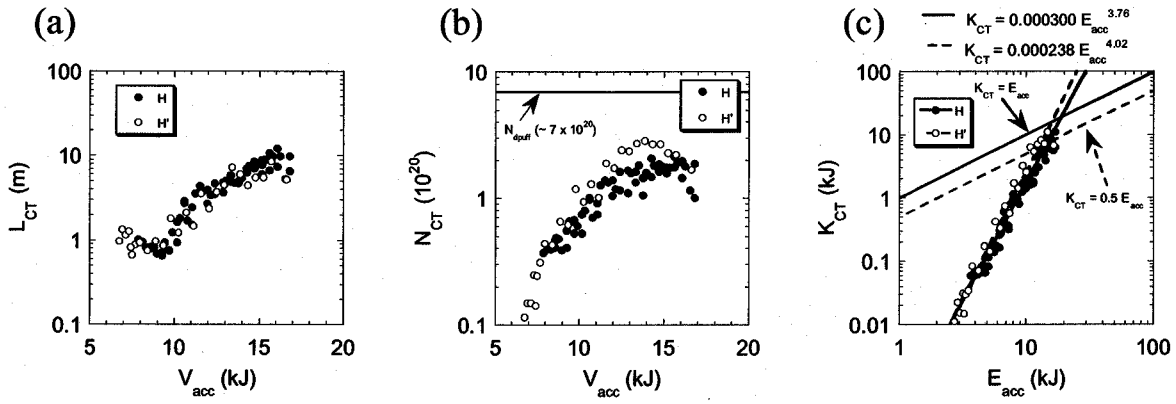

Fig. 4.4.14. Results of V_{acc} scan experiment. (a) CT length, (b) the total number of hydrogen atoms, and (c) the CT kinetic energy, measured at the port **H** or **H'**. Note that the abscissa in (a) and (b) is V_{acc}, while it is E_{acc} in (c). Analyzed discharges are identical to that in Fig. 4.4.12.

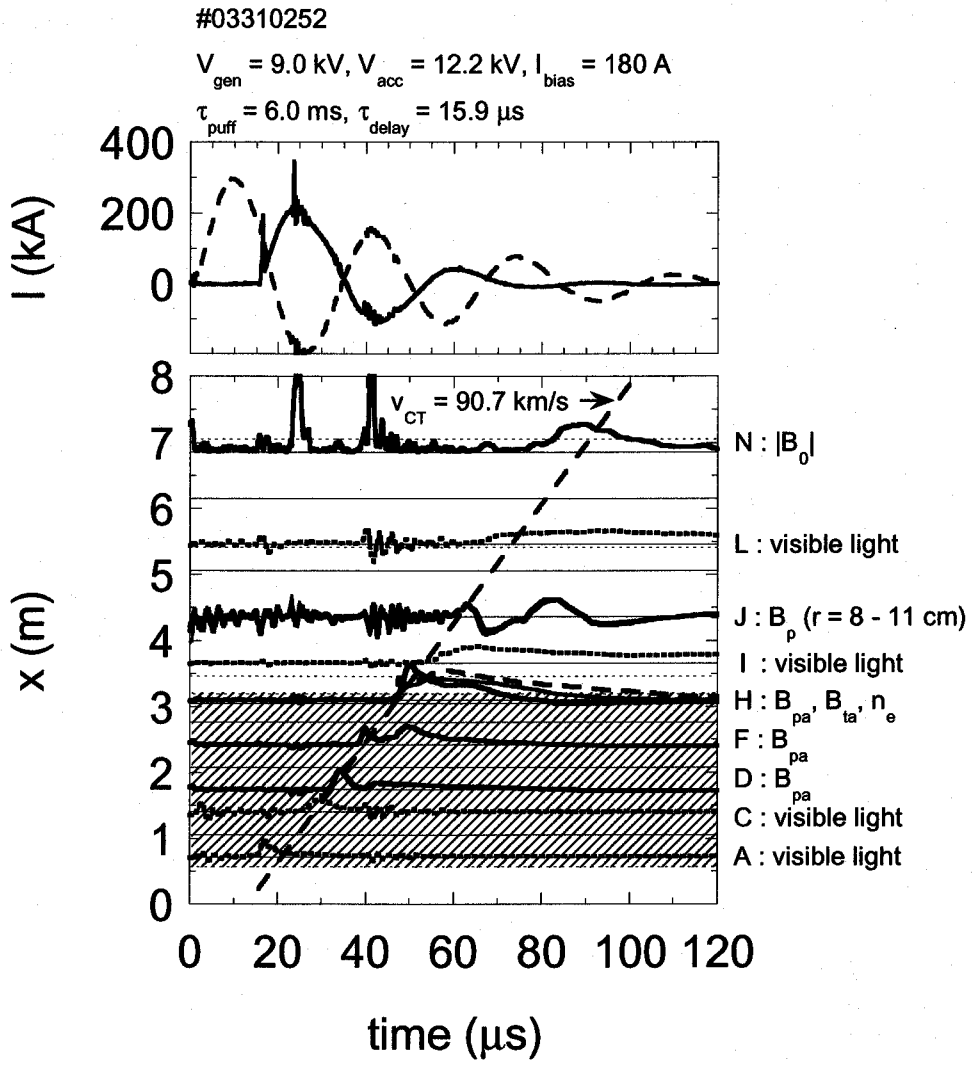

Fig. 4.4.15. Typical waveforms in the two-stage acceleration experiment with the extended acceleration electrode. Discharge currents, I_{gen} and I_{acc}, are shown on the top. In the bottom figure, CT motion is traced by the visible light signals, the magnetic signals, and the density signal. The offsets of these signals correspond to the axial location of the measurements. Hatched region in the bottom figure indicates the region of the acceleration electrode. In this case, the drift tube was not used.

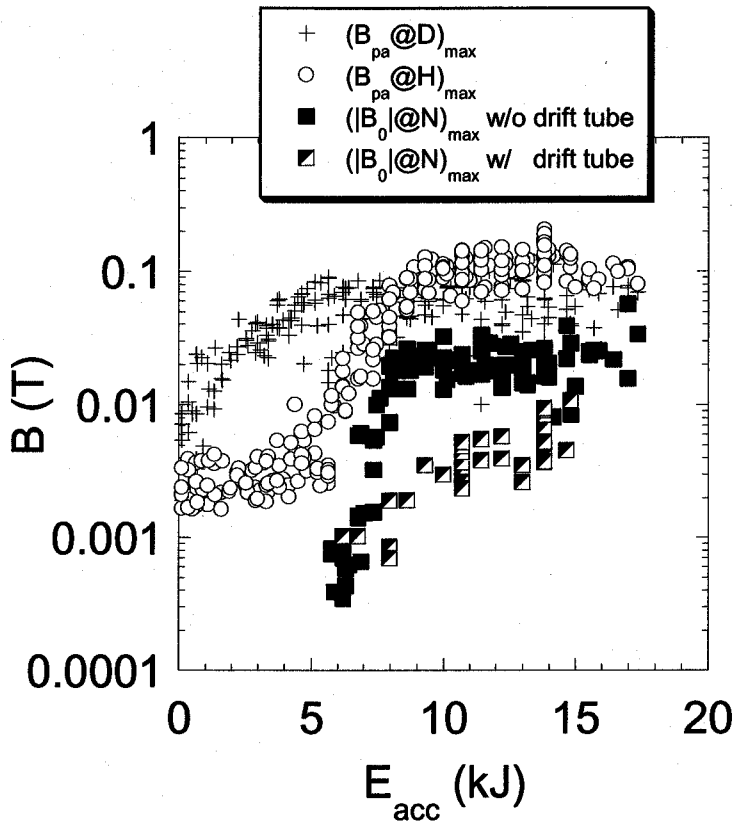

Fig. 4.4.16. Results of V_{acc} scan experiment. The peak value of B_{pa} measured at the port **D** or **H** (same data plotted in Fig. 4.4.13 (a)) and the peak value of $|B_0|$ measured at the port **N** in the discharges with or without the drift tube are shown. Analyzed discharges are identical to that in Fig. 4.4.12.

4.5. Summary

Three-dimensional CT orbit in the LHD magnetic field has been calculated. As a result, central fueling is confirmed to be possible with realistic parameters of CT, such as 20 cm diameter, 10^{22} m^{-3} electron density, and 300 km/s initial velocity. In this study, 1.5 T LHD magnetic field is used for the calculation, so that in the case of 3 T LHD magnetic field, one should use a faster (~ 600 km/s) or heavier (~ 0.3 mg) CT to achieve the center fueling. Note that the large velocity and the heavy mass of CT have the same meaning in the orbit calculation. One should be careful to set the CT injector to the appropriate position such as that found in this study. Even if the CT is electrically charged up to 0.1 % electron density, it can penetrate the plasma core although the trajectory is bent due to Lorentz force. This finding supports the idea of a non-neutral CT injection as a biasing electrode, to control the electric field inside the main plasma.

A point model of CT acceleration in a co-axial electrode has been solved using the fourth-order Runge-Kutta method to obtain the optimum design of a CT injector. It was revealed that the ratio of electrode inductance to the external inductance determines the acceleration efficiency. The high efficiency CT injector can be realized by reduction in the external inductance and enlargement of the volume inside the injector to increase the electrode inductance. Adiabatic compression using conical accelerator is also proposed. The optimum design is obtained by scanning various parameters for given conditions. More than 34 % of acceleration efficiency and about 15 kJ of CT kinetic energy are expected with a long (3.2 m) acceleration electrode. This is enough to carry out the CT injection into LHD. Moderate electrode length of 1.6 m results in the less CT kinetic energy of 7.5 kJ in the optimum condition, but still available for CT injection into the LHD plasma with 1.5 T magnetic fields. In our experimental scenario, a short electrode of 0.8 m long is adopted for the first step. In spite of the small acceleration efficiency of 15.7 %, such a compact injector is useful to study the basic techniques of CT formation and acceleration.

A CT injector for LHD named SPICA has been developed and the CT acceleration experiments have been carried out successfully. In the initial experiments, it was confirmed that SPICA generates a CT with the spheromak-type internal magnetic field profile. It was also suggested that the wall of the test chamber is working as a shell that determines the CT size. In the two-stage acceleration experiment with an extended acceleration electrode of 2.6 m long, CT velocity of over 200 km/s and CT density of order 10^{21} m^{-3} have been observed.

The CT generated in the two-stage acceleration experiment on SPICA consists of a short (~ 1 m) leading component, which is characterized by the large magnetic field and relatively low density, and a long (a few meters) tail component that has higher density. To obtain a sufficient CT magnetic field at the tip of the acceleration electrode, the charging voltage of the acceleration bank should be larger than 10 kV. The compression effect of the conical acceleration electrode has been proved from the CT magnetic field larger than the biasing magnetic field. As for the CT density, the compression effect has not been recognized, suggesting that the particle confinement time is less than ~ 20 μsec. The CT velocity has a strong dependence on the stored energy of the acceleration bank and exponentially increases with the stored energy. At the same time, the CT length also increases while the peak CT density decreases. Resultant kinetic energy of the CT is in proportion to the fourth power of the stored energy of the CT acceleration bank. The long distance transfer of CT was examined in the large test chamber with or without a drift tube inside. It has been demonstrated that the CT can be transferred more than 3.6 m after the acceleration. To avoid a severe decay of the CT magnetic field while keeping an adequate CT size, a drift tube of 0.32 m diameter might be better than that of 0.16 m diameter, for the CT injection experiment on LHD.

Although a good prospect in the CT injection experiment on LHD has been obtained, there also are unsolved problems. First of all, the trajectory of a long CT in the LHD magnetic field might be different from that simulated in section 4.2 assuming a spherical CT. Therefore, the CT kinetic energy needed to achieve the direct fueling into the plasma core can be different from that expected. In such a case, one should decrease the LHD magnetic field strength. Note that the low magnetic field experiment has been often carried out on LHD to achieve the high β condition and it will be interesting to perform the CT injection into the high β plasmas. Secondary, the stray magnetic field intersecting the drift tube is thought to prevent the CT motion. Since the CT has perfect diamagnetic property, it pushes aside the stray magnetic flux in the drift tube. Then the magnetic pressure increases and it slows down the CT velocity. If the inner radius of the drift tube is much larger than the CT radius and there is an enough space between the CT and the wall, such a local increase of the magnetic pressure can be mitigated. Therefore, one can be optimistic on this problem as long as a drift tube of 0.32 m diameter is to be adopted. Third, the particles injected by SPICA is 2×10^{20} at most, and a large part of these is not necessarily included in the strongly magnetized component. Furthermore, this will decrease before the CT reaches the LHD plasma due to the small particle confinement time. To deliver the CT faster than the density decrease, it is

necessary to increase the CT velocity. This can be achieved by elongating the acceleration electrode and increase the electrode inductance. As has been shown, a large electrode inductance helps to obtain the higher acceleration efficiency.

Taking into account the above problems, the best scenario of the CT injection experiment on LHD using SPICA can be summarized as below.

- Target is the high β plasma.
- With a drift tube of ~ 0.3 m diameter set inside the LHD port.
- Injection from the lower port and set the electrode vertically. This makes it easy to elongate the acceleration electrode.
- Elongate the acceleration electrode from 2.6 m to 3.2 m, which is favorable to achieve the optimum condition in Table. 4.3.3.

One should pay attention to the perturbations due to CT injection and its effect on the confinement property of the LHD plasma. Since there is no method to generate the fast magnetic perturbation other than the CT injection, it will give a new and interesting point of view. Although the particle numbers injected by SPICA is expected to be not so large, it will be also interesting to investigate the synergetic operation with other fueling such as gas puffing and ice-pellet injection.

Chapter 5 Conclusion

In this thesis, the experimental results related to the most basic fueling method; gas puffing, and the possibility of the most advanced fueling method; CT injection, have been discussed in the framework of LHD. The gas puff experiments with various gases were carried out to investigate the fueling efficiency of gas puffing, the role of recycling flux, the effect of the metal impurity reduction, and the confinement property of plasmas with different ion species. The possibility of CT injection experiment on LHD was researched based on the CT orbit calculation and the development of the CT injector SPICA.

By means of the gas puff experiments with hydrogen, helium, methane and neon, conclusions as itemized below have been made.

[Hydrogen gas puff]

- The effective fueling efficiency ranges from 10 to 50 %.
- Scatter in the effective fueling efficiency is due to the recycling flux.
- The recycling flux increases and the recycling coefficient decreases due to gas puffing.
- At the limit of small recycling flux, the effective fueling efficiency decreases to 10 %, which corresponds to the fueling efficiency of hydrogen gas puffing in LHD.

[Helium gas puff]

- The effective fueling efficiency ranges from 20 to 100 % and higher than the hydrogen gas puffing.
- The perfect recycling condition where the recycling coefficient is unity even with gas puffing is likely be achieved.

[Methane gas puff]

- Real time carbonization (RTC) by methane gas puff is effective to reduce the metal impurities.
- Both of the particle and thermal transport is improved in the high-density pellet shots after the RTC.

[Neon gas puff]

- Reduced ion number density together with the increased absorption power at low density range resulted in the higher ion temperature of over 4 keV than that obtained in hydrogen plasmas of ~ 2 keV.
- The global electron energy confinement is not depending on the ion species but on the electron gyro-radius.

- A new scaling law that can be applied to both of the hydrogen and neon plasmas has been derived.

These results directly indicate the importance of gas puffing in the plasma experiments. In addition to the easy and precise density control, flexibility in the working gas selection enables the experiments needed to understand the plasma physics, such as the recycling and the confinement property.

To realize the direct fueling into the plasma core, which cannot be attained by gas puffing, possibility of CT injection has been investigated. At first, CT orbit in the helical magnetic field was calculated and the central fueling was confirmed to be possible by the CT injection with realistic CT parameters, such as 0.2 m diameter, 10^{22} m^{-3} electron density, and 300 km/s initial velocity in the case of LHD magnetic field strength of 1.5 T. The CT injector named SPICA has been designed and developed based on the results of point model simulation. It was revealed that the acceleration efficiency is determined by the ratio of electrode inductance to the external inductance. The CT formation and acceleration experiments have been successfully carried out on SPICA. It was shown that CT generated in SPICA has spheromak-type internal magnetic field profile. After the elongation of acceleration electrode, CT performance has been improved as expected from the results of point model simulation. In the two-stage acceleration experiment, CT velocity of more than 200 km/s together with the CT density of order 10^{21} m^{-3} has been observed. The long distance transfer of CT has been examined in the large test chamber. It is demonstrated that the CT can be transferred more than 3.6 m after the acceleration. These results indicate that SPICA has enough performance for CT injection experiment on LHD. It should be also noted that SPICA is the largest CT injector in the world, at this moment, aiming at the fueling for the high-temperature plasmas.

This thesis has asserted that the gas puffing is still a powerful fueling method. As for the direct fueling to the plasma core, CT injection has been certified as the candidate. Although the knowledge obtained in this thesis is limited, it will be available for understanding the fueling physics. In the investigation of other fueling methods, such as the pellet injection, and the neutral beam injection, the information presented in this thesis will give the basis for comparison. Even for the complementary study of tokamak plasmas with helical plasmas, the results of this thesis can afford the basic database.

Appendix: Gyro-Bohm Scaling

The gyro-Bohm scaling is based on the drift-turbulence models [1 - 4], where the turbulence that drives the anomalous transport has a scale length of the order of the ion gyro radius with a decorrelation time of the ion diamagnetic drift time. These models can be characterized by an expression below;

$$\tau_E \Omega \propto (\rho^*)^{2\delta-3}, \tag{A.1}$$

where Ω is the ion gyro frequency and ρ^* is the ion gyro radius normalized by the plasma minor radius ($\rho^* = \rho_i/a$). Using this expression, $\delta = 0$ and $\delta = 0.5$ corresponds to the gyro-Bohm model and the Bohm model, respectively. The energy confinement time τ_E deduced from Eq. (A.1) is expressed as

$$\tau_E = C_0 a^{\alpha_a} R^{\alpha_R} B^{\alpha_B} P^{\alpha_P} \bar{n}_e^{\alpha_n} Z^{\alpha_{Z1}} \left(1+\frac{1}{Z}\right)^{\alpha_{Z2}} A^{\alpha_A}, \tag{A.2}$$

where C_0 is the fitting parameter, A and Z are the mass and the charge of the ion, respectively. Table A.1 is the list of the indices corresponding to $\delta = 0$ (gyro-Bohm), 0.25 (weak gyro-Bohm), and 0.5 (Bohm). These indices satisfy the collisional high beta constraint [5]. For example, the energy confinement time of the gyro-Bohm type, τ_E^{GB}, and the Bohm type, τ_E^{B}, are given as below;

$$\tau_E^{GB} = C_0\, a^{2.4} R^{0.6} B^{0.8} P^{-0.6} \bar{n}_e^{0.6} Z^{0.8} (1+1/Z)^{0.6} A^{-0.2}, \tag{A.3}$$

$$\tau_E^{B} = C_0\, a^{2} R^{0.5} B^{0.5} P^{-0.5} \bar{n}_e^{0.5} (1+Z)^{0.5}. \tag{A.4}$$

The Z dependence appears in both of the models, while the mass dependence does not appears in τ_E^{B}. Inverse mass dependence of $\tau_E^{GB} \propto A^{-0.2}$ included in the gyro-Bohm model has been observed in JET H-mode experiments [6].

Note that Eqs. (A.2) - (A.4) are expressed for two-components plasmas, which contain electrons and a single kind of ions. As for the general plasmas, where two or more ion species are included, it is not obvious what kind of parameters are to be used instead of Z and A. One of the possible assumptions is to substitute Z_{eff} and A_{eff} for Z and A in these equations, respectively. Here, A_{eff} is the effective ion mass, which is defined as the total ion mass density divided by the total ion number density, and is uniquely determined from Z_{eff} according to the

definition below;

$$A_{\text{eff}} = \frac{A_{\text{M}} n_{\text{M}} + A_{\text{I}} n_{\text{I}}}{n_{\text{M}} + n_{\text{I}}} = \frac{A_{\text{M}} + A_{\text{I}} \gamma}{1 + \gamma},$$

where subscript M (I) denotes the majority (impurity) ion and $\gamma = n_{\text{I}}/n_{\text{M}}$ is the ratio of impurity ion density to majority ion density, which can be directly derived from the definition of Z_{eff} as;

$$\gamma = \frac{Z_M{}^2 - Z_M Z_{\text{eff}}}{Z_{\text{I}} Z_{\text{eff}} - Z_{\text{I}}{}^2},$$

It is possible to classify a database by investigating the sensitivity of the fitting error with respect to the parameter δ. For instance, if the minimum of the fitting error is obtained at $\delta = 0$, the gyro-Bohm model is better than the Bohm model to explain the parameter dependence of the dataset on the ion gyro-radius.

References

[1] F. W. Perkins, in *Heating in Toroidal Plasmas*, Rome, 1984 (International School of Plasma Physics, Varenna, 1984), Vol. 2, p. 977.

[2] R. J. Goldston, et al., Bull. Am. Phys. Soc. **34**, 1964 (1989).

[3] M. Murakami, et al., Phys. Fluids B **3**, 2261 (1991).

[4] J. G. Cordey et al., Nucl. Fusion **39**, 301 (1999).

[5] U. Stroth et al., Nucl. Fusion **36**, 1063 (1996).

[6] J. G. Cordey et al., Nucl. Fusion **39**, 301 (1999).

Table A.1. Summary of the indices in three typical confinement models.

Name	expression	Index number		
		gyro-Bohm	weak gyro-Bohm	Bohm
		$\delta = 0$	$\delta = 0.25$	$\delta = 0.5$
α_P	$\frac{-1.5+\delta}{2.5-\delta}$	-0.6	-0.556	-0.5
α_n	$\frac{1.5-\delta}{2.5-\delta}$	0.6	0.556	0.5
α_B	$\frac{2-2\delta}{2.5-\delta}$	0.8	0.667	0.5
α_a	$\frac{6-4\delta}{2.5-\delta}$	2.4	2.222	2
α_R	$\frac{1.5-\delta}{2.5-\delta}$	0.6	0.556	0.5
α_{Z1}	$\frac{2-2\delta}{2.5-\delta}$	0.8	0.667	0.5
α_{Z2}	$\frac{1.5-\delta}{2.5-\delta}$	0.6	0.556	0.5
α_A	$\frac{-0.5+\delta}{2.5-\delta}$	-0.2	-0.111	0

List of Papers and Presentations

[Papers]

(1) J. Miyazawa, S. Masuzaki, H. Yamada, H. Suzuki, M. Goto, S. Morita, S. Murakami, K. Narihara, M. Osakabe, B.J. Peterson, S. Sakakibara, K. Tanaka, O. Kaneko, A. Komori, K. Matsuoka, O. Motojima and LHD experimental Group, "Fueling efficiency of gas puffing on large helical device", Journal of Nuclear Material **313-316** (2003) 534-538.

(2) J. Miyazawa, H. Yamada, R. Sakamoto, K. Tanaka, S. Morita, S. Sakakibara, M. Osakabe, M. Goto, O. Kaneko, K. Kawahata, A. Komori, S. Murakami, S. Muto, K. Narihara, N. Ohyabu, B.J. Peterson, A. Sagara, T. Tokuzawa, K.Y. Watanabe, Yuhong Xu, K. Yamazaki, and LHD experimental Group, "Favorable effect of methane discharges observed in LHD pellet shots", Plasma Physics and Controlled Fusion **44** (2002) A203-A209.

(3) J. Miyazawa, H. Yamada, K. Yasui, S. Kato, N. Fukumoto, M. Nagata, T. Uyama, "Design of spheromak injector using conical accelerator for Large Helical Device", Fusion Engineering and Design **54** (2001) 1-12.

(4) J. Miyazawa, H. Yamada, K. Yasui, S. Kato, N. Fukumoto, M. Nagata, T. Uyama, "Development of Compact Toroid Injector for Large Helical Device and New Concept of Burning Compact Toroid", Journal of Plasma Fusion Research SERIES, Vol. 3 (2000) 481-484.

(5) J. Miyazawa, H. Yamada, and O. Motojima, "Possibility of Profile Control using Compact Toroid Injection on Large Helical Device", Japanese Journal of Applied Physics **37** (1998) 6620-6627.

(6) J. Miyazawa, S. Kido, K. Sasaki, T. Suzuki, S. Kondou, J. Morikawa, H. Nihei, Z. Yoshida, Y. Ogawa, N. Inoue, "Vacuum UV Spectroscopy at REPUTE-1", Fusion Engineering and Design **34-35** (1997) 235-239.

[Presentations]

(International Conference)

(1) J. Miyazawa, H. Yamada, K. Yasui, S. Kato, N. Fukumoto, M. Nagata, and T. Uyama., "Development of a Compact Toroid Injector for Large Helical Device and a New Concept of Burning Compact Toroid", 10th International Toki Conference on Plasma Physics and Controlled Nuclear Fusion (Jan. 18 - 21, 2000, Toki, Japan).

(2) J. Miyazawa, N. Fukumoto, H. Yamada, M. Nagata, and T. Uyama, "Two-Stage Acceleration Experiment on a Compact Toroid Injector for the Large Helical Device", Joint Conference of The12th International Toki Conference on Plasma Physics and Controlled Nuclear Fusion and The 3rd General Scientific Assembly of Asia Plasma Fusion Association (December 12, 2001, Toki, Gifu, Japan).

(3) J. Miyazawa, H. Yamada, K. Tanaka, S. Morita, S. Sakakibara, M. Osakabe, R. Sakamoto, S. Muto, Yuhong Xu, B.J. Peterson, S. Murakami, S. Masuzaki, K. Narihara, A. Sagara, S. Ohdachi, H. Suzuki, H. Funaba, M. Goto, O. Kaneko, K. Kawahata, A. Komori, N. Ohyabu, and LHD experimental Group, "Effective Charge Dependence of Confinement Improvement Factor in LHD", P4.043, 28th EPS Conference on Controlled Fusion and Plasma Physics (June 18 – 22, 2001, Madeira, Portugal).

(4) J. Miyazawa, S. Masuzaki, H. Yamada, M. Goto, S. Morita, S. Murakami, K. Narihara, M. Osakabe, B.J. Peterson, S. Sakakibara, K. Tanaka, O. Kaneko, A. Komori, K. Matsuoka, O. Motojima and LHD experimental Group, "Fueling Efficiency of Gas Puffing on Large Helical Device", P3-48, 15th International Conference on Plasma Surface Interactions in Controlled Fusion Devices, (May 27 - 31, 2002, Gifu, Japan).

(5) J. Miyazawa, H. Yamada, S. Morita, Y. Takeiri, M. Osakabe, K. Narihara, K. Tanaka, S. Sakakibara, M. Goto, S. Murakami, R. Sakamoto, B.J. Peterson, K. Ida, O. Kaneko, K. Kawahata, A. Komori, Y. Nakamura, N. Ohyabu, and LHD experimental Group, "Global Electron Energy Confinement of Neon Plasmas in LHD", P-1.073, 29th EPS Conference on Plasma Physics and Controlled Fusion (June 17 – 21, 2002, Montreux, Switzerland).

(Domestic Conference)

(1) プラズマ核融合学会第14回年会(1997/11/25-28、大阪大学)

14AMPD-1「LHDにおける磁化プラズモイド入射軌道の計算」

宮沢順一、山田弘司、本島修

(2) 第2回核融合エネルギー連合講演会(1998/6/1-2、科学技術館サイエンスホール(東京都千代田区))

A66「磁化プラズモイド入射による分布制御の可能性」

宮沢順一、山田弘司、本島修

(3)プラズマ核融合学会第15回年会(1998/12/1-4、筑波大学)

4pB15「LHD用CT入射装置の設計」

宮沢順一、山田弘司、本島修

(4) 第3回核融合エネルギー連合講演会(2000/6/12-13、中部大学(春日井))

E29「大型ヘリカル装置における先進燃料供給実験計画とその現状」

宮沢順一、山田弘司、安井孝治、加藤眞治、福本直之、永田正義、宇山忠男

(5) 日本物理学会第55回年次大会(2000/9/22-25、新潟大学(新潟))

23aXG-5「大型ヘリカル装置用磁化プラズモイド入射装置SPICAの初期実験結果」

宮沢順一、山田弘司、福本直之、永田正義、宇山忠男

(6) プラズマ核融合学会第17回年会(2000/11/27-30、北海道大学(札幌))

30aB-01「LHD用CT入射装置SPICAにおけるCTの長距離飛行実験」

宮沢順一、山田弘司、福本直之、永田正義、宇山忠男

(7) プラズマ核融合学会第18回年会(2001/11/27-30、クローバープラザ(福岡県春日市))

30pB35P「LHD用CT入射装置SPICAにおける二段加速実験」

宮沢順一、山田弘司、福本直之、永田正義、宇山忠男

(8) プラズマ核融合学会第19回年会(202/11/26-29、犬山国際観光センター「フロイデ」(愛知県犬山市))

29pB22P「Recent Results of SPICA as the CT injector for LHD」

宮沢順一、山田弘司、福本直之、永田正義、宇山忠男